HERALDED SINGLE PHOTONS FOR EFFICIENT INTERACTION WITH SINGLE ATOMS

BHARATH SRIVATHSAN

B.E. (hons) Electrical and Electronics, BITS-Pilani

M.Sc. (hons) Physics, BITS-Pilani

A THESIS SUBMITTED FOR THE DEGREE OF DOCTOR OF PHILOSOPHY

CENTRE FOR QUANTUM TECHNOLOGIES

NATIONAL UNIVERSITY OF SINGAPORE

2015

Declaration

I hereby declare that the thesis is my original work and it has been written by me in its entirety. I have duly acknowledged all the sources of information which have been used in the thesis.

The thesis has also not been submitted for any degree in any university previously.

Bharath Srivathsan

December 11, 2014

Acknowledgements

First and foremost, I would like to thank my lab partner, Gurpreet Kaur Gulati for working on the project with me since its inception. She has been a wonderful person to work with, and has become a great friend. All the brainstorming sessions with her on various physics and technical problems made my PhD years truly fun and worthwhile.

Next I would like to thank my supervisor, Prof. Christian Kurtsiefer for teaching me not just atomic physics and quantum optics, but also proper ways to write papers and present talks. He has always encouraged me and supported my ideas for the project, for which I am eternally grateful.

Special thanks to Brenda Chng for her help in setting up the experiment, teaching me to use the machines in our workshop, and proof reading all our papers and this thesis. I would also like to thank Prof. Dzmitry Matsukevich for helping us whenever we got stuck during the initial stages of the project. Thanks to Gleb Maslennikov and Syed Abdullah Aljunid for teaching me the ways of the lab and basic experimental skills. Alessandro Cerè has been of great help during the final two years of the project for which I am very grateful.

I would like to express my gratitude to Victor Leong and Sandoko Kosen, students from the single atom project for making it possible to connect our two experiments. Special thanks to Victor for proof reading this thesis. I would also like to thank the other students who worked on the project with me: Chin Chii Tarng, Kathrin Luksch, Mathias Seidler, and Victor Huarcaya Azanon. Thanks also to my office mate and a friend Siddarth

Joshi, and all the current and past members of the quantum optics group.

Last but not least, I would like to thank my parents for always being supportive of me, and showing interest in my experiments.

Contents

Summary

In this work we present a source of single photons for efficient interaction with a single atom. We start by generating narrowband time-correlated photon pairs of wavelengths 762 nm and 795 nm (or 776 nm and 780 nm) from non-degenerate four-wave mixing in a laser-cooled atomic ensemble of ^{87}Rb using a cascade decay scheme. Coupling the photon pairs into single mode fibers, we observe an instantaneous photon pair rate of up to 18000 pairs per second with silicon avalanche photodetectors. Detection events exhibit a strong correlation in time with a peak value of the cross-correlation function $g_{si}^{(2)}(t) = 5800$, and a high fiber coupling indicated by heralding efficiencies of 23% and 19% for signal and idler modes respectively.

Single photons are prepared from the generated photon pairs by heralding on the detection of one of the photons using a single photon detector. The detection statistics measured by a Hanbury-Brown-Twiss experiment shows strong anti-bunching with auto-correlation $g^{(2)}(0) < 0.03$, indicating a near single photon character. The bandwidth of the heralded single photons is tunable between 10 MHz and 30 MHz, as measured by using a Fabry-Perot cavity. In an optical homodyne experiment, we directly measure the temporal envelope of these photons and find, depending on the choice of the heralding mode, an exponentially decaying or rising temporal profile.

We then study the interaction of single photons of different temporal shapes with a single mode of an asymmetric cavity. We find that coupling the first photon of the cascade decay to such a cavity, and using its detection as a herald reverses the temporal shape of its twin photon from a decaying to a rising exponential envelope. The narrow bandwidth and high brightness of our source makes it well suited for interacting with atomic systems for quantum information applications. Moreover, the rising exponential temporal shape of the photons will be useful for efficient absorption by a single atom.

List of Publications

The main results of this thesis have been reported in the following articles

1. **Bharath Srivathsan**, Gurpreet Kaur Gulati, Brenda Chng, Gleb Maslennikov, Dzmitry Matsukevich, and Christian Kurtsiefer. **Narrow Band Source of Transform-Limited Photon Pairs via Four-Wave Mixing in a Cold Atomic Ensemble**. *Phys. Rev. Lett.* **111**, 123602, September 2013.

2. Gurpreet Kaur Gulati, **Bharath Srivathsan**, Brenda Chng, Alessandro Ceré, Dzmitry Matsukevich, and Christian Kurtsiefer. **Generation of an exponentially rising single-photon field from parametric conversion in atoms**. *Phys. Rev. A*, **90**, 033819, September 2014.

3. **Bharath Srivathsan**, Gurpreet Kaur Gulati, Brenda Chng, Alessandro Ceré, and Christian Kurtsiefer. **Reversing the Temporal Envelope of a Heralded Single Photon using a Cavity**. *Phys. Rev. Lett.*, **113**, 163601, October 2014.

List of Figures

LIST OF FIGURES

LIST OF FIGURES

Chapter 1

Introduction

Over the past two decades, there has been a tremendous growth in research on quantum information and computation. This growth stems from the promise of being able to perform some computational tasks much faster in a quantum computer than the classical counterparts [1, 2, 3], and potentially unbreakable crytographic protocols [4, 5]. In order to perform these tasks and protocols, we need the ability to initialize, manipulate, store and measure the quantum states of some quantum system for a physical implementation. In addition it is also essential to connect physical systems situated at different locations in order to build any viable large scale quantum networks [6, 7, 8, 9]. There are a variety of different physical implementations currently being researched such as photons [10], neutral atoms [11], ions [12], cavity QED [13], spins in NMR [14], superconducting circuits [15], quantum dots [16] etc. Each has its own advantages and disadvantages as discussed in [17]. It is widely agreed upon that the photons are ideal for transmitting quantum information over long distances as they interact weakly with the environment and therefore preserve coherent superposition states well. On the other hand atomic systems are well suited for manipulation and storage of the quantum states. An efficient transfer of information between the two systems requires strong interaction between photons and atoms.

Apart from the quantum information applications, a more fundamental interest in single atom - single photon interaction is to answer one of the elementary questions

in quantum optics: Whether it is possible to reverse the spontaneous emission from a single atom [18]. In other words, is it possible to excite an atom in its ground state to an excited state using a single photon Fock state? There has been some work on developing theoritical models to describe this process [19, 20], and proof of principle experiments [21, 22, 23, 24]. However, an experimental demonstration at a single quantum level still remains to be performed. With the recent advances in cavity QED [25], and free space trapping of single atoms with large spatial mode overlap [26], it may now be possible to perform experiments to verify this. According to the theoretical predictions, single photons required for such an experiment should have some very specific constraints on the spectral and temporal properties [19]. The bandwidth of the interacting photons has to match the linewidth of the atomic transition, and the temporal envelope of the photons should be the time reversal of a photon from the spontaneous emission.

In this thesis, we present a source of single photons that is suitable for interaction with atomic systems for quantum information applications, and to test the reversibility of the spontaneous emission process. We use a photon pair source based on fourwave mixing in an atomic ensemble as a starting point. The detection of one photon of the pair is then used as a herald for the preparation of a single photon. We present various experiments to quantitatively characterize the generated single photons, and ways to manipulate them for efficient interaction with atoms.

1.1 Thesis Outline

Chapter 2 : We start by describing the basic equipment and experimental techniques for cooling and trapping an ensemble of atoms. This is followed by a description of the experimental setup, source alignment procedures, and generation and detection of entangled photon pairs by fourwave mixing via cascade decay level scheme.

Chapter 3 : Here we describe how single photons are obtained from the generated

photon pairs by heralding, and measurements of some characteristic qualities the single photons including a temporal auto-correlation function, bandwidth, and temporal field envelope.

Chapter 4 : In this chapter we discuss the interaction of heralded single photons with an asymmetric cavity as a method to shape the temporal envelope of the single photons in order to make them suitable for absorption by a single atom. By using a different interpretation of the same experiment, we investigate how single photons with different temporal shapes affect the population of the cavity.

Chapter 5 : In the final chapter we present the conclusion of the thesis, some of the ongoing work and future experiments that can possibly be performed.

The results presented in Chapter 2 of this thesis is a joint work with Ms. Gurpreet Kaur Gulati and therefore also appears in a her PhD thesis [76]. While the rest of my work focuses on the characterizing and engineering the spectral and temporal properties of the heralded single photons for absorption by a single atom, her work aims to characterize the entanglement between the photons of the pair in different degrees of freedom and interfacing with a single atom via quantum interference rather than direct absorption.

The results on generation of photon pairs and the bandwidth measurements are published in [27], the proof of single photon nature and the field measurements in [28], and the interaction of the photons with an asymmetric cavity in [29].

Chapter 2

Generation of photon pairs

Time-correlated and entangled photon pairs have been an important resource for a wide range of quantum optics experiments, ranging from fundamental tests [30, 31, 32, 33] to applications in quantum information [4, 10, 34, 35, 36]. Many initial experiments used a cascade decay in atomic beam to generate photon pairs [32, 37]. These photons showed strong non-classical correlation in time and polarization, but large numerical aperture lenses close to the atoms were needed to collect sufficient photons to perform the experiments. Another way to generate photon pairs uses parametric frequency conversion process in non-linear optical crystalline materials. This was first observed in [38] and is in fact the most widely used technique today for generating correlated photon pairs. The key advantage of this method is that the photon pairs can be generated in well defined spatial modes (see Section 2.1.1)

Spontaneous Parametric Down Conversion (SPDC) in $\chi^{(2)}$ nonlinear optical crystals has been the workhorse for generating photon pairs for the past three decades. Although extremely robust, the photons from SPDC have very broad bandwidths ranging from 0.1 to 2 THz [39, 40, 41]. This makes it difficult to interact with atom like physical systems, since their optical transitions usually have a lifetime-limited bandwidth on the order of several MHz. Various filtering techniques have been employed to reduce the bandwidth of SPDC photons. In addition, the parametric conversion bandwidth may be redistributed within the resonance comb of an optical cavity [42, 43, 44, 45].

Another parametric process Four-Wave Mixing (FWM), exploits the third order susceptibility ($\chi^{(3)}$) and has been used to generate photon pairs from nonlinear fibers [46, 47], hot vapor cells [48, 49], and cold atomic ensembles [50, 51, 52]. FWM in atomic ensembles rely on large nonlinear optical coefficient $\chi^{(3)}$ near the atomic resonances. We generate photon pairs by FWM in a cold cloud of atoms using a cascade level scheme similar to previous work by Chanelière et al. [53].

In this chapter, the theory of photon pair generation by FWM is briefly introduced in Section 2.1. This is followed by some technical details of the equipment in Section 2.2. Section 2.3 describes the experimental setup and the source alignment procedure. Finally, the results of the correlation measurements that demonstrates the generation of the pairs are presented in Section 2.4.

2.1 Theory

In non-linear optics the response of a dielectric material to applied optical fields can be written as a series expansion [54]

$$P = \epsilon_0(\chi^{(1)}E + \chi^{(2)}E^2 + \chi^{(3)}E^3 + ...) \tag{2.1}$$

where E is the strengths of the applied optical field, P is the dipole moment per unit volume, also known as polarization of the material. The coefficient $\chi^{(1)}$ is the linear susceptibility and is related to the refractive index of the material, $n = \sqrt{\chi^{(1)} + 1}$. The second- and third- order non-linear susceptibilities $\chi^{(2)}, \chi^{(3)}$ of the optical media are negligibly small in many materials. However, the response of some materials due these terms becomes significant at high field strengths. The SPDC process in a typical nonlinear crystal is described by the $\chi^{(2)}$ term.

In the case of neutral atoms as a non-linear medium, the $\chi^{(2)}$ term vanishes due to the inversion symmetry of the atoms. This can also be seen from the angular momentum selection rules. In the electric dipole approximation, parametric coupling of three fields to an atom is disallowed due to angular momentum conservation [54]. Hence the lowest

order non-linear response of an atom comes from the $\chi^{(3)}$ term which is responsible for FWM processes.

We generate photon pairs via a non-degenerate spontaneous FWM process in the presence of two continuous wave (CW) pump beams. Photons from the pump lasers are probabilistically converted into pairs of photons in two optical modes called the signal and idler modes. A simplified level scheme for FWM in a cascade decay is shown in Figure 2.1 (Right). Assuming that the intensity of the pump laser is chosen such that the atomic population remains primarily in the ground level (a), the third-order nonlinear susceptibility for this scheme is given by [54]

$$\chi^{(3)}(\omega_i = \omega_1 + \omega_2 - \omega_s) = \frac{NL}{6\hbar^3} \frac{\mu_{ab}\,\mu_{bc}\,\mu_{cd}\,\mu_{da}}{[\omega_{ab} - i\Gamma_b - \omega_1]\,[(\omega_{ab} + \omega_{bc}) - i\Gamma_c - (\omega_1 + \omega_2)]\,[\omega_{ad} - i\Gamma_d - (\omega_1 + \omega_2 - \omega_s)]} \tag{2.2}$$

where N is the atom density, L is the length of the interaction region, $\mu_{ab,bc,cd,da}$ are electric dipole matrix elements, $\omega_{1,2,s,i}$ are the frequencies of the pumps, signal and idler field, $\omega_{ab,bc,cd,ad}$ are the atomic transition frequencies, and $\Gamma_{b,c,d}$ are the linewidths of the excited levels. The physical quantity measured in an experiment is the intensity of the signal and idler fields for a fixed intensity of the pump fields. This quantity can be considered as a measure of the strength of the FWM process and it is proportional to $|\chi^{(3)}|^2$. Therefore Eq. (2.2) indicates how the strength of the FWM process is related to the atom density and the detunings of the fields from the atomic resonances. Since FWM is a parametric process, the energy of the participating fields has to be conserved. This condition is also included in Eq. (2.2).

The output state of the light generated from a parametric process assuming single spatio-spectral modes for the signal and idler is given by [55]

$$|\psi(t)\rangle \;=\; \frac{1}{\cosh(\kappa t)} \sum_{n=0}^{\infty} \tanh(\kappa t)^n \,|n\rangle_s \otimes |n\rangle_i \,, \tag{2.3}$$

where κ is the effective interaction strength proportional to $\chi^{(3)}$ and the intensities of

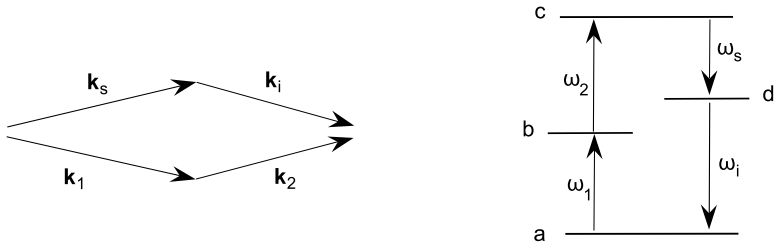

Figure 2.1: Conditions for FWM. (Left) Phase matching condition. (Right) Energy conservation with cascade level scheme

the pump fields, t is the interaction time, and $|n\rangle_s$ and $|n\rangle_i$ are the photon number states in the signal and idler modes. It can be seen that the photon number is strongly correlated between the signal and the idler modes. Since the interaction strength κ is usually small, multi-photon states corresponding to higher order terms with $n \geq 2$ have much smaller probability of occurrence compared to $n = 0$ or 1. Therefore the output state from such a system is a very good approximation of a two-photon pair state.

A complete theoretical description of the FWM process in atoms is outside the scope of this thesis. A detailed study of parametric frequency conversion with a four-level system in a cascade decay scheme can be found in [56].

2.1.1 Phase matching

The cascade decay in atoms can generate photon pairs even with a single atom interacting with the pump lasers. Since the spontaneous emission from a single atom is more or less isotropic [1], the emitted photons cannot be easily collected into single mode fibers. This was also the case in early experiments with atomic beams [37].

On the other hand, using a spatially extended ensemble of atoms as a non-linear medium provides translational symmetry and therefore leads to momentum conservation. The photons generated by FWM in an atomic ensemble satisfy the following criteria known as phase matching condition

$$\mathbf{k_1} + \mathbf{k_2} = \mathbf{k_s} + \mathbf{k_i}\,, \tag{2.4}$$

[1] The dipole transitions are not always isotropic [57]

where k_1, k_2, k_s and k_i are wave-vectors of the two pumps, signal and idler modes. This implies that for Gaussian mode pump beams, the photon pairs are generated in well defined spatial modes that satisfy Eq. (2.4). This in turn enables efficient collection of photons into single mode fibers without the need for high numerical aperture lenses close to the medium. In the experiment we use Gaussian beams with Rayleigh length much longer than the length of the atomic medium such that we have a nearly plane wavefront for all the four modes. The 1/e diameter for the beams were chosen to be approximately the same as the diameter of the atom cloud in the transverse direction so as to maximize the overlap with the cloud without compromising much on the pump intensity.

2.2 Prerequisites

The main prerequisites for a parametric process are coherent light sources and a non-linear medium. We use lasers as a source of coherent light and a cold ensemble of ^{87}Rb atoms as the non-linear medium. In this section we briefly discuss the laser systems, and cooling and trapping of the atoms.

2.2.1 Rubidium

We choose to work with ^{87}Rb atoms for compatibility with another experiment in our group with a single trapped atom [58, 59]. ^{87}Rb is a naturally occurring isotope of Rubidium with atomic number 37. It has a natural abundance of 28% and a mass of 86.9 amu and a nuclear spin of $I = 5/2$ [60]. The energy levels we are interested in this thesis are the ground level $5S_{1/2}$, the first excited levels $5P_{1/2}$ and $5P_{3/2}$, and the second excited level $5D_{3/2}$. The wavelengths of the transition between these levels are shown in Figure 2.2. For the full hyperfine manifold of these levels refer to appendix E
.

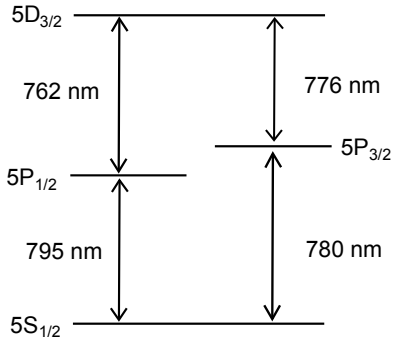

Figure 2.2: Energy levels of ^{87}Rb along with the transition wavelengths. Only the relevant levels used in the experiment are shown.

2.2.2 Lasers

The lasers are essential for cooling and trapping atoms, as pump and alignment beams and as frequency reference for generated photons. It is therefore useful to have them operating with narrow bandwidths compared atomic transition linewidths. All the lasers used in our experiment make use of temperature stabilized single-mode semiconductor laser diodes. For the lasers of wavelengths 780 nm and 795 nm, we use Sanyo diodes (DL7140-201SW) with a rated output power of 60 mW at a recommended forward current of 100 mA [61]. However, we operate the diodes at 70 mA with an output power of about 35 mW in order to extend their operating lifetime. The operating wavelength of these diodes is around 780 nm at room temperature ($\approx 20\,^{\circ}$C). To obtain a 795 nm laser beam, we heat these diodes up to 65 °C. We also require lasers of wavelengths 762 nm and 776 nm that corresponds to the frequency difference between the first and the second excited level of ^{87}Rb (see Figure 2.2). For these wavelengths, we use ridge waveguide diodes with a wide tuning range of 760 nm to 800 nm from Eagleyard (EYP-RWE-0780-02000-1300-SOT12-0000). We operate these diodes at a forward current of ≈ 100 mA with an output power of 65 mW. The temperature of the diodes is stabilized to an accuracy of 1 mK using a Peltier element, a thermistor, and a home built digital Proportional-Integral-Derivative (PID) controller.

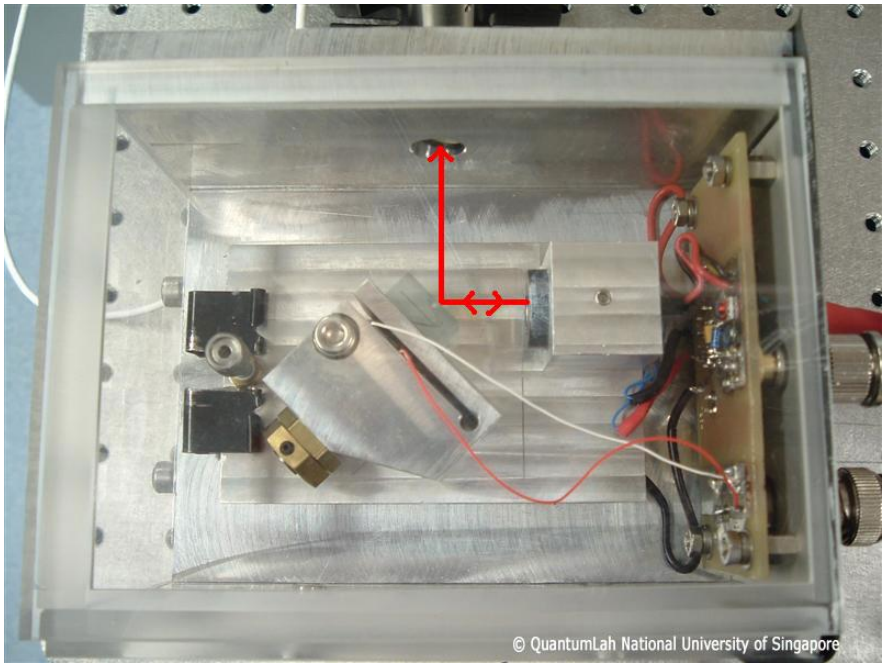

Figure 2.3: Photo of an External Cavity Diode Laser (ECDL). The grating is positioned in such a way that the first order diffraction of the incident light from the diode goes back into the diode thus forming the cavity.

External Cavity Diode Laser

The frequency bandwidth of the light from these diodes is a few orders of magnitude more than the atomic transition linewidths. We use an external cavity formed by a diffraction grating in the Littrow configuration as shown in Figure 2.3 to reduce the bandwidth. This design is commonly referred to as External Cavity Diode Laser (ECDL) [62]. The grating is aligned such that the first diffraction order of the light from the diode is reflected back into the diode to form the external optical cavity. The zero-order beam from the grating is used for the experiment. A piezo electric actuator is used to fine tune the the normal angle of the grating with respect to the incident light. This provides the means to adjust the frequency of the laser.

The linewidths of the Sanyo lasers in this configuration were measured by mutual beat measurements [63] to be between 1 MHz and 2 MHz. We note that the linewidth of the lasers is wider than the linewidth of the $5D_{3/2}$ level of ≈ 700 KHz (Figure 2.2). In

order to see how this affects our experiment, consider two photon scattering of the pump beams (780 nm and 776 nm) by a cold cloud of ^{87}Rb atoms. The fraction of the scattered light from the pump beams that remain coherent with the pump beams depend on the linewidth of the lasers. A detailed discussion of coherence in the scattering process can be found in [75]. If the linewidth of the lasers is much smaller than the atomic transition linewidth, the scattered light remains mostly coherent. However in our case, since the laser linewidth is wider than the linewidth of the transition a fraction of the scattered light becomes incoherent with the pump beams. Since FWM is a result of coherent scattering of the pump beams into signal and idler photon pairs, the laser linewidth also affects the FWM process efficiency. Therefore, minimizing the laser linewidth or phase locking of the two pump lasers can improve the rate and efficiency of the photon pairs obtained in this work (see Section 2.4).

The spatial mode of these laser beams exhibit a 2:1 ellipticity due to the difference in divergence along the two transverse axes [61]. This is corrected by using a pair of anamorphic prisms. An optical isolator with 30 dB isolation is used to prevent back reflection from any optical surfaces reaching the diode and disturbing its oscillation at a particular frequency.

Frequency modulation spectroscopy

In addition to obtaining a narrow bandwidth, it is also necessary to stabilize the frequency of these lasers. We use Doppler-free frequency modulation (FM) spectroscopy to atomic transition lines. A strong pump beam and a relatively weak probe beam is aligned in a counter-propagating geometry through a rubidium reference cell (Thorlabs. GC19075-RB). The pump beam is used to saturate the atomic transition, while the probe beam is used to measure the change in absorption and phase shift acquired across the saturated atomic resonance. Frequency modulation of the beams is performed by an Electro-Optic Modulator (EOM) driven by a tank circuit with a 20 MHz resonance frequency. The frequency modulation of the probe beam is converted into amplitude modulation at 20 MHz using a photodiode. The dispersion of the probe

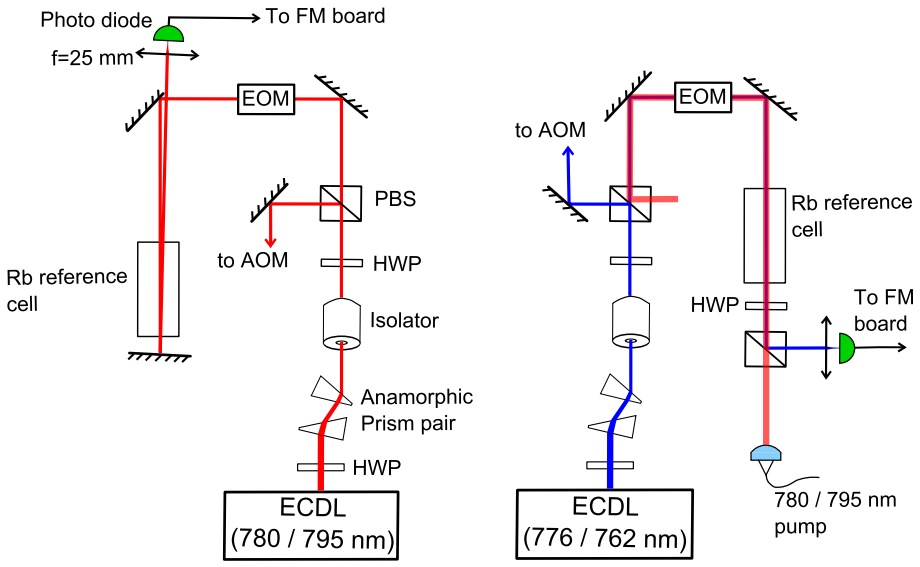

Figure 2.4: **(Left)**The optical setup of FM spectroscopy used for the 780 nm and 795 nm lasers. **(Right)**The optical setup of FM spectroscopy used for the 776 nm and 762 nm lasers.

beam across the atomic resonance appears as a phase shift in the photodiode signal. This phase shift is converted into a DC error signal by frequency demodulation. An analog PID controller uses the error signal to provide feedback to the grating PZT and hence lock the frequency of the laser. The demodulation and PID lock is performed using a home built FM circuit board.

The optical setup for FM spectroscopy is shown in Figure 2.4. For the 780 nm and 795 nm lasers both the pump and the probe beams are of same wavelength and are derived from the same laser. However for the 762 nm and 776 nm lasers, we first need to saturate the ground state resonant transition at 795 nm and 780 nm respectively. Therefore the pump beams are derived from a different ECDL. In this case the Rb reference cell is warmed up to a temperature of 70 °C in order to increase effective atom density. This is required because the transition between the first and second excited levels of ^{87}Rb is much weaker than the ground state resonant transitions [64]. The error signals that we observe in our experiment with these lasers are shown in

appendix E

FM spectroscopy is a very well established technique to perform frequency locks. A comprehensive description of the technique can be found in [65].

The AOM

The frequency of each laser is shifted by using either a 80 MHz or a 200 MHz Acousto-Optic Modulator(AOM) (Crystal technology, 3080-122 or 3200-124). A Radio-Frequency (RF) signal of an appropriate frequency generated by a Direct Digital Synthesizer (DDS) and amplified by a Mini circuits power amplifier is used to drive the AOMs. The AOM works based on the acousto-optic effect to diffract and shift the frequency of the laser with acoustic waves formed by the applied RF field [54]. We use the first order diffraction that shifts the light frequency by the RF frequency and also deflects the beam from its original path. The diffracted beam is then coupled using an aspheric lens into a single-mode optical fiber to guide them to the main experiment. Apart from shifting of the laser frequency, the AOM also acts as an optical switch. This is done by switching the RF signal supplied to the AOM using a Mini circuits switch (ZYSWA-2-50DR), thereby switching on/off the first diffraction order.

Tapered Amplifier

To obtain a sufficiently dense cloud of atoms (see Section 2.2.3), we require cooling lasers with an optical power of about 300 mW. We use a Tapered Amplifier (TA) with a maximum output power of 1 W (Eagleyard EYP-TPA-0780-01000-3006-CMT03-0000) to obtain our cooling lasers [1]. The TA is mounted on a copper block which is temperature stabilized in the same way as the ECDLs. We use a commercial Thorlabs current controller unit (LDC240C) to supply a constant current to the TA. The seed beam is derived from a frequency stabilized 780 nm ECDL 55 MHz blue detuned from the $5S_{1/2}, F = 2 \rightarrow 5P_{3/2}, F = 3$ atomic transition. The seed is mode matched to the

[1] This TA failed after 2 years of operation and was replaced with a 2 W version (EYP-TPA-0780-02000-3006-CMT03-0000).

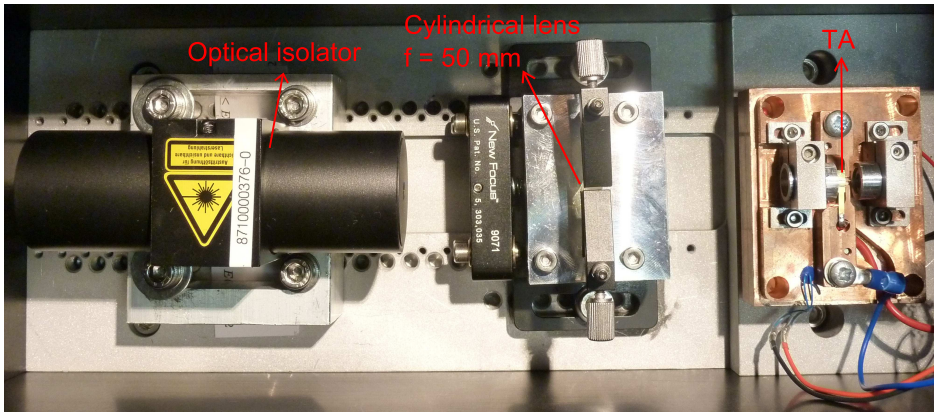

Figure 2.5: Photo of the Tapered Amplifier (TA) kit. The TA chip is mounted on a copper heat sink and temperature stabilized using a peltier element. The aspheric lenses used for mode matching the seed beam and collimating the output can be seen around the TA chip. The cylindrical lens and the optical isolator are also enclosed in the kit.

input of the TA using an aspheric lens of focal length 6.16 mm (Thorlabs C170-TME-B). The output beam of the TA is collimated using an aspheric lens of focal length 2.75 mm (Thorlabs C390-TME-B) and a cylindrical lens of focal length 50 mm (Thorlabs LJ1821L1-B) is used to correct the astigmatism. A 60 dB Linos optical isolator is used to prevent any back reflection to the TA. An 80 MHz AOM shifts the frequency of the amplified light from the TA 24 MHz to the red of the above mentioned transition. This AOM acts as an optical switch for the cooling laser.

A measurement of the output optical power from the TA for different forward operating currents and seed beam powers is shown in Figure 2.6. We operate the TA with a seed beam power of ≈ 20 mW and forward current of ≈ 2 A [1].

2.2.3 Cooling and trapping the atoms

We use a cold cloud of ^{87}Rb atoms trapped by a Magneto-Optical Trap (MOT) to perform the FWM experiment. The advantage of using a cold ensemble as opposed to

[1] The operating current was gradually increased over the lifetime of the TA from 2 A to 2.5 A to maintain the optical power output

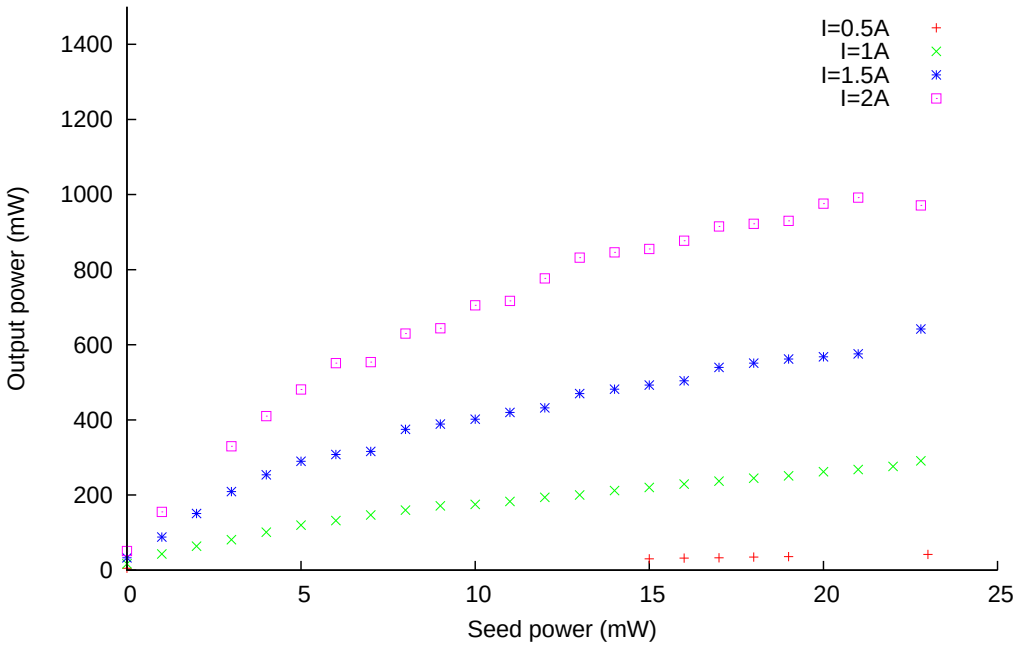

Figure 2.6: Output power of the TA for different operating currents and seed beam powers.

a hot vapor cell is that the Doppler broadening of the atomic transition line becomes negligible. This in turn reduces the bandwidth of the generated photons by an order of magnitude compared to the hot vapor.

The MOT

A Magneto-Optical Trap is a widely used method for cooling and trapping the neutral atoms. The working principle of the MOT is illustrated in Figure 2.7. When an atom absorb a photon from a laser, it gains momentum along the **k**-vector of the laser. When the laser is slightly red detuned from the atomic resonance, only the atoms moving towards the laser source with a certain velocity corresponding to the detuning absorbs the light due to the Doppler effect. For cooling to happen the atom has to be illuminated by counter-propagating lasers along all three directions. The trapping in a MOT is performed by a quadrupole magnetic field with a nearly linear field gradient at the origin. This results in a spatially dependent Zeeman shift of the atom's m_f sub-

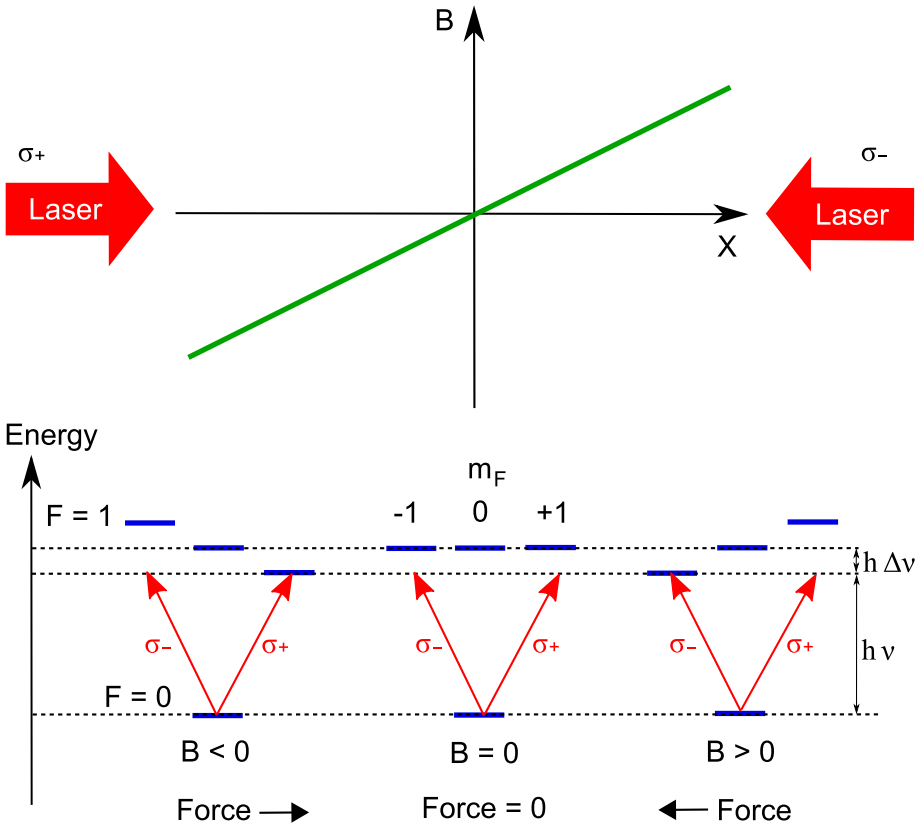

Figure 2.7: The working principle of the MOT illustrated using a simplified hypothetical atom with $F = 0 \rightarrow F = 1$ cooling transition. The magnetic field gradient creates a position dependent shift of the Zeeman sub-levels. The polarization of the cooling light is chosen such that the net force on the atoms due to absorption and reemission of the cooling light is directed towards the center of the MOT.

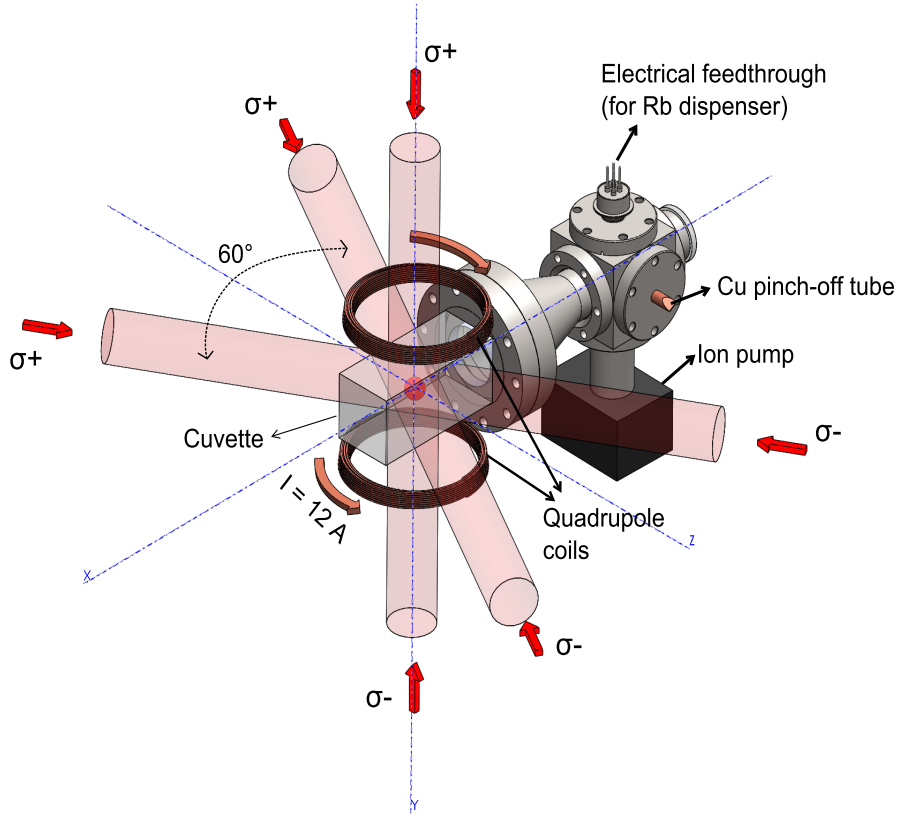

Figure 2.8: Magneto-Optical Trap (MOT). The figure shows the vacuum chamber, cooling beams and quadrupole coils used to make the MOT.

levels, which increase with the radial distance from the field zero point. Because of this, an atom moving away from the center sees the red detuned cooling laser propagating in the opposite direction with the appropriate polarization to be on resonance, and gets a momentum kick towards the center of the trap by absorbing a photon. There is plenty of literature on the working principles of the MOT [66, 67, 68] and is therefore not discussed in more detail in this thesis.

Here we give a brief description with the technical details of the MOT used in our experiment.

- **Vacuum chamber -** The first step in making a cold atomic ensemble is a good vacuum. Our vacuum chamber consists of a central cube of edge length $1\frac{1}{3}$". Each

side of the cube is connected to a vacuum component by a CF connection. We use a turbo molecular pump connected to the chamber via a copper pinch-off tube for initial evacuation to a pressure of about 10^{-6} mbar. A ion getter pump from Varian with pumping speed of 2 l/s is used to bring the chamber pressure further down. The pressure in our chamber is inferred from the ion pump current controller (Varian Microvac 929-0200) to be about 2×10^{-9} mbar [69]. One port of the cube is attached to an electrical feed-through with a Alvasource Rb dispenser from Alvatec. A glass cuvette of outer dimensions 70 mm × 30 mm × 30 mm which is anti-reflection (AR) coated on the outside for 780 nm wavelength is attached to another port of the cube. The MOT is formed within the cuvette which provides good optical access to the atom cloud. The design of the vacuum chamber along with the components is shown in Figure 2.8.

- **Quadrupole magnetic field -** The next step is to get a linearly varying magnetic field (B-field) gradient with a central zero point. A pair of circular current carrying coils connected in an anti-Helmholtz configuration produces a quadrupole B-field with this kind of field gradient near the center. Each coil is made of 40 turns of enamal coated copper wires with a 3 mm × 3 mm square cross-section carrying a current of 12 A. The estimated B-field gradient with this configuration is 24.8 G/cm in the radial direction and 49.6 G/cm in the axial direction.

- **Cooling and repump beams -** The final ingredients for a MOT are the cooling beams. Counter-propagating, circularly polarised cooling laser beams along three axes as shown in Figure 2.8 are aligned to intersect within the glass cuvette at the position of the zero B-field. The cooling beams are obtained from the TA and their frequencies are tuned using an AOM to be 24 MHz red detuned from the cycling transition in ^{87}Rb, $5S_{1/2}, F = 2 \rightarrow 5P_{3/2}, F = 3$. Each beam has diameter of about 15 mm with an optical power of 45 mW, which corresponds to a peak intensity $>$ 15 times the saturation intensity (I_{sat}). Even though the cycling

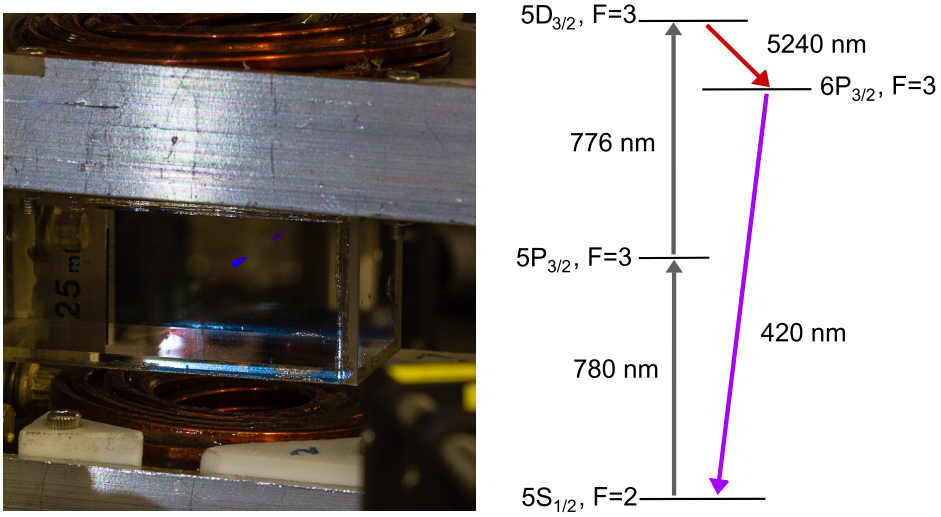

Figure 2.9: (Left) Blue fluorescence from the atom cloud in the presence of the 780 nm and 776 nm pump lasers. **(Right)** The relevant levels of ^{87}Rb that results in emission of the blue fluorescence.

transition forbids the population of $5S_{1/2}, F = 1$ level, there is a small probability of scattering via the $5P_{3/2}, F = 2$ level to $5S_{1/2}, F = 1$ level. Population of this level stops the cooling process. Therefore, we use an additional repump laser of power 9 mW and tuned to the transition $5S_{1/2}, F = 1 \rightarrow 5P_{3/2}, F = 2$ to deplete the population in this level.

A picture of the fluorescence from atoms trapped by the MOT in the presence of the 780 nm and 776 nm pump lasers is shown in Figure 2.9. We see blue (420 nm) fluorescence from one of the possible decay paths from the $5D_{3/2}$ level via $6P_{3/2}$ level to the ground state.

Measuring the optical density of the cloud

For many measurements shown in this thesis, the number of atoms interacting with the optical fields is an important quantity. We use the optical density (OD) of the cloud on resonance to the cooling transition as a measure of the number of atoms [57].

$$OD = \frac{d^2\nu}{2c\hbar\epsilon_0 A\gamma} N\,, \tag{2.5}$$

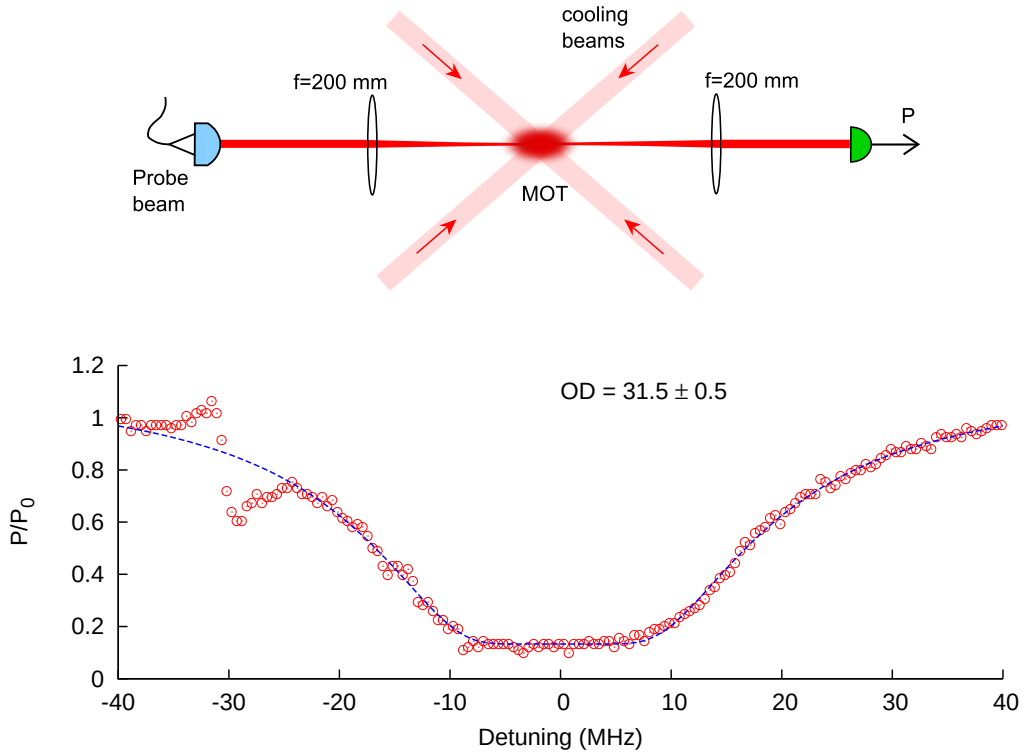

Figure 2.10: (Top) Setup to measure the optical density of the cloud. A probe laser is focused on to the center of the cloud and the transmitted power P is measured using a photodiode. The cooling lasers are on during the measurement of OD. **(Bottom)** Transmission as a function of probe detuning from the resonance. The dashed line is from a fit of the points between -10 MHz and 40 MHz detuning to Eq. 2.6. The deviation from the expected shape on the red detuned side is due to EIT.

where N is the number of atoms, A is the area of cross-section of the beam, ν is the transition frequency, d is the transition dipole moment, and γ is the line width of the transition. The first term on the right side of Eq. (2.5) is a constant. Therefore, OD is directly proportional to N. We get the OD of the cloud by measuring the transmission of a weak probe beam focused onto a 100 μm spot approximately at the center of the cloud. The frequency of the probe beam is scanned across the resonance, and the transmitted power P is measured using the a PIN photodiode. The transmission as a

function of detuning from the atomic resonance Δ can be described by

$$P(\Delta) = bg + P_0\, e^{-\frac{od\,\gamma^2}{4\Delta^2+\gamma^2}}, \tag{2.6}$$

where P_0 is the incident power of the probe beam, bg is the background signal in the absence of the probe beam. The measured transmission as a function of the detuning is shown in Figure 2.10. We see a sharp feature in the transmission spectrum that deviates from the expected behavior on the red detuned side. This is because the measurement was carried out with the MOT cooling lasers "on" while probing the atoms. The presence of the strong cooling beams changes the transmission of the weak probe beam creating a transparency window centered at the detuning of the cooling beams. This phenomenon is called Electromagnetically Induced Transparency (EIT) [70]. We fit the measured experimental points to Eq. 2.6 to obtain the OD of the cloud. In our experiment, we observe a maximum OD of ≈ 33. The measurement of the number of atoms in the cloud determined absorption imaging is described in appendix A.

2.3 Experimental setup

2.3.1 Optical setup and level scheme

The optical setup for generating the photon pairs in a non-collinear geometry is shown in Figure 2.11. The pump beams of wavelengths 780 nm and 776 nm from single mode fibers (SMF) are collimated using aspheric lenses of focal length 4.51 mm (Thorlabs C230-TMB) resulting in a beam waist of 0.45 mm. The beams are aligned to overlap at the position of the cloud at an angle of $\approx 0.5\,^\circ$. A true zero-order quarterwave plate (QWP) and a half wave plate (HWP) for 780 nm is placed in both pump beams to set the polarization. The atoms cooled by the MOT are initially in the $5S_{1/2}, F = 2$ ground level. Photons from the two near resonant pump beams are coherently scattered by the atoms into 762 nm and 795 nm photon pairs in the phase matched directions. The one and the two photon detunings of the pump lasers from the atomic resonances, $\Delta_1 =$ -

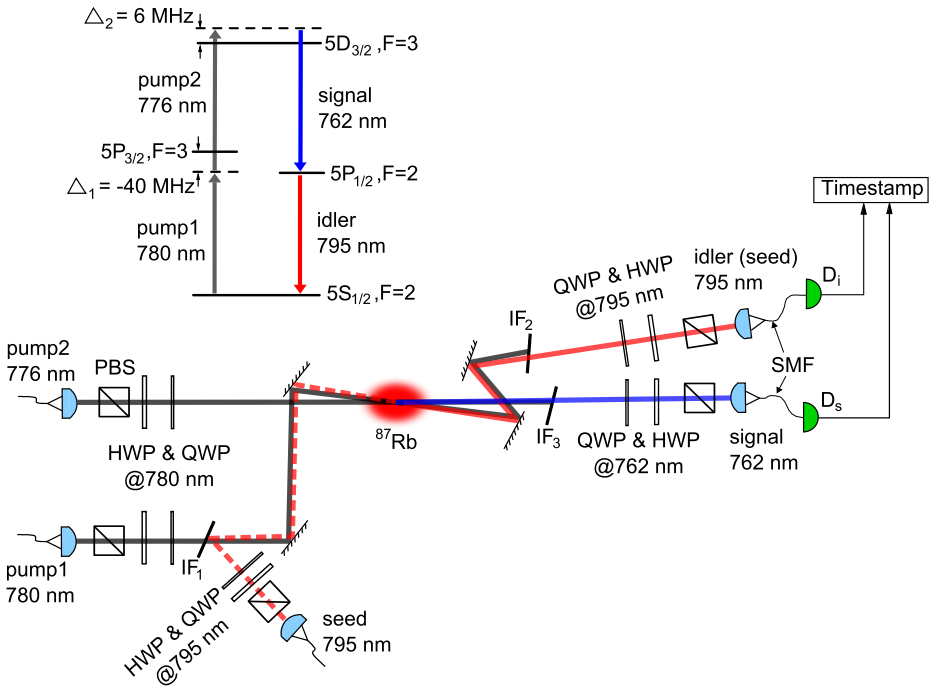

Figure 2.11: Schematic of the experimental set up. A combination of QWP, HWP and PBS is placed in all the optical modes to set or project the polarization. Interference filters IF_1, IF_2 and IF_3 are used to combine or filter the pump modes from the signal/idler modes. The APDs D_s and D_i are used to detect the single photons. A 795 nm seed beam is used during the alignment to determine the phase-matched direction.

40 MHz and $\Delta_2 = 6$ MHz, were chosen empirically to minimize incoherent scattering without compromising much on the photon pair rate. A seed beam of wavelength 795 nm shown as a dashed line is combined with the 780 nm pump using an interference filter IF_1. This beam is used only for alignment purposes and is switched off during the generation of pairs. The alignment of the source is discussed in detail in Section 2.3.3.

On the collection side, the interference filters IF_2 and IF_3 of bandwidth 3 nm are used to reject the residual pump light from the photon pairs. A QWP, a HWP and a PBS in the collection modes are used to choose the polarization of the signal and

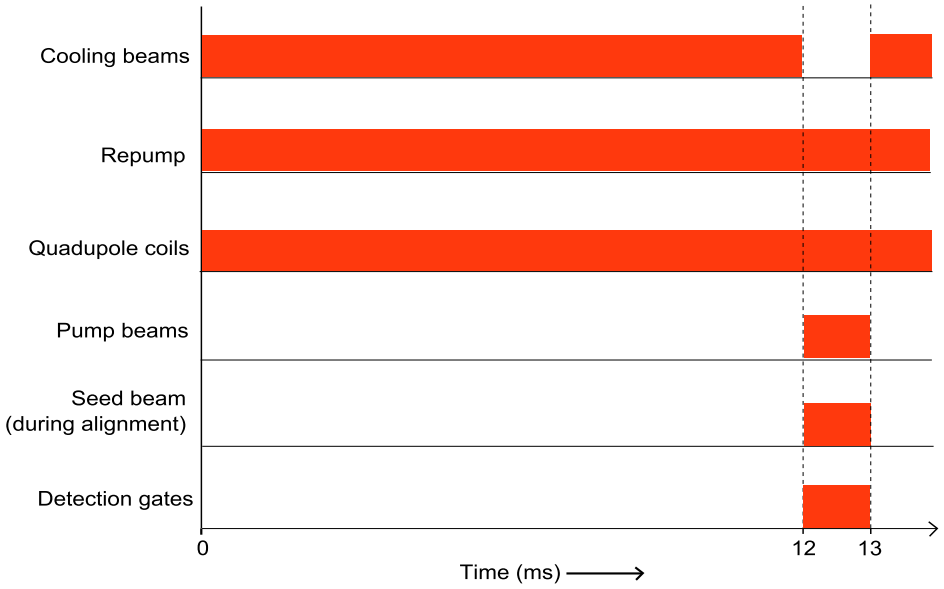

Figure 2.12: Experiment timing sequence.

the idler photons. Aspheric lenses of focal length 7.5 mm (Thorlabs A375-TME-B) are used in both the signal and idler modes to couple the photons into single mode fibers (SMF). The procedure used to couple signal and idler modes to the single mode fibers is discussed in Section 2.3.3. The effective waists of the collection modes at the location of the cloud were determined to be 0.4 mm and 0.5 mm for signal and idler respectively by back-propagating light through the fibers and couplers.

The photons are detected using Avalanche Photo-Diode (APD) single photon detectors from Perkin Elmer. The APD module and the associated electronics are home built, details of which can be found in [71]. The dark count rate of the APDs ranges between $40\,s^{-1}$ to $200\,s^{-1}$ and their detection efficiency is $\approx 40\%$. Whenever a photon is detected the APD module outputs a NIM signal, which is then sent to a timestamp unit. The timestamp unit records the arrival time of the NIM pulse with a resolution of 125 ps. The timing jitter of the APDs used in our experiment was measured to be 0.6 ns FWHM (see appendix C).

2.3.2 Timing sequence

The MOT cooling beams have to be switched off during the generation of photon pairs in order to prevent any incoherent scattering from cooling beams into the collection modes. However, the cold atom cloud obtained dissipates within a few milli-seconds after the cooling beams are turned off. This limits the photon pair generation time before which the atom cloud needs to replenished by turning the cooling beams back on. The timing sequence used in the experiment is shown in Figure 2.12. The 12 ms duration for cooling was chosen to maximize the average optical density of the cloud during the 1 ms photon pair generation window. The repump beam is kept on during the pair generation time to avoid the population of the $5S_{1/2}, F = 1$ ground level. The switching of the beams is done using the AOMs as described in Section 2.2.2. The sequence for switching is provided by a home built programmable pattern generator. The signals from the APDs to the timestamp unit are are electronically gated (Detection gates) such that only photons detected during the 1 ms pair generation time are registered.

2.3.3 Alignment procedure

For a given pump geometry, the photon pairs are generated only in the spatial modes that satisfy the phase matching condition described in Section 2.1.1. For a non-collinear geometry of the pump beams finding the correct collection modes for the photon pairs is not straight forward. We use a seed beam resonant to $5S_{1/2}, F = 2 \rightarrow 5P_{1/2}, F = 2$ transition overlapped with the 780 nm pump to define the idler mode. In this configuration, the phase matching condition is satisfied only when the signal mode is overlapped with the 776 nm pump.

In the presence of the three near resonant fields the atomic cloud acts as a parametric amplifier, generating a fourth coherent field of wavelength 762 nm resonant to the $5P_{1/2}, F = 2 \rightarrow 5D_{3/2}, F = 3$ transition in the direction of 776 nm pump. The spectrum of the generated beam measured using a grating spectrometer (Ocean optics - USB2000) is shown in Figure 2.13. A clear peak is visible at 762 nm. This generated light at 762 nm defines the signal mode.

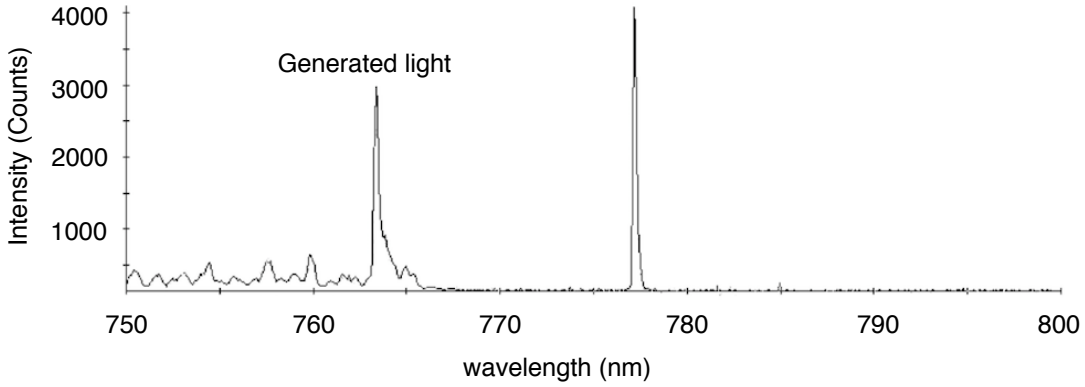

Figure 2.13: Wavelength of the FWM signal mode. The peak on the left is from the generated signal beam, and the one on the right is from the 776 nm pump. The spectrometer had an wavelength offset of 1 nm.

The angle between seed beam and 780 nm pump beam is then gradually increased to spatially separate the idler mode from the 780 nm pump mode. This changes the phase matching condition and hence changes the angle at which the signal beam is generated. This is illustrated in Figure 2.14 using a series of camera snapshots of the four participating modes in the FWM process. When the seperation angle is $\approx 0.5°$, the seed and the signal beams are coupled into the collection single mode fibers with a coupling efficiency of 80 % and 70 % respectively.

We performed some measurements to characterize the seeded operation of the source which are described in appendix B. A similar experiment of the seeded operation of the FWM was carried out by Willis et al. in [72].

2.4 Photon pairs

Once the source is properly aligned, the seed beam is switched off. The photon pairs generated in the defined signal and idler modes are now coupled into the collection fibers and are sent to the APDs for detection. The polarizations of the pump beams are set to

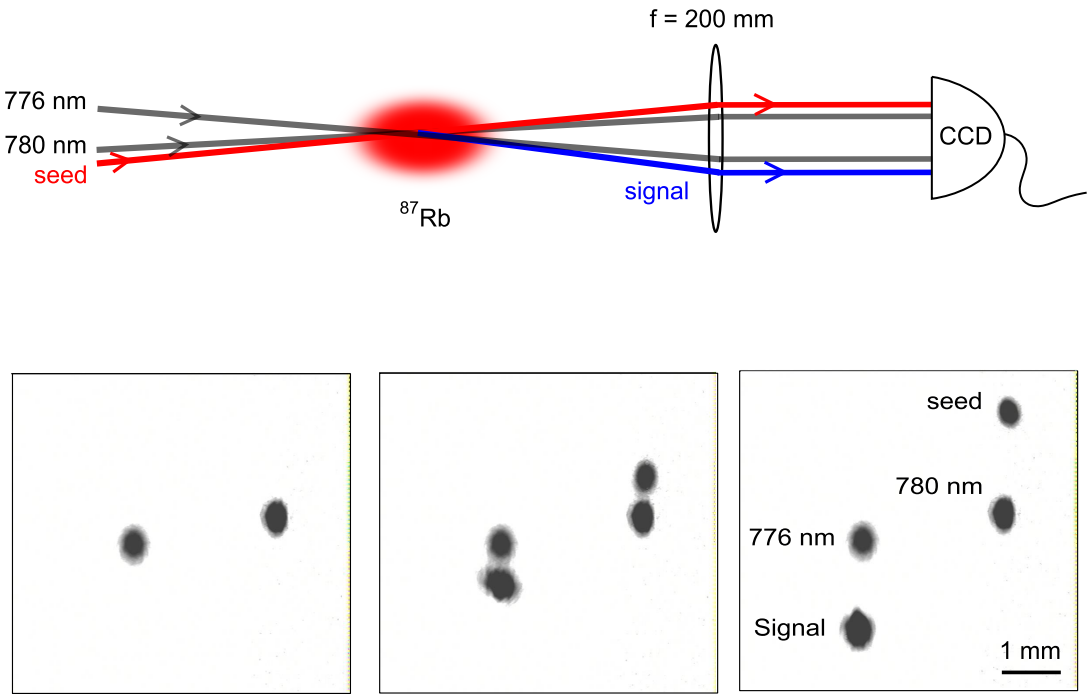

Figure 2.14: Observation of the phase matching using a CCD camera. (Top) Setup used to image the pump, seed and generated signal beams onto a camera. (Bottom) Images of the beams while changing the alignment. When the seed beam is overlapped with 780 nm pump, the generated signal is overlapped with the 776 nm pump. As the angle between the seed and the 780 nm pump is increased, the signal beam is generated at an angle with the 776 nm pump to satisfy phase matching condition.

horizontal (H) for 780 nm and vertical (V) for 776 nm. The measurement polarizations for the photons are set to H for signal, and V for idler. These polarization settings were chosen to maximize the FWM process efficiency as determined by operating the source as a parametric amplifier (see appendix B) and later confirmed by two-photon correlation measurements.

The histogram of coincidence events $G^{(2)}_{si}(\Delta t_{si})$ between the detection of signal and idler photons as a function of time delay (Δt_{si}) sampled into time bins of width $\Delta t =$

1 ns is shown in Figure 2.15 The normalized cross-correlation is defined as

$$g_{si}^{(2)}(\Delta t_{si}) = \frac{G_{si}^{(2)}(\Delta t_{si})}{r_i\, r_s\, \Delta t\, T} \quad , \tag{2.7}$$

where $r_{\rm i}$=2600 $\rm s^{-1}$ and $r_{\rm s}$=3100 $\rm s^{-1}$ are the idler and signal photons count rates, and T is the total time when the pump beams are on, i.e. 1/13 of the total measurement time (see Figure 2.12). The peak at $g_{si}^{(2)}(0)$ of 5800±124 indicates a strong temporal correlation with a very low background accidental coincidences. The measured $1/e$ decay time from the fit is 7.2±0.1 ns, which is lower than the single atom spontaneous decay time of 27 ns from the $5P_{1/2}, F = 2$ level. This is due to the superradiance effect in an optically thick atomic ensemble [73, 74]. More details of superradiance in the context of our experiment is described in appendix D.

A total photon pair detection rate r_P of this source can be derived from the measured $G_{si}^{(2)}(\Delta t_{si})$ by integrating over a coincidence time window Δt_c,

$$r_P = \frac{1}{T} \sum_{\Delta t_{si}=0}^{\Delta t_c} G_{si}^{(2)}(\Delta t_{si})\,, \tag{2.8}$$

For $\Delta t_c = 30$ ns, more than 98% of the pairs are captured. With pump powers of 5 mW at 776 nm, 100 μW at 780 nm, and detunings $\Delta_1 \approx -40$ MHz and $\Delta_2 \approx 6$ MHz, we obtain $r_P = 400\,\rm s^{-1}$ during the pair generation interval. Under these conditions, we find a signal heralding efficiency $\eta_s = r_p/r_s = 14.9\%$, and an idler heralding efficiency $\eta_i = r_P/r_i = 12.9\%$.

The pair rate can be increased by increasing the pump power or by reducing the two photon detuning (Δ_2), but at the expense of reducing the heralding efficiency. We observe a maximum pair rate of 18000 $\rm s^{-1}$ with pump powers of 15 mW for 776 nm, 300 μW for 780 nm and the two photon detuning of $\Delta_2 = 0$. However the heralding efficiency is reduced to $\eta_s = 7\,\%$, and $\eta_i = 5\,\%$. This is due to increased incoherent scattering when the pump beams are on resonance to the atomic transition [75]. Systematic measurements of pair rate and efficiency by changing various experimental parameters

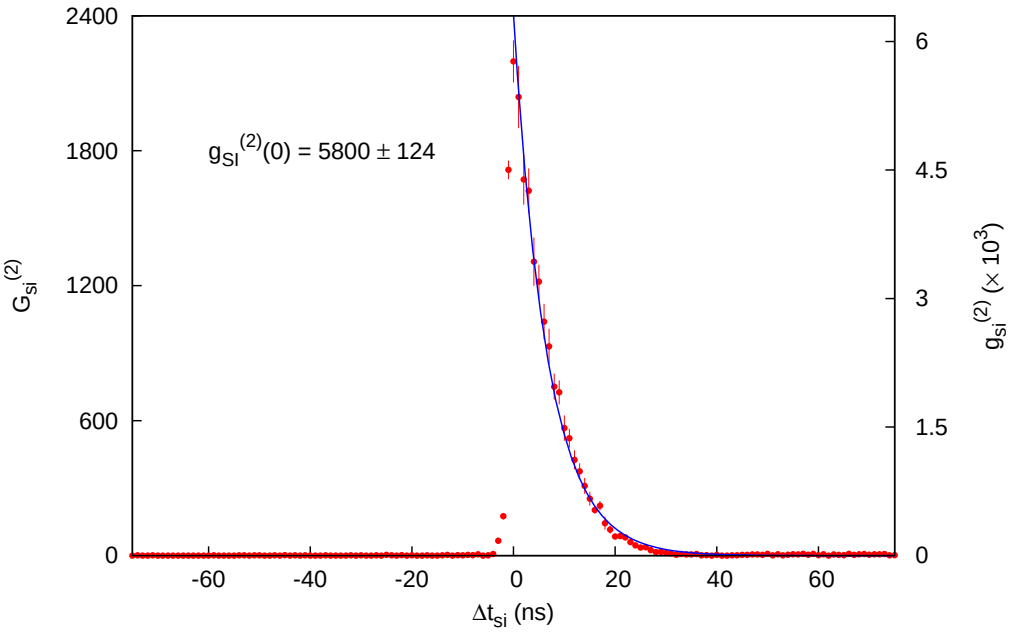

Figure 2.15: Histogram of coincidence events $G_{si}^{(2)}(\Delta t_{si})$ as a function of time delay Δt_{si} between the detection of idler and signal photons sampled into $\Delta t_{si} = 1\,\text{ns}$ wide time bins, and its normalized version $g_{si}^{(2)}$ according to Eq. (2.7). The total integration time T=47 s. The solid line is a fit to the model $g_{si}^{(2)}(\Delta t_{si}) = B + A \times \exp(-\Delta t_{si}/\tau)$, where $B = 1.20 \pm 0.07$ is the mean $g_{si}^{(2)}(\Delta t_{si})$ for Δt_{si} from 125 ns to 1μs, resulting in $A = 5800 \pm 124$ and $\tau = 7.2 \pm 0.1\,\text{ns}$.

are presented in [76].

2.4.1 Improving signal heralding efficiency by filtering

Two photon decay from the excited $5D_{3/2}, F = 3$ level to the hyperfine ground state $5S_{1/2}, F = 1$ is an allowed electric dipole transition (see Figure 2.16). However, the photons from this decay path are not generated by a parametric process and they do not satisfy the phase matching condition. Therefore the photon pairs from this decay path are not emitted into the defined collection modes.

To verify this we used a scanning Fabry-Perot cavity to measure the spectrum of the idler mode. The cavity had a linewidth of $\approx 13\,\text{MHz}$ and a Free Spectral Range

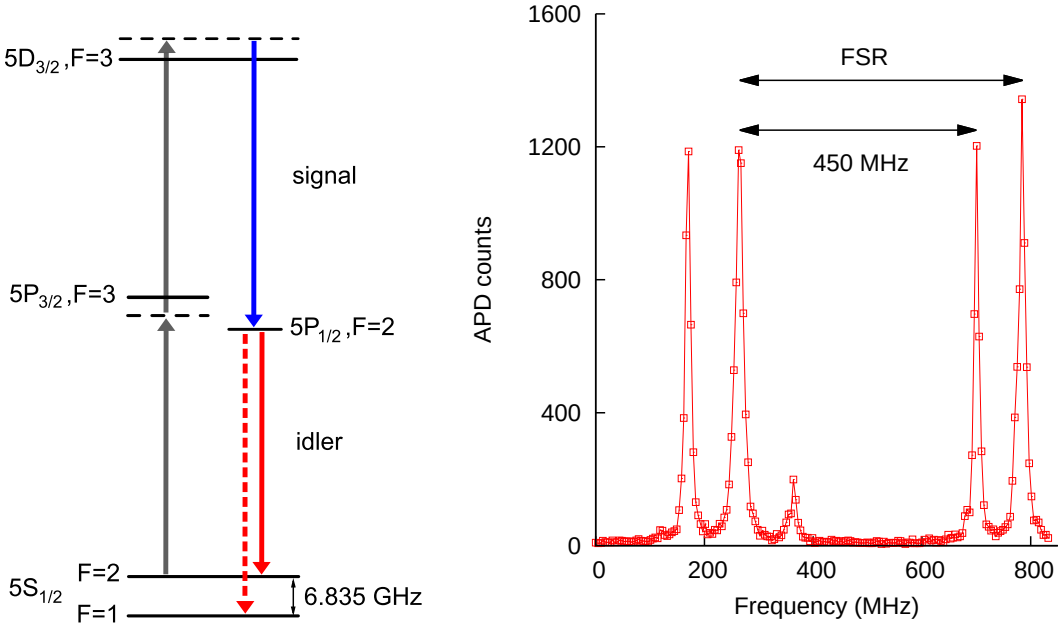

Figure 2.16: (Left) Level scheme showing the two allowed decay paths for idler. (Right) Spectrum of the light in idler mode measured using a scanning Fabry-Perot cavity. The two significant peaks corresponds to the two decay paths and the small peak is from the residual pump light.

(FSR) of $\approx 530\,\mathrm{MHz}$. The cavity transmission spectrum of the photons in the idler mode measured using APDs is shown in Figure 2.16. We observe two major peaks corresponding to the two allowed decay paths. The measured frequency difference between the two peaks is 450 MHz, which agrees with the expected separation between the two hyperfine levels of $6.83\,\mathrm{GHz}\,(= 12\,\mathrm{FSR} + 470\,\mathrm{MHz})$.

Next we measured the coincidences $G^{(2)}_{si}$ between signal and idler by tuning the cavity to transmit the photons from either of the two decay paths. As expected we observe concincidences only for the decay path that brings the atom back to $F = 2$ ground level (see Figure 2.17). The photons from the other decay path contributes only to the single detection events and not to the pairs. This implies that the heralding efficiency of the signal photons, η_s can be improved if we filter out the uncorrelated idler photons from the $5S_{1/2}, F = 1 \rightarrow 5P_{1/2}, F = 2$ decay path.

We use a temperature-tuned solid fused-silica etalon of linewidth 375 MHz (FWHM),

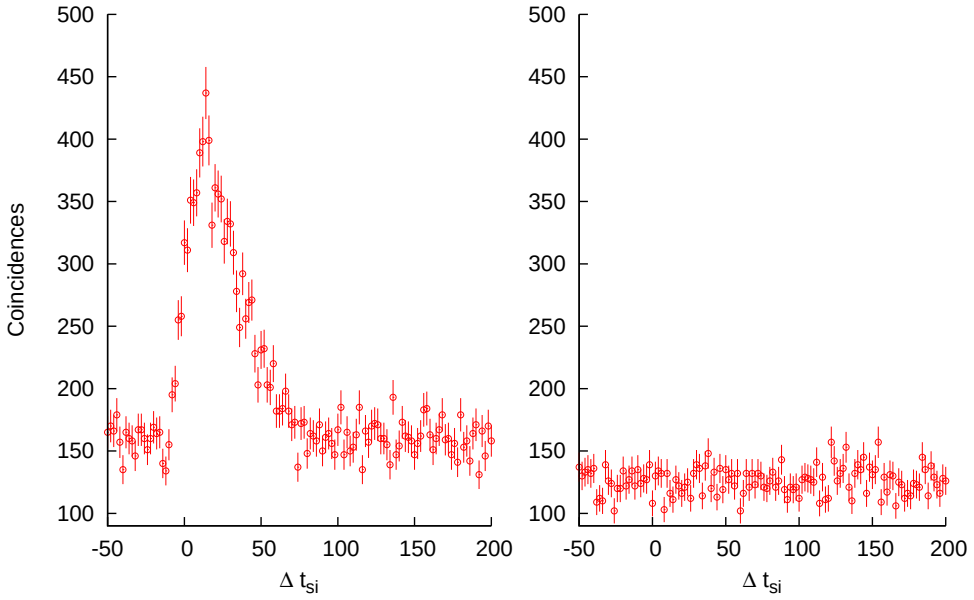

Figure 2.17: (Left) Coincidences between signal and idler with the cavity tuned to transmit the photons resonant with $5S_{1/2}, F = 2 \rightarrow 5P_{1/2}, F = 2$ transition. (Right) Cavity is tuned to transmit photons resonant with $5S_{1/2}, F = 1 \rightarrow 5P_{1/2}, F = 2$ transition

and a peak transmission 86% in the idler mode to remove these uncorrelated photons. This improves the idler heralding efficiency η_{i} to 23%.

2.4.2 Polarization entanglement

The photon pairs from our source are entangled in polarization due to the presence of spatially and temporally indistinguishable decay paths through different Zeeman states. The maximum polarization entanglement is obtained for orthogonal circular polarizations of the pump beams. This can be understood from the Clebsch-Gordan coefficients that define the relative coupling strengths between the different Zeeman states participating in the cascade decay process. A comprehensive theoretical description of polarization entanglement of the photon pairs from FWM in cascade decay can be found in [77]. We characterize the polarization state of our photon pairs by performing a quantum state tomography. Each QWP and HWP in the collection modes

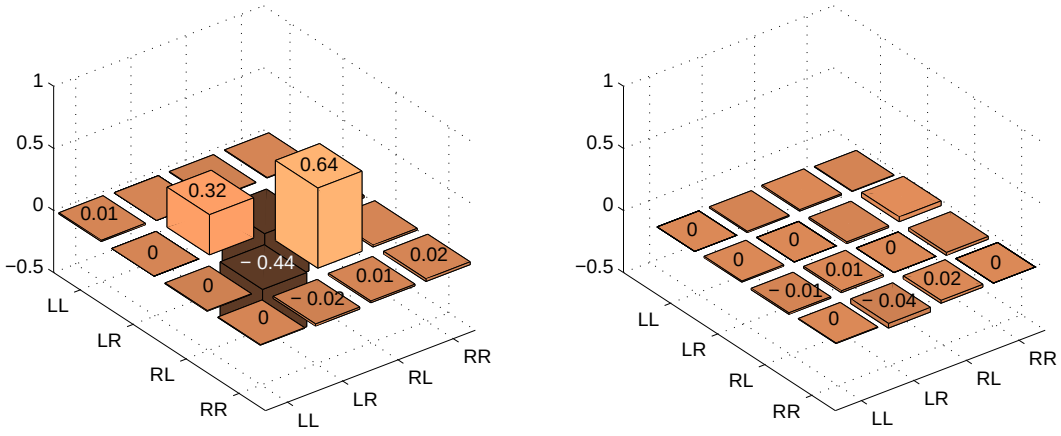

Figure 2.18: Polarization state of the photon pairs.(Left) Real part of the density matrix. (Right) Imaginary part of the density matrix.

are mounted on rotation stages controlled by stepper motors. We then measure the coincidences between signal and idler for 16 different waveplate angles, corresponding to 16 measurement polarization settings shown in the Table 2.1. The event rates for normalization are obtained by collecting the 795 nm fluorescence from the atom cloud without any polarization projection. This is used to correct for any fluctuations in photon pair rate due to the fluctuations in the pump beam powers, and the density of the atom cloud.

From these coincidences we reconstruct the polarization state of the photon pairs generated from the atom cloud using a maximum likelihood algorithm [78]. The resulting density matrix of the state is shown in Figure 2.18.

$$\rho = \begin{pmatrix} 0.010 & -0.010i & -0.004+0.012i & 0.004-0.003i \\ 0.010i & 0.323 & -0.436-0.014i & -0.016+0.038i \\ -0.004-0.012i & -0.436+0.014i & 0.645 & 0.014-0.023i \\ 0.004+0.003i & -0.016-0.038i & 0.014+0.023i & 0.022 \end{pmatrix} \tag{2.9}$$

The degree of entanglement can be quantified by entanglement of formation E_f. It is

Measurement Polarization		Coincidences	Normalization counts
Signal	**Idler**	(in 3 min)	(in 3 min)
L	L	82	67478
L	R	2417	61617
R	R	111	63529
R	L	5228	66241
-	L	2520	65796
-	R	1118	66488
H	R	1341	70638
H	L	2775	68862
H	-	2110	73960
H	H	219	70812
-	H	2109	70179
L	H	1440	69350
R	H	2738	65702
R	+	2736	71610
L	+	1301	64502
-	+	3543	65982

Table 2.1: Polarization tomography measurements. The first two columns show the polarization projections on signal and idler modes with H : Horizontal, + : 45° linear, - : -45° linear, L : Left circular, and R : Right circular polarization. The number of coincidences and normalization counts for each polarization projections are given in the third and the fourth columns respectively.

defined as the minimum number of singlets needed to create an ensemble of pure states that represents ρ [79], and it ranges from 0 for a completely separable state to 1 for a maximally entangled state. Our photon pairs exhibits a high degree of entanglement with $E_f = 0.8$. Another important measure of an entangled state is its purity,

$$P = Tr[\rho \cdot \rho] \tag{2.10}$$

where Tr refers to the trace of a square matrix, and P ranges from 0 for a totally mixed state to 1 for a pure state. We measure a purity of $P = 0.94$ for the state ρ. The closest pure state to ρ is $|\psi\rangle = 0.57|LR\rangle - 0.82|RL\rangle$ with a fidelity of 0.95.

2.5 Conclusion

In this chapter, we presented a photon pair source based on fourwave mixing in a cold ensemble of ^{87}Rb. We started by describing the essential tools including the lasers, spectroscopy, the magneto optical trap and the optical elements used in the experiment. We then presented the cross correlation measurement $g_{si}^{(2)}$ as a proof of the photon pair generation, and a complete state tomography to quantify entanglement in polarization between the photons. The high normalized cross correlation $g_{si}^{(2)}$ value clearly indicates the non-classical nature of the photon pairs, and a low background rate. This makes our photon pairs well suited for a heralded single photon source as discussed in the next chapter.

Chapter 3

From photon pairs to single photons

A "true" single photon can be defined as fluorescence from a single quantum emitter initially prepared in an excited state. Such sources of single photons rely on isolating and imaging single quantum particles that can emit only one photon per excitation. Single photons of this nature have been observed from single atoms [80, 81], ions [82], molecules [83, 84], quantum dots [85, 86, 87], and colour center in diamonds [88, 89]. In order to achieve a high rate and collection efficiency of the photons into a single optical mode, the emitter typically needs to be confined at the focus of high numerical aperture (NA) lenses. In a cavity QED context, single photons with relatively high collection efficiency have been observed using cavity-driven Raman transitions with single atoms [90, 91] and quantum dots [92]. These systems also require the particles to be confined within a high finesse optical cavity. These sources are also known as "deterministic" single photon sources because the photons can be generated on-demand by deterministically exciting the particle.

An experimentally simpler and efficient way of generating single photons is to use photon pair sources based on parametric conversion process such as the one described in the previous chapter. Since the photons are generated in pairs the detection of one

photon in the signal mode "heralds" the preparation of a single photon in the idler mode, and vice versa. This kind of single photon sources are known as "heralded" or "probabilistic" sources, as the spontaneous parametric process is intrinsically probabilistic. The advantage of such a single photon source over a deterministic source is that the photons are emitted in well defined spatial modes due to the phase matching condition (see Section 2.1.1), thereby eliminating the need for high NA optics. Single photons of this kind have been prepared from various physical systems such as nonlinear optical crystals [93], atomic ensembles [50, 94], photonic crystal fibers [95], Si waveguides [96] etc.

In this chapter, we present the experiments performed to characterize the heralded single photons from our pair source. In Section 3.1 we discuss the correlation measurement that shows the generation of single photons. The bandwidth measurement of the photons using a Fabry-Perot cavity is presented in Section 3.2. Finally the temporal field envelope of the heralded photons measured via homodyne detection is presented in Section 3.3.

3.1 Photon antibunching

The nature of any light source can be uniquely characterized by its coherence properties. Experimentally the coherence properties of light is measured by different order correlation functions as described by Glauber in his pioneering work [97]. We are interested in measuring the second-order autocorrelation function classically given by,

$$g^{(2)}(\tau) \;=\; \frac{\langle\, I(t)\, I(t+\tau)\,\rangle}{\langle I(t)\rangle^2}\,, \tag{3.1}$$

where $I(t)$ is the instantaneous intensity of the light field. For a classical light field the value of $g^{(2)}(0)$ is limited by the Cauchy-Schwarz inequality which applies to any pair of real numbers,

$$\langle I(t)^2\rangle \;\geq\; \langle I(t)\rangle^2\,. \tag{3.2}$$

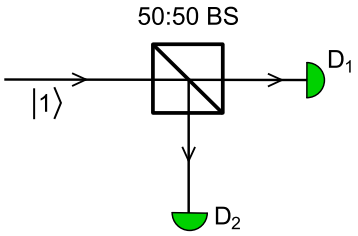

Figure 3.1: Hanbury–Brown–Twiss intensity interferometer used to measure the autocorrelation function $g^{(2)}$ of a single mode light. In our case the incident light to the BS is a single photon state.

By applying this condition to Eq. (3.1) it can be seen that $g^{(2)}(0) \geq 1$ for classical fields. However, the quantum description of light allows the violation of this inequality. For a single mode light the degree of second-order coherence in terms of the photon number distribution is given by [98]

$$g^{(2)}(0) = 1 + \frac{(\Delta n)^2 - \langle n \rangle}{\langle n \rangle^2}, \tag{3.3}$$

where $\langle n \rangle$ is the mean photon number in the mode and $(\Delta n)^2$ is the photon-number variance. A coherent light source exhibits Poissonian photon number statistics with $\langle n \rangle = (\Delta n)^2$, resulting in $g^{(2)}(0) = 1$. Any light source with $g^{(2)}(0) < 1$ exhibits a sub-poissonian photon statistics and the light is said to be "antibunched". A single photon Fock state has $\langle n \rangle = 1$ and $(\Delta n)^2 = 0$, resulting in $g^{(2)}(0) = 0$ for this state. This is a unique characteristic of an ideal single photon source with perfect antibunching. In this section we measure the $g^{(2)}(0)$ for the photons from our source to see how close we are to this ideal case.

3.1.1 Hanbury-Brown-Twiss setup

Experimentally the $g^{(2)}$ of a single mode light is measured using a Hanbury-Brown-Twiss (HBT) interferometer. The setup consists of a 50/50 beam splitter (BS) and an APD each at the two output port of the BS, D_1 and D_2 (figure 3.1). The $g^{(2)}$ is obtained from the probability of coincidence between the clicks from both detectors($P_{1,2}$) and

the probability of independent clicks (P_1 and P_2) on each detector.

$$g^{(2)} = \frac{P_{1,2}}{P_1\,P_2} = \frac{G^{(2)}_{1,2}}{s_1\,s_2\,\Delta t_c\,T}\,, \tag{3.4}$$

where $G_{1,2}$ is the total number of coincidences in measurement time T, s_1 and s_2 are the count rates on D_1 and D_2, and Δt_c is the width of the coincidence time window used for $G^{(2)}_{1,2}$.

Since a single photon from a heralded source is defined only with the detection of a heralding photon, the probabilities in Eq. (3.4) should be conditioned on the detection of a heralding event [99]. For the heralded idler mode the normalized $g^{(2)}$ is given by,

$$g^{(2)}_{i1,i2|s} = \frac{P_{i1,i2|s}}{P_{i1|s}\,P_{i2|s}} = \frac{P_{i1,i2,s}\,P_s}{P_{i1,s}\,P_{i2,s}} = \frac{G^{(2)}_{i1,i2,s}\,N_s}{G_{s,i1}\,G_{s,i2}}\,, \tag{3.5}$$

where $G_{i1,i2,s}$ is the number of triple coincidence events between the signal and the two idler modes, $G_{i1,s}$ and $G_{i2,s}$ are the number of pair events between signal and each of the idler modes, and N_s is the total number of heralding events in the signal mode. Bayes' theorem from probability theory is used in the above equation to convert the conditional probabilities to joint probabilities, which is subsequently converted to the number of coincidences.

The experimental setup used to perform this measurement is shown in Figure 3.2. The model in Eq (3.5) for obtaining $g^{(2)}$ works for coincidence window Δt_c much greater than the coherence time of the single photons. The photons generated from our source have a long enough coherence time ($\tau \approx 7\,\text{ns}$) that shape of the $g^{(2)}_{i1,i2,s}$ can be temporally resolved using APDs with a jitter time of 0.6 ns (see appendix C) The $G^{(2)}_{i1,i2,s}$ can now be resolved as a function of the time difference $\Delta t_{i1,i2}$ between the detection events on D_1 and D_2. The terms in the denominator of Eq (3.5), $G_{s,i1(i2)}$, have a strong dependence on the time delay $\Delta t_{s,i}$ between the signal and the idler photon (see Section 2.4). Therefore the normalization term for every time delay $\Delta t_{i1,i2}$ is determined by integrating the denominator in Eq (3.5) over all possible delays of

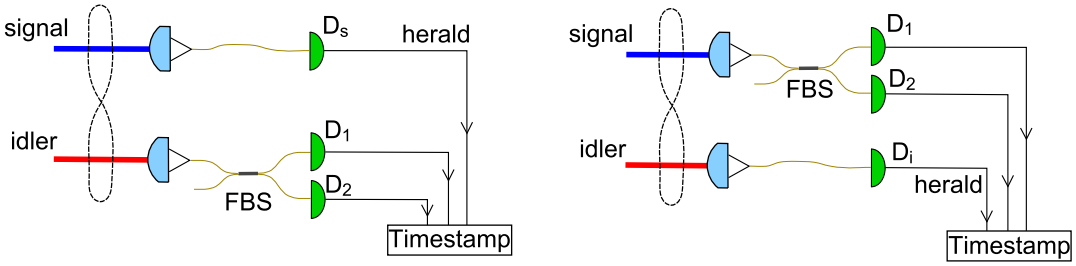

Figure 3.2: Experimental setup for heralded $g^{(2)}$ measurement with FBS: 50/50 fiber beam splitter, D_s, D_s, D_1, D_1 : APDs. (Left) Experimental setup to measure $g^{(2)}$ on the idler mode. The detection of the signal photon acts as a herald. (Right) Setup for $g^{(2)}$ on the signal mode with idler detection acting as a herald.

$\Delta t_{s,i}$ that result in a delay $\Delta t_{i1,i2}$ between D_1 and D_2. Moreover, due to the time ordering of the cascade process, it is only meaningful to consider positive time delays after the detection of the signal photon, thus splitting the denominator $N_{i1,i2|s}$ into two cases. For $\Delta t_{i1,i2} \geq 0$, we use

$$N^{(+)}_{i1,i2|s}(\Delta t_{i1,i2}) = \int_0^{30\,\mathrm{ns}} G^{(2)}_{s,i1}\left(\Delta t_{si}\right) G^{(2)}_{s,i2}\left(\Delta t_{si} + \Delta t_{12}\right)\, d\Delta t_{si}\,, \tag{3.6}$$

while for $\Delta t_{i1,i2} < 0$, we use

$$N^{(-)}_{i1,i2|s}(\Delta t_{i1,i2}) = \int_0^{30\,\mathrm{ns}} G^{(2)}_{s,i1}\left(\Delta t_{si} + \Delta t_{12}\right) G^{(2)}_{s,i2}\left(\Delta t_{si}\right)\, d\Delta t_{si}\,. \tag{3.7}$$

The integration window of 30 ns ($> 4\tau$) was chosen such that more than 98 % of generated pairs are considered for the measurement. The time resolved $g^{(2)}$ is then given by,

$$g^{(2)}_{i1,i2|s}(\Delta t_{i1,i2}) = \frac{G^{(2)}_{i1,i2,s}(\Delta t_{i1,i2})\, N_s}{N(\Delta t_{i1,i2})}\,. \tag{3.8}$$

The normalized $g^{(2)}_s$ for heralded signal photons is obtained in a similar way by swapping the roles of signal and idler modes.

3.1.2 Results

The resulting $g^{(2)}_{i1,i2|s}(\Delta t_{12})$ is shown in Figure 3.3(a) as function of the delay $\Delta t_{i1,i2}$, sampled into 2 ns wide time bins. With a signal photon detection rate of $50000\,\mathrm{s}^{-1}$, we observe $g^{(2)}_{i1,i2|s}(0) = 0.032 \pm 0.004$. When switching the roles of the signal and idler arms, the resulting normalized correlation function shown in Figure 3.3(b) has a minimum $g^{(2)}_{s1,s2|i}$ of 0.018 ± 0.007 with an idler photon detection rate of $13000\,\mathrm{s}^{-1}$.

In both the cases we see a clear signature of antibunching with $g^{(2)}(0) \ll 1$. This shows that we prepare a very good approximation of an ideal single photon state in the signal mode upon the detection of a heralding photon in the idler mode, and vice versa.

3.2 Bandwidth of the idler photons

An indirect assessment of the bandwidth of the heralded idler photons can be obtained from the $g^{(2)}_{si}(\Delta t_{si})$ (Figure 2.15), since it is related to the Fourier transform of the spectral distribution. Assuming a transform-limited spectrum, we infer a bandwidth of $\Delta\nu = 1/(2\pi\tau) = 23.8 \pm 0.7\,\mathrm{MHz}$ (FWHM). In order to verify if the photons are indeed Fourier limited, we carry out a direct optical bandwidth measurement of idler photons with a scanning Fabry-Perot cavity.

3.2.1 The cavity

The cavity is formed by two high reflecting mirrors from ATFilms with specified reflectivity $R > 99.9\%$ at 780 nm and radius of curvature 50 mm. The mirrors are mounted on an Invar spacer temperature stabilized to within 10 mK fluctuation, and kept in a vacuum (6×10^6 mbar) to prevent frequency drift due to change in the refractive index of air. This design of the cavity was originally intended to have frequency drifts less than the linewidth of the cavity over the entire time of the bandwidth measurement. However the measured drift was of the order of 10 MHz over the period of an hour, probably due to the curing process of the epoxy used to attach the mirrors to the

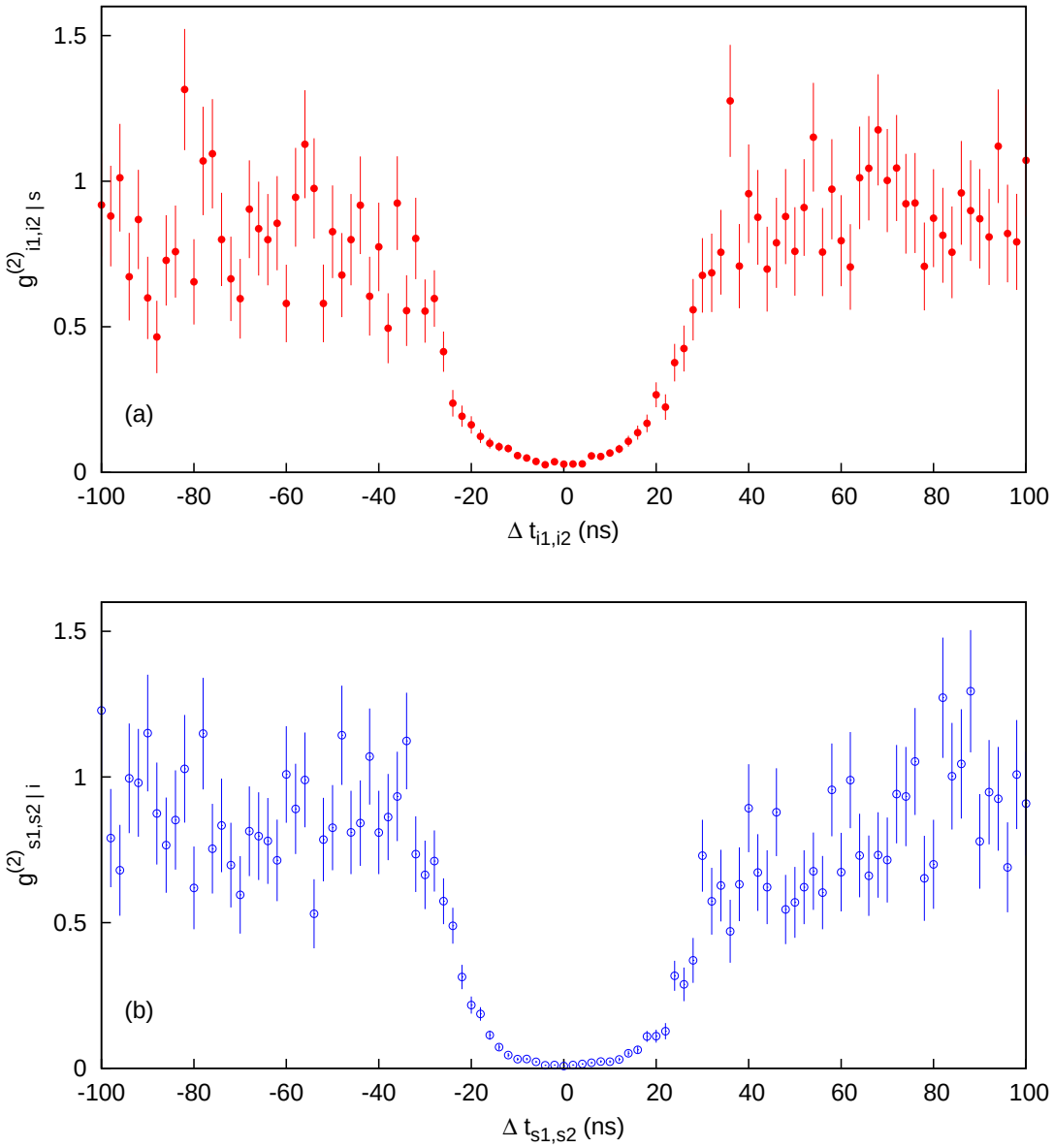

Figure 3.3: Photon antibunching. (a) The correlation function $g^{(2)}_{i1,i2|s}$ of idler photons separated by a time difference $\Delta t_{i1,i2}$, conditioned on detection of a heralding event in the signal mode, shows strong photon antibunching over a time scale of ± 20 ns, indicating the single photon character of the heralded photons. The error bars indicate the propagated Poissonian counting uncertainty from $G^{(2)}_{i1i2|s}$ and $N_{i1,i2|s}$. (b) Same measurement, but with the signal and idler modes swapped.

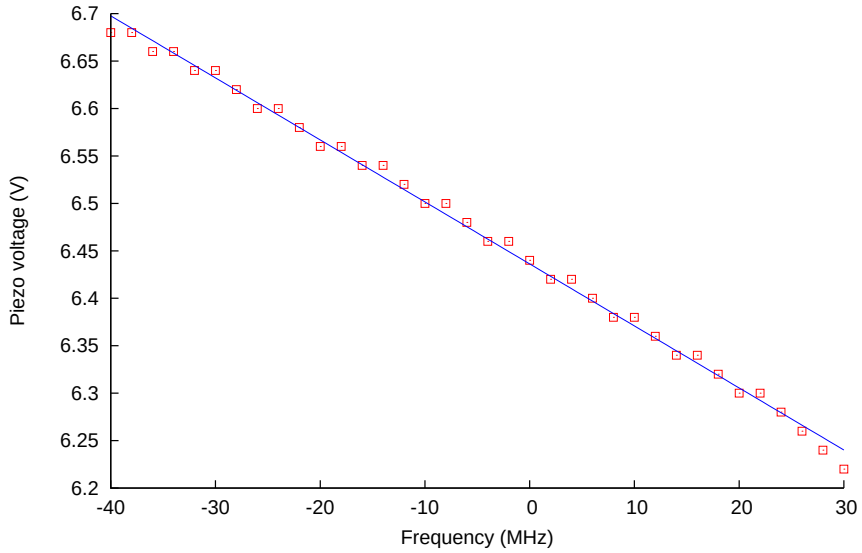

Figure 3.4: Input laser AOM detuning vs piezo voltage for maximum transmission through the cavity. The solid line is a linear fit of the form $V(\nu) = m \times \nu + V0$ where, $m = 0.00653\,\mathrm{V/MHz}$ and $V0 = 6.44\,\mathrm{V}$.

spacer. Therfore the design was modified to include a piezo tube attached to one of the mirrors to be able to tune and stabilize the transmission frequency of the cavity via feedback.

We determine the transfer function between the applied voltage to the piezo tube and the frequency shift of the transmission peak by using a locked 795 nm laser, frequency tuned by an AOM. This transfer function is later used to convert the measured bandwidth of the idler photons from piezo voltage to frequency. The AOM frequency is scanned in steps of 2 MHz, and for each step the piezo voltage that results in a maximum transmission of the laser through the cavity is determined. The result of this measurement is shown in Figure 3.4. The transfer function is determined by a linear fit to be 153 MHz/V.

The idler photons from a single mode fiber is mode matched to the fundamental TEM_{00} transverse mode of the cavity using an aspheric lens of focal length 4.5 mm (Thorlabs C230-TMB) and a 150 mm plano convex lens. The cavity length is stabilized via a feedback to the piezo voltage by monitoring the transmission of a 795 nm refer-

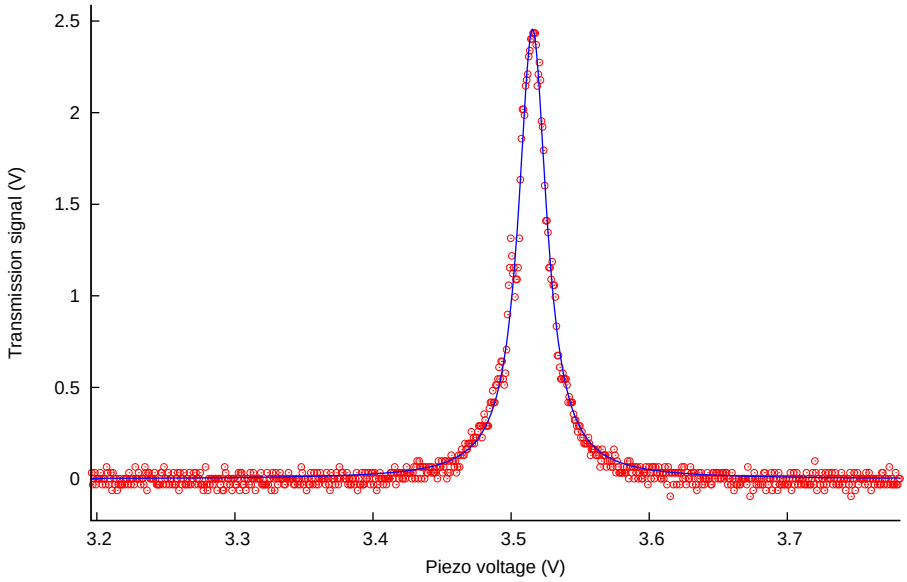

Figure 3.5: The cavity transmission as a function of applied piezo voltage. The solid (blue) line indicates a fit of the form y(x)=$\frac{a}{\gamma^2+4(x-x0)^2}$ where the FWHM linewidth $\gamma = 0.0247\,\mathrm{V}$. We use the transfer function from Figure 3.4 to determine the frequency linewidth to be $3.78 \pm 0.12\,\mathrm{MHz}$.

ence laser coupled through the cavity. The reference laser is switched on only during the cooling cycle of the experiment (Figure 2.12). The linewidth of the cavity was measured using this reference laser by tuning the piezo as shown in Figure 3.5. The FWHM linewidth of $3.78 \pm 0.12\,\mathrm{MHz}$ is obtained from a fit of the experimental points to a lorentzian function. However, this is a convolved linewidth of the cavity and the reference laser, and therfore gives only an upper bound of the cavity linewidth.

The value of the cavity linewidth can be determined from the $G^{(2)}_{si}$ decay time of the idler photons transmitted through the cavity [100]. The piezo voltage was tuned such that the peak transmission frequency of one of the longitudinal modes match the idler photon central frequency. The coincidence time distribution ($G^{(2)}_{si}(\Delta t_{si})$) between the transmitted idler photons and the heralding signal photons is shown in Figure 3.6. The $G^{(2)}_{si}$ without the cavity has exponential time constant $\tau = 7.2\,\mathrm{ns}$ (figure 2.15). In the presence of the cavity this transforms into a much longer decay compatible with

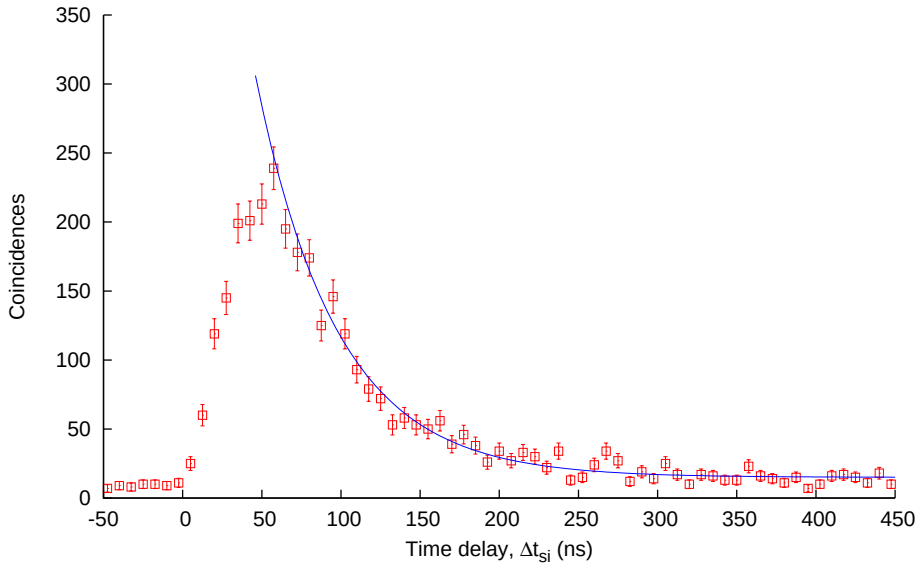

Figure 3.6: The cavity ringdown time measured with heralded idler photons. The blue line indicates a fit to an exponential decay function of the form $B + A \times e^{-(t-t0)/\tau'}$, where $B = 15$, $A = 327$, $t0 = 40\,\text{ns}$ and $\tau' = 51.3 \pm 3.5\,\text{ns}$. The fit is performed only on experimental points with $\Delta t_{si} > 80\,\text{ns}$.

the ring-down time of the cavity τ'. The linewidth of $\Delta\nu = 1/(2\pi\tau') = 3.1 \pm 0.2\,\text{MHz}$ is obtained by fitting the tail of the $G^{(2)}_{si}(\Delta t_{si})$ to an exponential function.

In order to measure the bandwidth of the idler photons, their transmission though the cavity is recorded using an APD and a timestamp unit while tuning the cavity resonance $\pm 50\,\text{MHz}$ around the $5S_{1/2}, F = 2 \rightarrow 5P_{1/2}, F = 2$ transition frequency.

3.2.2 Results

The result of the transmission measurement of the heralded idler photons with an atomic cloud $OD \approx 32$ is shown in figure 3.7(a). It can be seen that the bandwidth of the photons is broader than the natural line width of the $5S_{1/2}, F = 2 \rightarrow 5P_{1/2}, F = 2$ transition (6 MHz). This is due to a collective enhancement of the decay process from the intermediate level $5P_{1/2}, F = 2$ in an optically thick ensemble. This process is known as superradiance, discussed in more detail in appendix D. A fit of the obtained

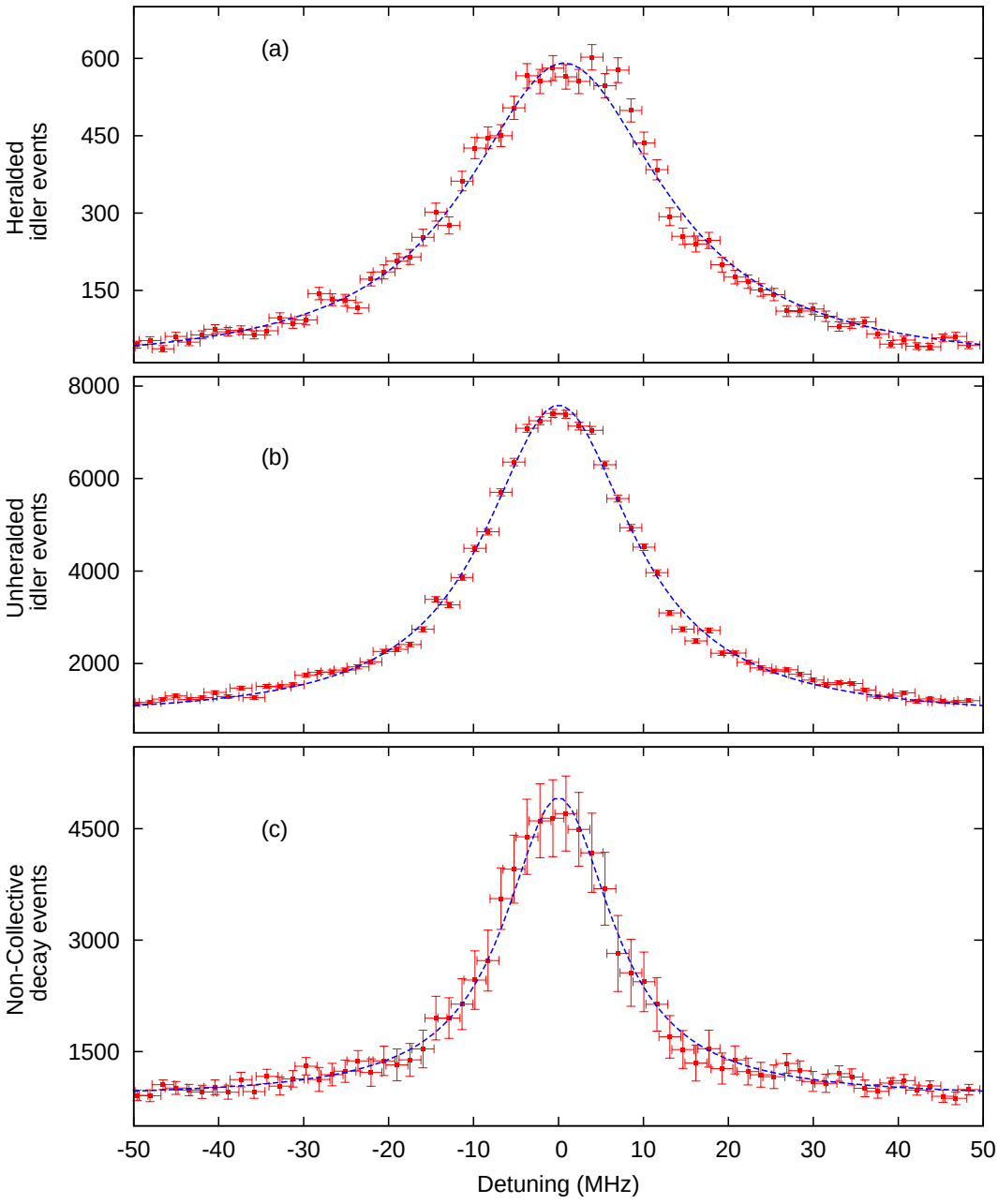

Figure 3.7: (a) Spectral profile of idler photons, heralded by the detection of signal photons with an atomic cloud $OD \approx 32$. The frequency uncertainty is due to the uncertainty in voltage driving the cavity piezo. The line shows a fit to a model of Lorentzian-shaped photon spectrum, convoluted with the cavity transmission spectrum. The fit gives a bandwidth of 24.7 ± 1.4 MHz (FWHM). (b) Same as (a), but without heralding. The resulting bandwidth from the fit is 18.3 ± 1.3 MHz (FWHM). (c) Inferred idler spectrum from the incoherent (non-superradiant) decay with 12.4 ± 1.4 MHz (FWHM) bandwidth from a fit.

spectrum to a Lorentzian line shape widened by the cavity transfer function leads to a bandwidth of $24.7 \pm 1.4\,\mathrm{MHz}$ (FWHM) for the idler photons, if they are heralded by a signal photon.

However, the observed spectrum of all light in the idler mode (i.e., the unheralded ensemble) shows a narrower bandwidth of $18.3 \pm 1.3\,\mathrm{MHz}$ (FWHM). This may be explained by incoherent (non-collective) contributions to light emitted via the collectively enhanced decay collected in phase-matched directions. The optical bandwidth of light from the collective decay contribution should increase with the atom number N due to an enhanced cascade decay rate, while the bandwidth of light from the incoherent contribution should remain the same. We can infer its spectrum by subtracting the heralded idler spectrum from the unheralded idler spectrum after correction for losses in filters (11%), optical elements (7%), inefficient photo detectors (60%), polarization filters (12%), and fiber coupling (30%). The resulting spectrum for $OD \approx 32$ is shown in Figure 3.7(c), with a width of $12.4 \pm 1.4\,\mathrm{MHz}$ FWHM. This exceeds the natural line width expected for the incoherent decay, probably due to self-absorption in the atomic cloud.

The observed bandwidth γ of the heralded idler photons for different atomic densities is shown in figure 3.8(a). According to [101, 102], the variation of the emitted bandwidth γ due to collectively enhanced decay can be modeled by the relation

$$\gamma = \gamma_0(1 + \mu N)\,, \tag{3.9}$$

where $\gamma_0 = 2\pi \times 5.8\,\mathrm{MHz}$ is the natural line width of the $5P_{1/2}, F = 2 \rightarrow 5S_{1/2}, F = 2$ transition, N is the atom number and μ is a factor that corresponds to the geometry of the cloud. We find a linear increase of γ with OD which is compatible with this model, since μN is proportional to our measured OD. The solid line shows a fit with the proportionality factor between μN and OD as a free parameter. The estimated bandwidth from the $g^{(2)}_{si}$ decay time is shown in Figure 3.8(b). This bandwidth is comparable with the bandwidth measured using the cavity, indicating that the photons

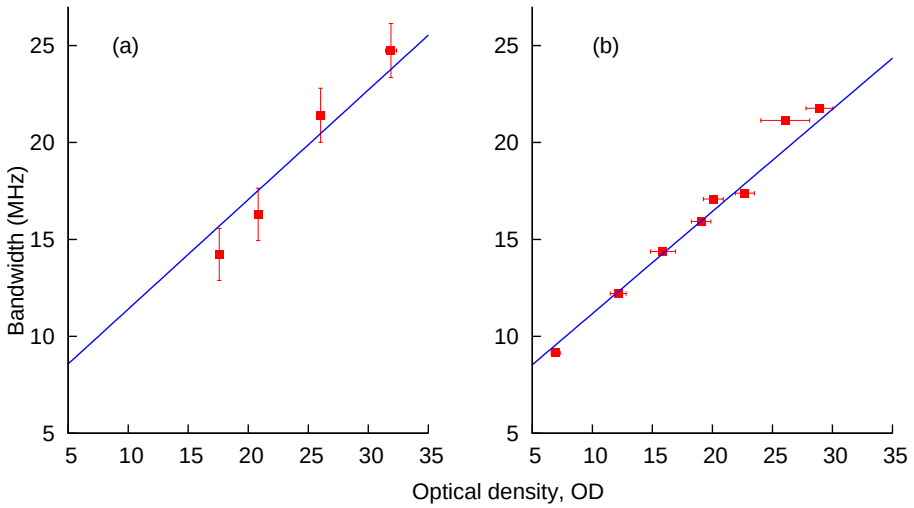

Figure 3.8: (Left) Bandwidth (FWHM) of heralded idler photons for different cloud optical densities (OD) measured wih the cavity. (Right) Bandwidth of heralded idler photons estimated from the $g^{(2)}_{si}$ decay time. The solid line shows the fit to the model (Eq (3.9)) with the slope as the only free parameter. The slope of the line is 0.098 ± 0.007 for (a), and 0.089 ± 0.005 for (b).

are indeed transform-limited.

3.3 Measuring the field envelope of the photons

The two-photon correlation in time ($g^{(2)}_{si}$) represents the probability of detecting one photon before or after detection of the herald (see Figure 2.15). In a cascade decay the correlation is not symmetric in time [98]. When using the signal photon as a herald, the temporal envelope of the idler photon shows a fast rise and a long exponential decay. We expect this envelope to be reversed in time when the idler serves as the herald, with an exponential rise instead of an exponential decay. We now complement this reasoning with a measurement of the heralded single photon field quadrature in the time domain [103, 104] via a balanced homodyne detection.

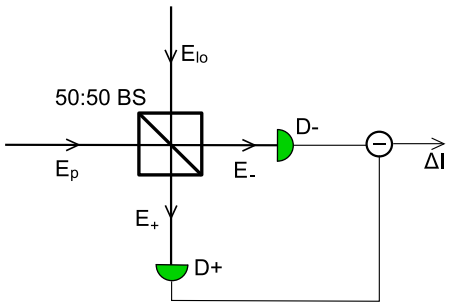

Figure 3.9: The basic elements for a homodyne detection. The field to be measured E_p is mixed with a strong local oscillator E_{lo} and detected using PIN photodiodes D+ and D-. The difference current ΔI is proportional to the field quadrature of E_p which is in phase with E_{lo}.

3.3.1 Homodyne detection

Homodyne detection is a well known technique used to measure the field quadrature of an electromagnetic mode. The basic elements of a balanced homodyne detection scheme is outlined in the figure 3.9. The mode carrying the field to be measured is mixed with a strong reference field (local oscillator LO) of same frequency on a 50/50 beam splitter (BS). The outputs of the beam splitter are detected by two PIN photodiodes and their currents subtracted.

The two incident fields on the BS are given by [55],

$$\begin{aligned} E_p(\vec{r},t) &= i\sqrt{\frac{\hbar\omega}{2V\epsilon_0}}\,(\hat{a}\,e^{i(\vec{k}.\vec{r}-\omega t)} - \hat{a}^\dagger\,e^{-i(\vec{k}.\vec{r}-\omega t)} \\ E_{lo}(\vec{r},t) &= i\sqrt{\frac{\hbar\omega}{2V\epsilon_0}}\,(\hat{b}\,e^{i(\vec{k}.\vec{r}-\omega t)} - \hat{b}^\dagger\,e^{-i(\vec{k}.\vec{r}-\omega t)}\,, \end{aligned} \tag{3.10}$$

where a and b are the photon annihilation operators which characterize the the two incident modes. The total field at the two output ports of the beam splitter,

$$E_\pm(\vec{r},t) = i\sqrt{\frac{\hbar\omega}{2V\epsilon_0}}\,(\hat{c_\pm}\,e^{i(\vec{k}.\vec{r}-\omega t)} - \hat{c}_\pm^\dagger\,e^{-i(\vec{k}.\vec{r}-\omega t)}\,, \tag{3.11}$$

where $\hat{c_{\pm}} = \hat{a} \pm i\hat{b}$ are the annihilation operators of the output modes of the BS.

The quantity measured by balanced homodyne detection is represented by the operator

$$\begin{aligned} \hat{M_H}(t) &= \int_t^{t+T} dt'(\hat{c}_+^\dagger(t')\hat{c}_+(t') - \hat{c}_-^\dagger(t')\hat{c}_-(t')) \\ &= i\int_t^{t+T} dt'(\hat{a}^\dagger(t')\hat{b}(t') - \hat{b}^\dagger(t')\hat{a}(t')) \end{aligned} \tag{3.12}$$

where T is the integration time. The local oscillator is assumed to be a single mode coherent light beam characterized by complex amplitude

$$\alpha(t) = \sqrt{F}e^{-i\omega t + i\theta} \tag{3.13}$$

where F is the time-independent mean photon flux, and θ is the phase.

The difference current of the two detectors is given by

$$\langle \Delta I(t)\rangle \propto \langle \hat{M_H}(t)\rangle = i\sqrt{F}\int_t^{t+T} dt'\langle \hat{a}^\dagger(t')e^{-i\omega t' + i\theta} - \hat{a}(t')e^{i\omega t' - i\theta}\rangle \tag{3.14}$$

$$= 2i\int_t^{t+T} dt'\langle \hat{X}\cos(\omega t' - \theta) + \hat{P}\sin(\omega t' - \theta)\rangle \tag{3.15}$$

where $\hat{X}$ and $\hat{P}$ are quadrature field operators. It can be seen that the mean difference current is proportional to the quadrature phase amplitude of the signal mode defined with respect to the local oscillator phase θ. The LO phase is generally defined by phase locking the LO to the pump lasers. This is essential for the experiments on quantum state reconstruction in quadrature phase space [105, 106]. However, we are only interested in measuring the time variation of the field amplitude of a single photon Fock state. It is well known that the quadrature phase amplitude of a single photon Fock state is independent of the phase θ [98]. This is illustrated in figure 3.10. Therefore our experiment does not require such a phase lock for the LO.

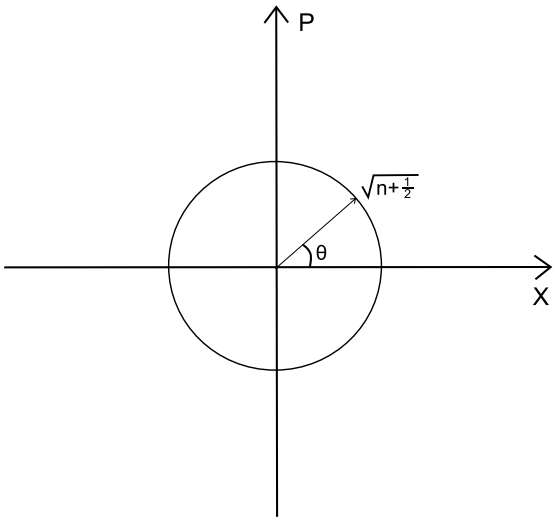

Figure 3.10: Representation of quadrature field operator expectation values for the Fock states. The expectation value is independent of the local oscillator phase θ.

3.3.2 Detector characterization

The homodyne detector unit consists of two Si PIN photodiodes (Hamamatsu S5972) connected as shown in Figure 3.11 to measure the difference current ΔI. The responsivity and coupling of light to these diodes is determined to be 0.53 A/W by comparing the measured DC current with a reference photodiode. The sensitivity of the reference diode was measured by the National Metrology Center in A*STAR, Singapore to be 0.6027 ± 0.002651 A/W at 795 nm. The DC part of the difference current is suppressed by using a high pass filter with a cut-off frequency of 10 KHz. The AC part is amplified by a transimpedence amplifier (AD8015) of gain 5.7 kΩ. The output of the amplifier in this configuration is designed to drive a 100Ω load. A 2:1 transformer is used to convert the output impedance of the detector unit to drive a 50 Ω load instead.

Since we are interested in measuring the optical field at a single photon level, it is important to characterize the noise level of the homodyne detector. The detector noise can be classified into three broad categories:

- Electronic noise which is independent of the incident optical power. This includes

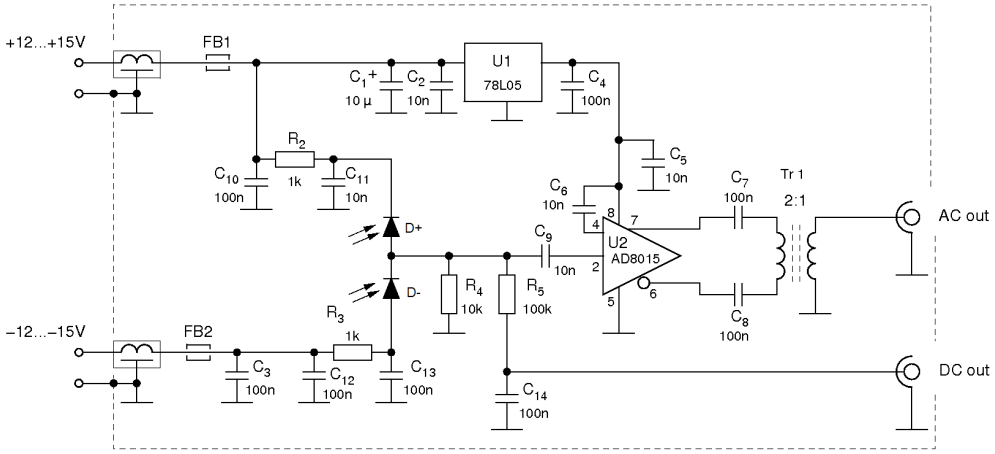

Figure 3.11: Circuit diagram of the homodyne detector with: Si photodiodes D+ and D-, a high pass filter HPF (C9,R4) with 3 dB cut-off frequency of 10 KHz, a transimpedance amplifier AD8015, and a 2:1 transformer for impedance matching with a 50 Ω line. The upper cut-off frequency of the AC port is limited by the amplifier at 210 MHz. The DC port is used to measure the difference DC current across the 10 KΩ load (R4).

the dark current of the detector and the thermal noise in the electronics.

- Classical noise which results from intensity fluctuations in the laser. This noise is negligible in the balanced homodyne detection as the intensity fluctuations cancel out in the difference current, ΔI.

- Shot noise which corresponds to the Poissonian photoelectron statistics. This is the fundamental detection limit. The variance of the photocurrent due to shot noise is given by $V(\Delta I) = 2e\Delta f\langle\Delta I\rangle$, where Δf is the frequency bandwidth, and e is the charge of the electron.

The best signal-to-noise ratio can be achieved when the detector noise power is dominated by shot noise i.e., the detector is said to be shot noise limited. In this case,

$$P_{noise} \;=\; V(\Delta I)\, R_L\,, \tag{3.16}$$

where P_{noise} is the rms noise power of the homodyne current measured using a load

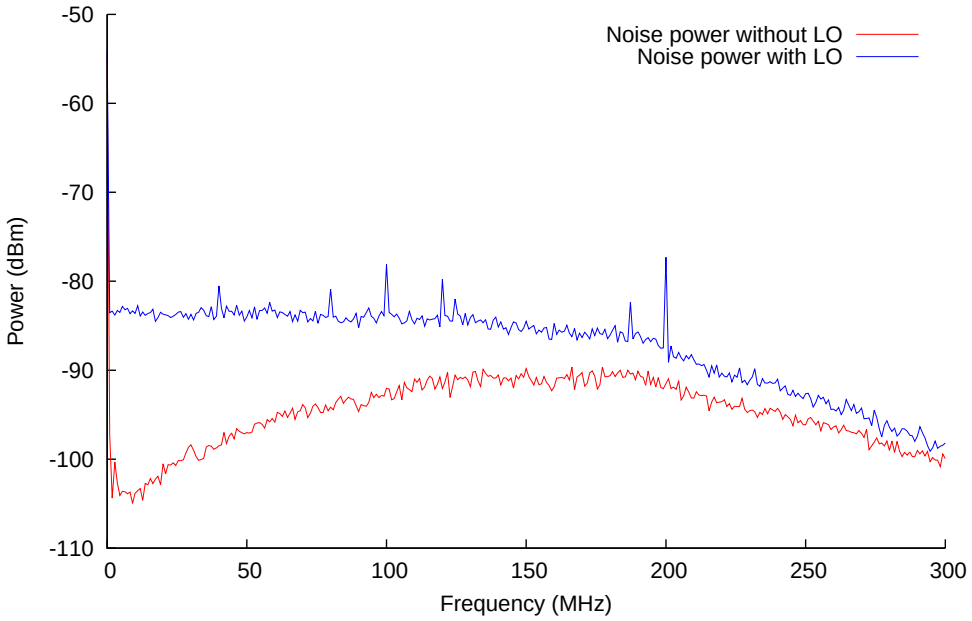

Figure 3.12: The spectrum of the electronic noise measured without LO (red) and the overall noise with LO of optical power 4.4 mW (blue). The resolution bandwidth of the spectrum analyzer was set to 10 KHz for both the measurements. The 3 dB bandwidth of the detector is determined from the blue curve to be 210 MHz. The relatively flat response of the noise within the detector bandwidth is characteristic of the Shot noise.

resistance R_L.

The characteristic features of shot noise are :

- The variance of the noise power is directly proportional to the average current, and therefore the incident optical power.
- The noise spectrum is independent of the frequency within the detection bandwidth.

The spectrum of the noise from our detector was measured with an Agilent 13 GHz spectrum analyzer (MS2723B) and is shown in Figure 3.12. The red line is the spectrum of the electronic noise obtained with no incident light onto the detectors. The blue line is the noise spectrum in the presence of the LO of optical power 4.4 mW. It can be seen

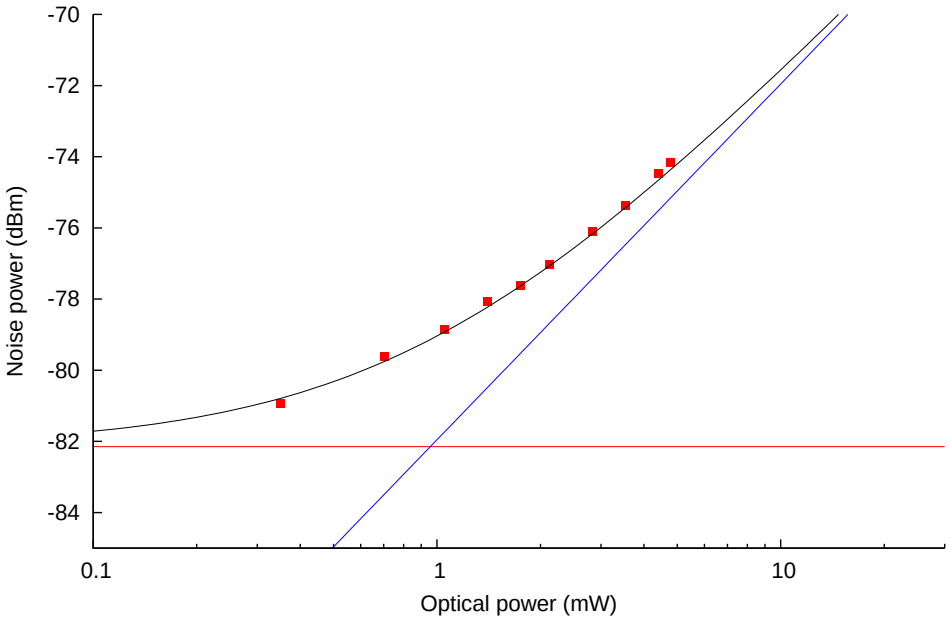

Figure 3.13: The detector noise power by varying the incident optical power of the LO on a log-log plot. The noise power (y-axis) is obtained from the average value of the spectrum analyzer trace (Figure 3.12) between 100 KHz to 200 MHz. The black line is a fit of the form: $P_{noise} = b + s \times P_{opt}$, where b=-82.15 dBm is the electronic noise level (red line) and s=10 dB/decade is the slope of the shot noise.

that the spectrum is reasonably flat in frequency within the detection bandwidth of 210 MHz, except for a few peaks [1]. The noise power in these peaks become negligible when integrating over the detection bandwidth.

The measured noise power of our detector as a function of the incident optical power is shown in Figure 3.13. The electronic noise is shown as a horizontal line at -82 dBm independent of the optical power, and the blue line represents the shot noise. We operate the detector at an incident optical power of $\approx$ 4.5 mW where the overall noise is dominated by the shot noise.

[1] The peaks are presumably from FM radio, and AOM drivers nearby

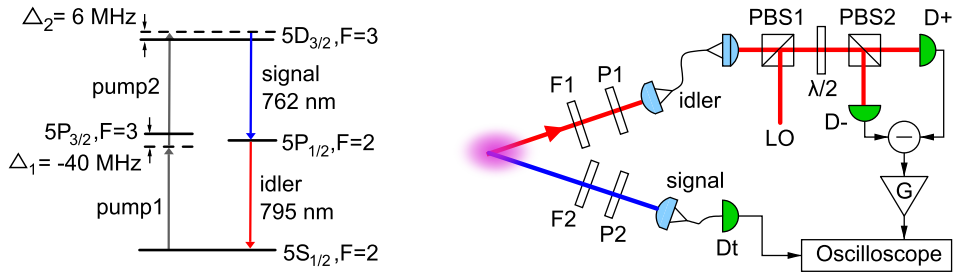

Figure 3.14: Field measurement setup. One of the photons (idler in this figure) is combined with a coherent laser field as a local oscillator on a polarizing beam splitter (PBS1), and sent to a balanced pair of PIN photodiodes D+, D- for a homodyne measurement. The photocurrent difference as a measure of the optical field strength is amplified and recorded with an oscilloscope triggered on the detection of a heralding signal photon by D_t.

3.3.3 Experimental setup

The experimental scheme is shown in Figure 3.14: the idler mode is mixed with a local oscillator (LO) which is frequency-stabilized to the idler transition $5S_{1/2}, F = 2 \rightarrow 5P_{1/2}, F = 2$. The balanced mixing is done with two polarizing beam splitters (PBS1,2) and a half-wave plate resulting in an interference visibility of $\approx 95\%$. The difference of photocurrents from the PIN silicon photodiodes (D+, D-) is proportional to the optical field quadrature in the idler mode. We record the homodyne signal with a digital oscilloscope (analog bandwidth 1 GHz), with the detection of the signal photon on D_t triggering the acquisition. We then calculate the variance of the optical field from 2.7×10^5 traces, normalized to the shot noise, as a measure of the temporal envelope of the photon. We also switched the roles of the signal and idler modes for triggering and homodyne detection, this time using a local oscillator resonant with the transition $5P_{1/2}, F = 2 \rightarrow 5D_{3/2}, F = 3$ near 762 nm. The variance for this measurement is calculated from 5×10^5 traces. Both results are shown in Figure 3.15. In both configurations, we set $\Delta_2 \approx 6$ MHz to maximize the heralding efficiency.

3.3.4 Results

In Figure 3.15(a) the normalized field variance of the idler photon suddenly rises about 4% above the shot noise level at the detection time of the trigger photon, and exponentially decays back to the shot noise level, with a time constant of $\tau_i = 7.2 \pm 0.2\,\mathrm{ns}$ obtained from a fit. This can be easily understood by the timing sequence of a cascade decay, where the signal photon heralds the population of the intermediate level, which subsequently decays exponentially, leading to the characteristic decaying envelope of the idler photon according to the Weisskopf-Wigner solution [107]. The probability of detecting an idler photon given the detection of a signal photon (heralding efficiency) was independently determined with two APDs to be $\eta_i \approx 13\%$.

In Figure 3.15(b) the normalized field variance of the signal photon exponentially increases a few 10 ns before the trigger event to a value of 1.06, and then quickly returns to the shot noise level. The time constant of the exponential part is obtained from a fit to be $\tau_s = 7.4 \pm 0.2\,\mathrm{ns}$. Here, the suppression of uncorrelated trigger (idler) photons by the etalon (see Section 2.4.1) results in a higher heralding efficiency $\eta_s \approx 19\%$, and therefore a higher signal to shot noise level. The measured value of decay time is compatible with our previous measurements of the distribution of detection time differences for this optical density.

From the results of the HBT experiment (see Section 3.1.2), we know that the idler detection witnessed a single photon in the signal mode to a very good approximation. We therefore have to conclude that the heralded signal field is a single photon state with an exponentially rising temporal envelope. In this case, however, the simple causal interpretation of the physical process in the Weisskopf-Wigner picture does not work [107]: the trigger time is fixed by the herald that leaves the atoms in the ground state, but the signal field starts to rise to a maximum before that. So the heralding process does not set an initial condition of a physical system that then evolves forward in time, but marks the end of a (signal) field evolution that is compatible with the exponential rise that started *before* the heralding event. Formally this is not a problem, because the heralding event just sets a different boundary condition. A single photon

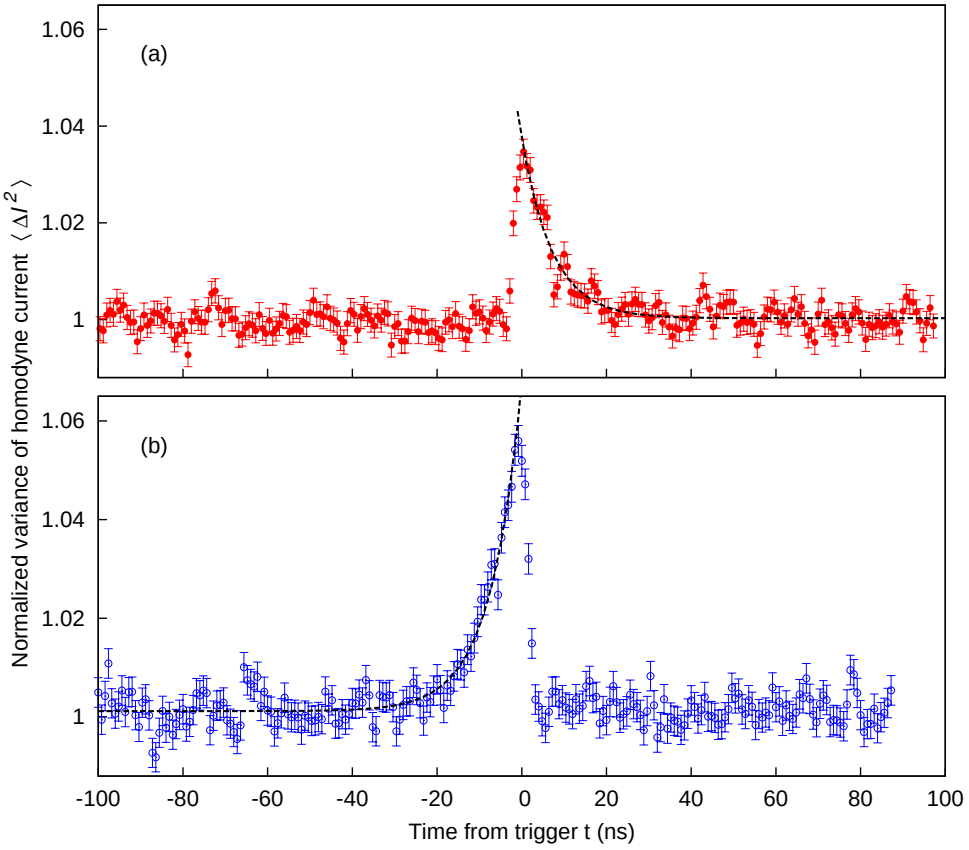

Figure 3.15: Optical homodyne results. (a) Exponential decay of the field variance of heralded idler photons. (b) Exponential rise of the field variance of heralded signal photons.

with such a rising exponential temporal envelope would be ideal for absorption by a two-level system, and to test the reversibility of the spontaneous emission process [18].

3.4 Conclusion

In this chapter, we have demonstrated a source of narrowband heralded single photons based on an ensemble of cold rubidium atoms. We observe antibunching with $g^{(2)}(0) < 0.03$, conditioned on detection of a photon in the signal (idler) mode. Depending on which of the modes is chosen as a herald, we find either an exponentially decaying or rising temporal envelope of the heralded photon.

If heralded single photons are practically not distinguishable from "true" single photons, the former should at least in principle be efficiently absorbed by a two-level system in free-space in a time-reversed Weisskopf-Wigner situation. Such an experiment also would provide a better understanding as to how equivalent heralded photons are to single photons emerging from a deterministic source with a well-defined initial condition. This test would require a photon driving a ground state transition of a two level system. The heralded photons with the exponentially rising waveform generated by our scheme are resonant with an excited transition and therefore cannot be used directly. In the next chapter, we address this problem of how to prepare a ground state resonant photon with an exponentially rising envelope.

Chapter 4

Interaction of single photons with a cavity

Absorption of a single photon by a single atom is an interesting problem from a fundamental point of view, and is also essential for many quantum information protocols [8, 108]. One of the requirements for an efficient absorption is that the temporal shape of the incident photon is the time reversal of the photon from the spontaneous decay process [19, 20]. Temporally shaped light pulses have been utilized in many recent experiments to achieve efficient interactions between light and matter [25, 109]. In particular, the advantage of using a rising exponential shaped single photon for absorption in an atomic ensemble was demonstrated in [110], and shaped multiphoton pulses for exciting a single atom was demonstrated in [24]. This advantage also applies to interacting single photons with other systems such as quantum dots [111, 112], single molecules [113] and superconducting circuits [22].

Efficient preparation of single photons with a rising exponential envelope is not trivial. One solution is the direct modulation of a heralded photon generated by an atomic medium [114]. This technique results in unavoidable losses due to filtering. In Chapter 3 we demonstrated a scheme to generate single photons with a rising exponential shape by heralding on photon pairs produced by cascade decay without

filtering. The drawback of this scheme is that the photon with the rising exponential envelope is not resonant with an atomic ground state transition.

We combine the asymmetric cavity design used by Bader et al. [21] with the well known temporal correlation properties of photon pairs [115] to invert the temporal envelope of the generated photon pairs. With a proper heralding sequence, we obtain rising exponential single photons resonant with a ground state transition of ^{87}Rb. This concept is not limited to atoms, but can equally be applied to other physical system with a cascade level structure to obtain such photons [116, 117, 118].

In this chapter, we discuss two related experiments. In the first experiment presented in Section 4.1, we reverse the temporal envelope of the heralded photons. In Section 4.2, we study the coupling of single photons with different temporal shapes to the cavity.

4.1 Reversing the temporal envelope

4.1.1 Concept

We first present an intuitive, though hand-waving description of how a cavity can be used to reverse the temporal envelope of the heralded photons. A more rigorous mathematical description is presented in the Section 4.1.2. Consider an asymmetric cavity with one mirror (M_2) with unit reflectivity and another partially reflecting mirror (M_1) with a reflectivity chosen such that the cavity ringdown time matches the coherence time of our photons (see Figure 4.1). A photon incident on the cavity at the mirror M_1 will either be directly reflected off the mirror or be coupled to the cavity mode. If the incident photon has a rising exponential temporal envelope matching the cavity lifetime, the probability amplitudes of the direct reflection and the leakage from the cavity mode through the mirror M_1 cancel out due to complete destructive interference. Therefore the incident photon is completely absorbed into the cavity mode, and subsequently decays exponentially through M_1. The exponentially rising envelope of the incident photon thus gets transformed into a decaying exponential envelope.

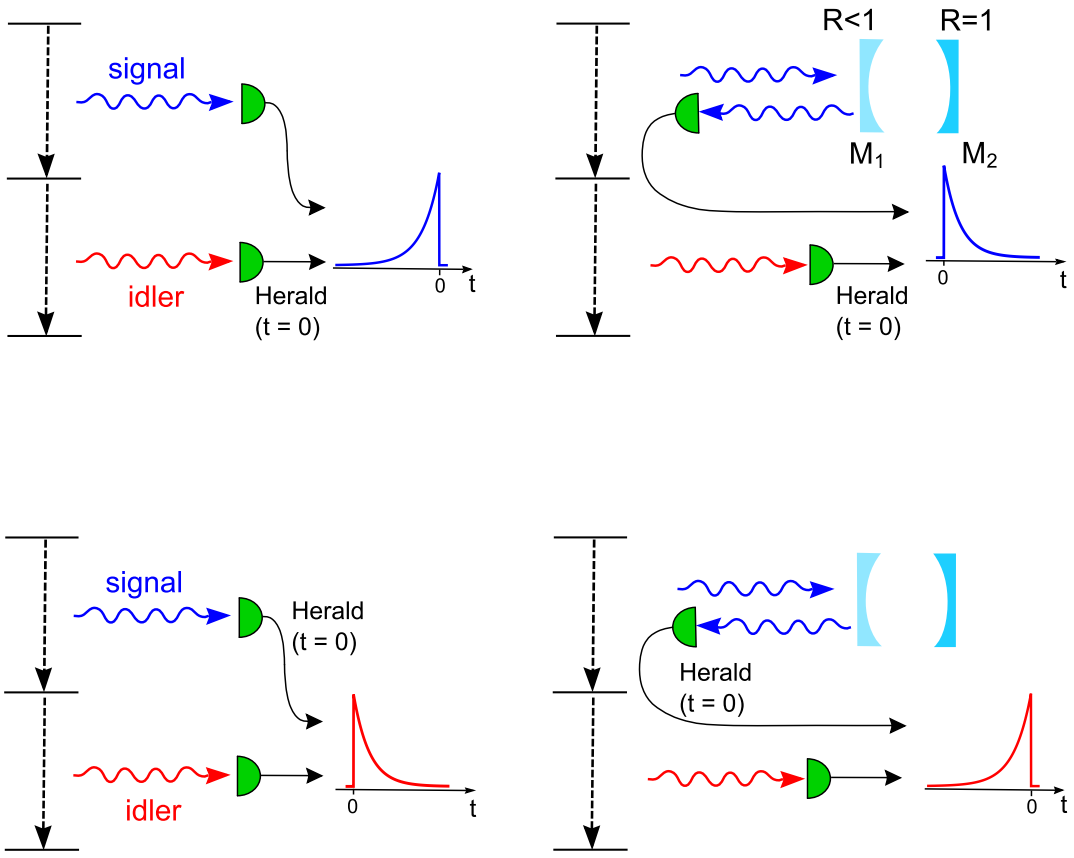

Figure 4.1: Concept of time reversal of the heralded photons using an asymmetric cavity. The figures of the left shows the temporal shape of the heralded photons without the cavity. The experimental observation of this was presented in Chapter 3. The figures on the right shows how an asymmetric cavity in the signal mode is expected to reverse the envelope of these photons.

In our experiment the signal photon has a rising exponential envelope when heralded on the detection of the idler photon. When coupled to the cavity, its temporal envelope changes to an exponential decay. However we are interested in the shape of the heralded idler photons resonant with the ground state of the atom. If the heralded signal photon has an exponentially decaying envelope, symmetry implies that the heralded idler photon has a rising exponential envelope with the same time constant. Thus by using an asymmetric cavity in the signal mode we can invert the temporal shape of the idler photons from exponential decay to a rise.

4.1.2 Theory

The photons emerging from an atomic cascade decay have a well defined time order. The first photon of the cascade (signal) is generated before the photon resonant with the ground state (idler). The resulting state can be described by a two photon wave function [102] of the form

$$\psi(t_s, t_i) = A\, e^{-(t_i - t_s)/2\tau}\, \Theta(t_i - t_s)\,, \tag{4.1}$$

where t_s, t_i are the detection times of the signal and idler photons, and Θ is the Heaviside step function. In this notation, the probability of observing a pair is proportional to $|\psi(t_s, t_i)|^2$. The exponential envelope and the decay time τ is a consequence of the atomic evolution of the cascade decay. If the detection of a signal photon is used as herald, the idler mode has a single photon state with a exponentially decaying temporal envelope starting at $t_i = t_s$. Similarly, if the detection of an idler photon acts as a herald, the signal photon has an exponentially rising temporal envelope.

The effect of the cavity on the signal mode can be described as a frequency-dependent phase factor [119, 120],

$$C(\delta') = \frac{\sqrt{R_1} - \sqrt{R_2}\, e^{i\,\delta'/\Delta\nu_f}}{1 - \sqrt{R_1\, R_2}\, e^{i\,\delta'/\Delta\nu_f}}\,, \tag{4.2}$$

where $R_{1,2}$ are the reflectivities of $M_{1,2}$, $\Delta\nu_f$ is the free spectral range of the cavity,

and δ' the detuning from the cavity resonance. For $R_2 = 1$, the transformation of the incoming mode is lossless, i.e., $|C(\delta')| = 1$. We are only interested in the condition when the photon frequency is tuned near the cavity resonance i.e. $\delta' \ll \Delta\nu_f$. Therefore Eq. (4.2) can be approximated upto the first order in series expansion as

$$C(\delta') \approx \frac{\sqrt{R_1} - \sqrt{R_2}\,(1 + i\,\frac{\delta'}{\Delta\nu_f})}{1 - \sqrt{R_1\,R_2}\,(1 + i\,\frac{\delta'}{\Delta\nu_f})}\,. \tag{4.3}$$

The cavity transforms the two-photon wavefunction in Eq. (4.1) into the two-photon wavefunction $\tilde{\psi}(t_s, t_i)$:

$$\tilde{\psi}(t_s, t_i) = \mathcal{F}_s^{-1}\left[C(\omega_s - \omega_s^0 - \delta) \cdot \mathcal{F}_s\left[\psi(t_s, t_i)\right]\right]\,, \tag{4.4}$$

where $\mathcal{F}_s$ denotes a Fourier transform from t_s to ω_s, and δ is the detuning of the cavity resonance from the signal photon center frequency $\omega_s^0/2\pi$.

If R_1 is chosen such that the ring-down time of the cavity matches the coherence time τ of the photon pair, resulting wavefunction is:

$$\begin{aligned}\tilde{\psi}(t_s, t_i) = \frac{A}{\sqrt{1 + 4\,\delta^2\tau^2}}\,[\quad & 2\,\delta\,\tau\,e^{-(t_i - t_s)/2\,\tau}\,\Theta(t_i - t_s) \\ & + e^{(t_i - t_s)/2\,\tau}\,\Theta(-t_i + t_s)]\end{aligned} \tag{4.5}$$

with an exponentially rising and an exponentially decaying component. Their relative weight can be controlled by the detuning δ; for $\delta = 0$, a time-reversed version of Eq. (4.1) is obtained:

$$\tilde{\psi}(t_s, t_i) = A\,e^{(t_i - t_s)/2\,\tau}\,\Theta(-t_i + t_s). \tag{4.6}$$

Heralding on the detection of a modified signal photon results in an idler photon state with a rising exponential envelope, ending at $t_i = t_s$. The cavity thus effects a reversal of the temporal envelope of the heralded idler photons from an exponential decay to a rise.

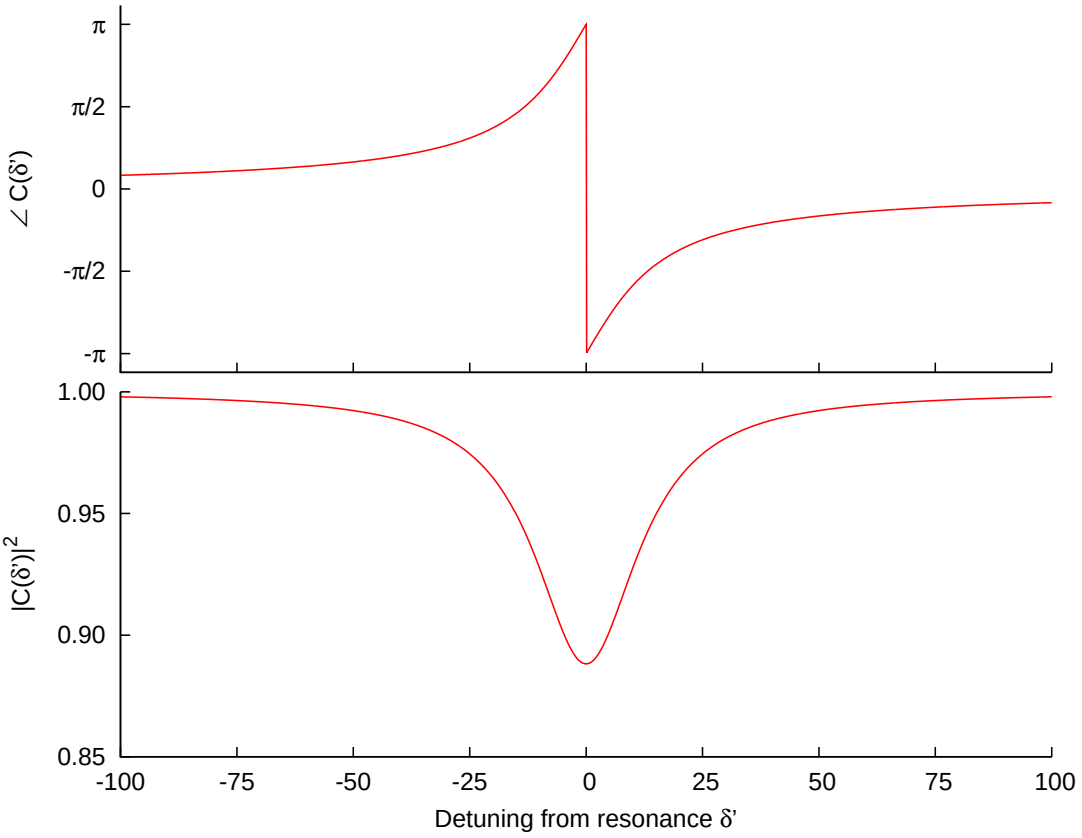

Figure 4.2: Transfer function of the asymmetric cavity. **(Top)** Argument of the cavity transfer function, $\angle C(\delta') = \tan^{-1}\left(\frac{\mathrm{Im}[C(\delta')]}{\mathrm{Re}[C(\delta')]}\right)$. **(Bottom)** Absolute value of the cavity transfer function, $|C(\delta')|$. The loss in the cavity is given by $1 - |C(\delta')|$.

In practice, R_2 is always less than 1, which leads to losses in the cavity. In the experiment we have R_1=0.941, R_2=0.998, and $\Delta\nu_f$=2.7 GHz (see next section). The transfer function between the incident light to the cavity and the reflected light from the cavity for these parameters is shown in Figure 4.2.

4.1.3 Experiment

To experimentally investigate the time reversal technique, we use the setup shown in Figure 4.3. We generate time-ordered photon pairs by four-wave mixing in a cold ensemble of ^{87}Rb atoms in a cascade level scheme. Pump beams at 795 nm and 762 nm

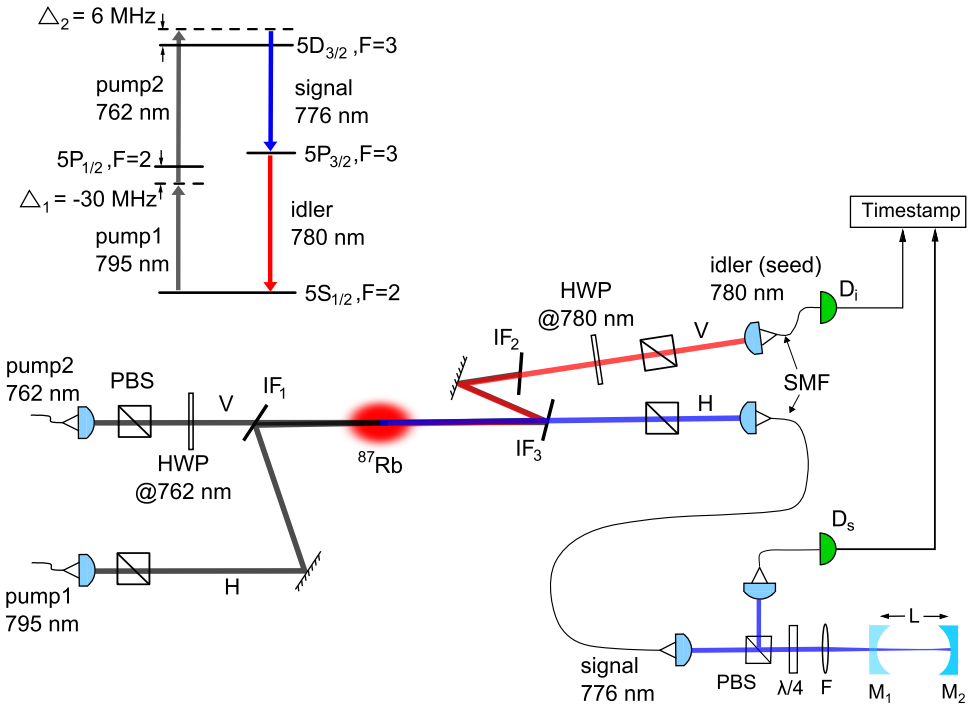

Figure 4.3: Schematic of the time reversal experiment. IF_1, IF_2: interference filters, used to combine pump beams and to separate the photons pairs. SMF: Single mode optical fibers. M_1, M_2: cavity mirrors. The incoming and outgoing mode of the cavity are separated by a polarizing beam splitter (PBS) and a quarter wave plate ($\lambda/4$). D_1, D_2: silicon avalanche photodiodes (APD). The inset shows the cascade level scheme for generation of photon pairs in ^{87}Rb

excite atoms from the $5S_{1/2}, F = 2$ ground level to the $5D_{3/2}, F = 3$ level via a two-photon transition. The 776 nm (signal) and 780 nm (idler) photon pairs emerge from a cascade decay back to the ground level and are coupled to single mode fibers.[1] All four modes are collinear and propagate in the same direction. The coherence time τ of the photon pairs is determined by a time-resolved coincidence measurement between the detection of signal and idler photons to be 5.9±0.2 ns. The optical density of the

[1]Note that for this experiment we swap the wavelengths of the pumps and generated photon pairs described in chapters - 2 and 3. This is done because the single atom experiment in our group requires a single photon resonant with the D2 line (780 nm) for efficient interaction.

atom cloud for this experiment is ≈ 28.

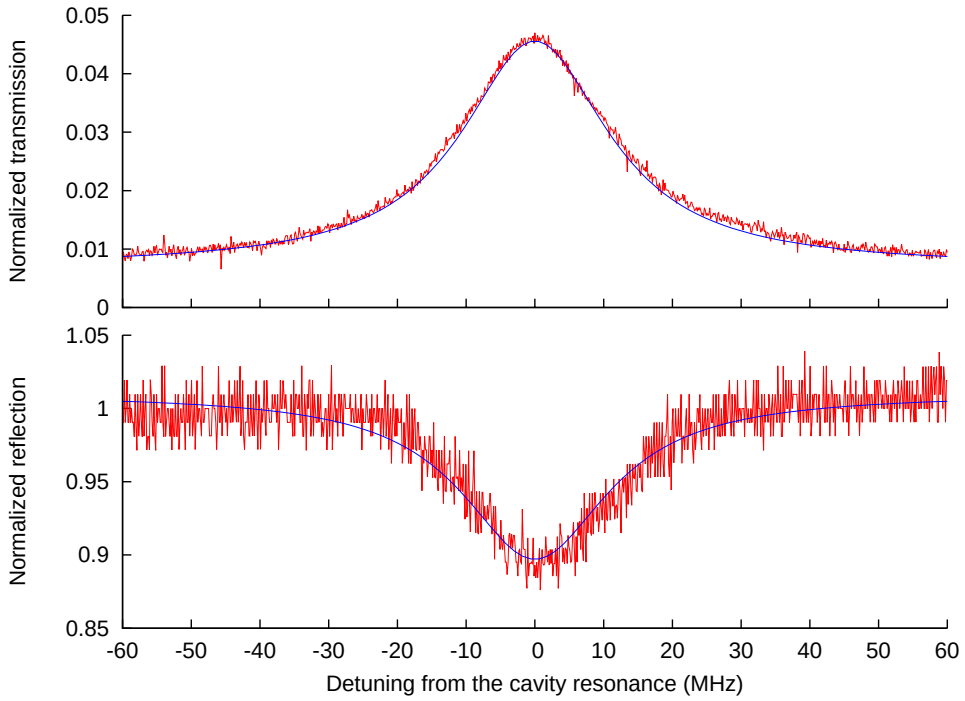

Figure 4.4: Transmission and reflection of the asymmetric cavity measured using 776 nm laser. **(Top)** Transmission through the cavity as a function of the detuning Δ from the cavity resonance. The blue line is the fit of the form $T(\Delta) = b + a\frac{(\gamma/2)^2}{\Delta^2+(\gamma/2)^2}$, where γ=27 MHz, a=0.039, and b=0.007. **(Bottom)** Reflection from the cavity as a function of the detuning Δ from the cavity resonance. The blue line is the fit of the form $T(\Delta) = b' - l\frac{(\gamma/2)^2}{\Delta^2+(\gamma/2)^2}$, where γ=27 MHz, l=0.113, and b'=1.01. The reflectivity of M_2 and the losses in the cavity (R_2) is obtained from the fit parameters to be $R_2 = 0.998 \pm 0.001$.

One of the modes of the photon pairs (signal in Figure 4.3) is coupled to the fundamental transverse mode of an asymmetric cavity, formed by mirrors M_1, M_2 with radii of curvature of 100 mm and 200 mm, respectively. We characterize the cavity using a frequency stabilized laser of wavelength 776 nm. The reflectivity of mirror M_1 is determined by direct measurement with a PIN photodiode to be $R_1 = 0.9410 \pm 0.0008$. Transmission through the mirror M_2 and absorption by the mirrors leads to losses in the cavity. The loss per round trip is determined from the transmission through and the

reflection from the cavity and is included in the reflectivity of M_2, $R_2 = 0.998 \pm 0.001$ (Figure 4.4). The mirrors are mounted on a 55 mm long fused silica spacer, corresponding to a free spectral range $\Delta\nu_f = 2.7\,\mathrm{GHz}$. Therefore, an incident photon of Fourier bandwidth $1/(2\pi\tau) = 27\,\mathrm{MHz}$ interacts effectively with only one longitudinal mode of the cavity, ensuring that Eq. (4.3) is an adequate model. Temperature control of the spacer allows precise tuning and stabilization of the resonance frequency of the cavity. The light reflected off the cavity is separated from the incident mode by using a polarising beam splitter (PBS) and a quarter waveplate ($\lambda/4$).

4.1.4 Results

We infer the temporal shape of the heralded photons from the time distribution of the coincidence rate $G^{(2)}_{si}$ between the APDs D_s and D_i. In Figure 4.5 we show $G^{(2)}_{si}$ for three different cavity-photon detunings. When the cavity resonance is tuned far away from the signal photon frequency ω_s^0, in this case about $\delta/2\pi = 120\,\mathrm{MHz}$, the temporal envelope remains nearly unchanged from the exponential decay obtained without the cavity. Off-resonant coupling of the incident signal photon to the cavity leads to the residual coincidences at times $t_i - t_s < 0$. At $\delta/2\pi = 27\,\mathrm{MHz}$, the time distribution becomes a symmetric exponential, and on resonance, $\delta/2\pi = 0$, we obtain a rising exponential shape. For all three detunings the measurement agrees with the shape expected from Eq. (4.5): the exponential time constants remain unchanged and the new temporal shapes are determined by the phase shift across the cavity resonance via Eq. (4.3).

From the time distribution of the coincidence counts, it is evident that the situation is symmetrical to what we presented in Section 3.3.4: by heralding on the signal photon we now obtain an idler photon with a rising exponential temporal envelope. This result, though predicted by the theory, is particularly exciting: the idler photon is resonant with a ground state transition and its temporal envelope is similar to the time reversal of that obtained by spontaneous decay. The only deviation from the predicted shape occurs for a short time interval after the detection of the herald ($t_i - t_s > 0$). We

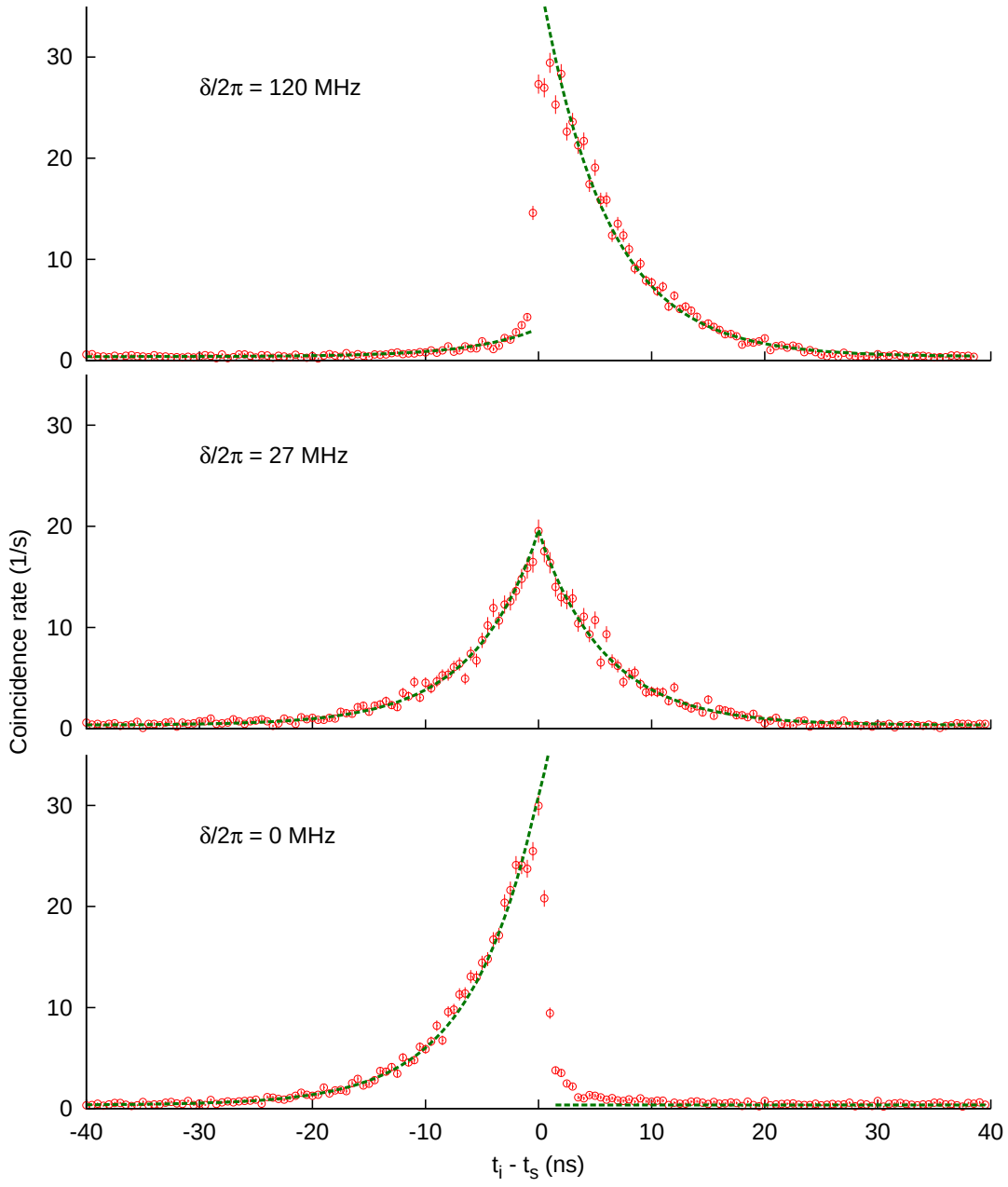

Figure 4.5: Transformation of the heralded idler photons from exponential decay to rise when the cavity is aligned in the signal mode. The y-axis shows the coincidence rate $G^{(2)}_{si}$ between the detectors D_1 and D_2 as a function of the detection time difference. The dashed lines represent $\left|\tilde{\psi}(t_s, t_i)\right|^2$, obtained from the model described by Eq. (4.5) for the indicated cavity detunings δ, with the amplitude A as the only free parameter used to fit the experimental points.

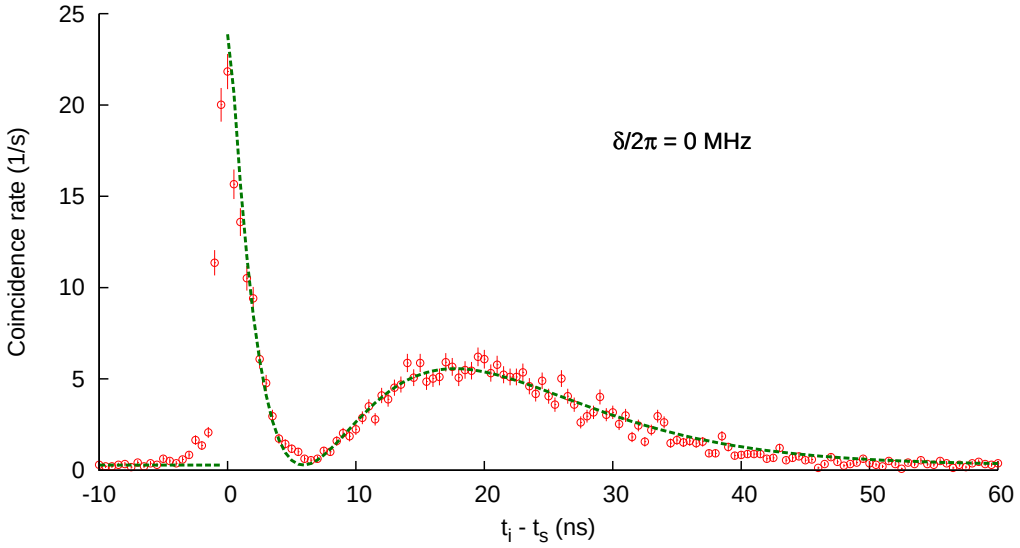

Figure 4.6: Temporal envelope of the idler photon when the cavity is aligned and tuned to resonance with the idler mode. The dashed line represents $\left|\tilde{\psi}(t_s, t_i)\right|^2$ obtained from Eq. (4.4) by swapping i and s. Also in this case, the amplitude is the only free parameters used in the fit.

attribute this deviation to an imperfect matching between the signal and cavity spatial modes.

To confirm the predictive power of our model, we repeated the same experiment swapping the roles of the signal and idler modes i.e., the cavity is aligned in the idler mode. This corresponds to swapping the subscripts s and i in Eqs. (4.4) and (4.5). Figure 4.6 shows the time resolved coincidence rate $G^{(2)}_{si}$ between the signal and modified idler photons with the cavity tuned on resonance with the idler central frequency. In this case the cavity transforms the exponentially rising temporal envelope into a more complex shape. Our model describes accurately this complex shape, as can be seen from the dashed line in Figure 4.6.

4.2 Coupling of the single photons to the cavity

Efficient coupling of temporally shaped coherent light pulses to an optical cavity was studied in [21]. In this section we present a similar experiment with single photons using the same experimental setup used for reversing the temporal envelope. We determine the population of the cavity mode as a function of time, and observe its dependence on the temporal envelope of the incident photon.

4.2.1 Estimation of the photon number in the cavity

The photon number in the cavity at any given time from the heralding event can be estimated from the time distributions of the rate of the photons incident to the cavity (G_{in}) and the rate of the photons reflected back from the cavity (G_{ref}). The G_{in} is obtained by tuning the cavity resonance to ≈200 MHz from the central frequency of the incident photons. The loss per round trip due to the leakage through the mirror M_2 and the absorption in the mirrors is $\eta = 1 - R_2 = 0.002 \pm 0.001$. The mean photon number in the cavity $\langle n(t) \rangle$ is given by,

$$n(t) = \int_{-\infty}^{t} \Big(\frac{G_{in}(t')}{P} - \frac{G_{ref}(t')}{P} - \frac{n(t')\,\eta}{t_{rt}} \Big)\, dt' \,, \tag{4.7}$$

where $P = \int_{100\,\mathrm{ns}}^{-100\,\mathrm{ns}} G_{in}(t)\, dt$ is the total rate of the incident photons, and $t_{rt} = 2L/c = 0.37\,\mathrm{ns}$ is the round trip time of the cavity. Eq. (4.7) can be rewritten as a differential equation,

$$\frac{d\,n(t)}{dt} = \frac{G_{in}(t)}{P} - \frac{G_{ref}(t)}{P} - \frac{n(t)\eta}{t_{rt}} \tag{4.8}$$

The solution of this differential equation is given by,

$$n(t) = \frac{e^{-\eta\, t/t_{rt}}}{P} \int_{-\infty}^{t'} \Big(\frac{G_{in}(t')}{P} - \frac{G_{ref}(t')}{P} \Big)\, e^{\eta\, t'/t_{rt}}\, dt' \tag{4.9}$$

We use Eq. (4.9) to determine the mean photon number in the cavity with single photons of different temporal shapes.

4.2.2 Results

When the cavity is aligned in the idler mode, we have a heralded single photon with decaying exponential envelope interacting with the cavity. The mean photon number in the cavity ($\langle n(t)\rangle$) reaches a maximum of 0.44 ± 0.01 as shown in Figure 4.7. On the other hand, when the cavity is aligned in the signal mode we have a heralded single photon with a rising exponential envelope interacting with the cavity. In this case, $\langle n(t)\rangle$ reaches a maximum of 0.76 ± 0.01. As expected, the photon with the rising exponential waveform interacts more efficiently with the cavity.

We also measured the population of the cavity with an exponentially rising single photon of coherence time $\tau = 17 \pm 1\,\mathrm{ns}$, much longer than the ringdown time of the cavity. This coherence time is obtained by lowering the optical density of the atom cloud to ≈ 7. The result is shown in Figure 4.8. It can be seen that the maximum value of $\langle n(t)\rangle$ is 0.51 ± 0.02., lower than the case when the decay times match.

An asymmetric optical cavity is analogous to a single atom in many aspects [121]. Following this analogy, we expect the results presented in this section to be extended to the probability of absorption of a single photon by a single atom. In the case of interaction with a single atom, in addition to the "time reversed" envelope it will also be necessary to match the bandwidth of the transition for an efficient absorption. We have already demonstrated how it is possible to control the bandwidth of the photon generated by the cascade process by adjusting the optical density of the atomic medium in Section 3.2.

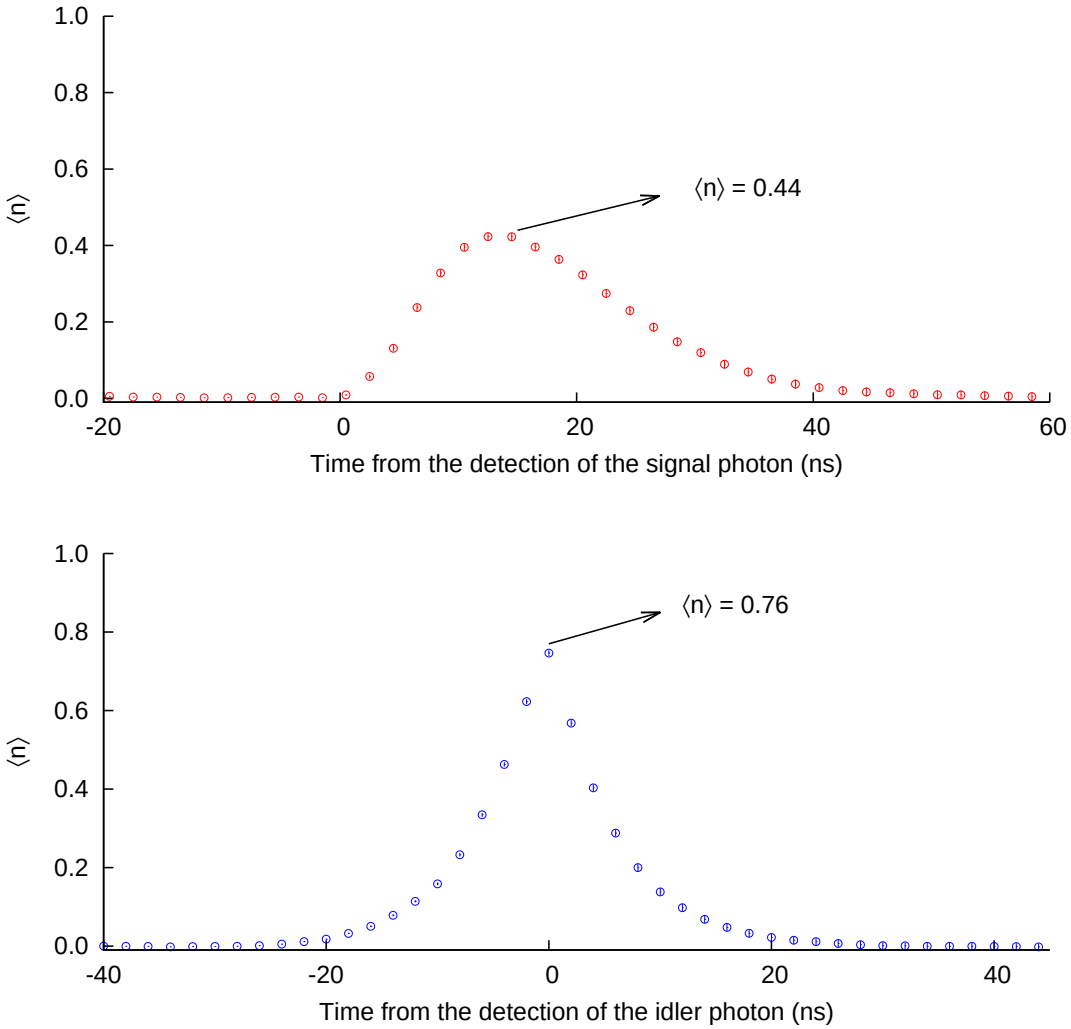

Figure 4.7: Mean photon number in the cavity estimated using Eq. (4.9). **(Bottom)** The detection of an idler photon is used as herald and the cavity is in the signal mode. In this case we observe the interaction of an exponentially rising waveform with the cavity. **(Top)** The roles of signal and idler are swapped and the cavity interacts with an exponentially decaying incident photon.

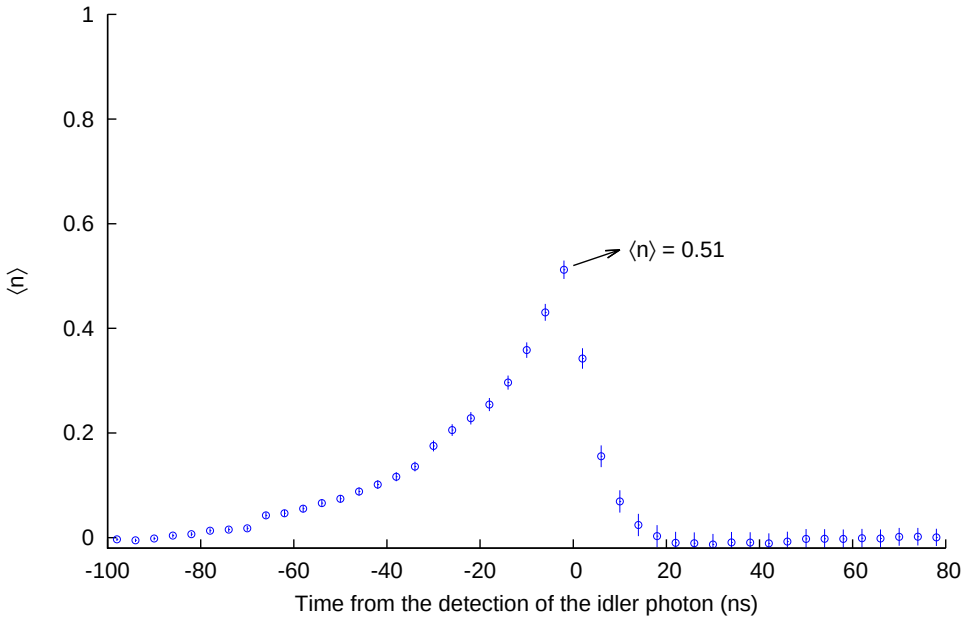

Figure 4.8: Mean photon number in the cavity with an exponentially rising single photon of coherence time 17 ns. The peak value of $\langle n \rangle$ is 0.51.

4.3 Conclusion

In this chapter, we have demonstrated a method to transform a heralded single photon with a decaying exponential temporal envelope to a rising exponential envelope using a cavity. Using this method, we obtain single photons that resemble the time-reversed versions of photons from spontaneous decay process resonant to the D2 line of ^{87}Rb atoms. Single photon states of this envelope and suitable bandwidth would be useful for transferring quantum information from photons to atoms. The time reversal technique presented here can also be used with photon pairs from other sources with time-ordered emission, as found e.g. in molecules and quantum dots.

Chapter 5

Conclusion and outlook

In this thesis we have demonstrated a source of narrow bandwidth heralded single photons resonant with the ground state of ^{87}Rb atoms. The bandwidth of the photons is tunable from 10 MHz to 30 MHz, and a maximum photon detection rate of 18000 s^{-1}. We have also presented a potentially loss-less technique to reverse the temporal envelope of the photons to resemble the time reversal of spontaneous decay process.

5.1 Outlook

Sonderman et al. [122] has theorized that a single photon light field can be absorbed completely by a single atom provided that it was generated by an inversion of all the degrees of freedom of the atomic spontaneous emission process. One of the challenges to experimentally verify this has been to obtain single photons with a time reversed envelope. There has been a few recent experiments with temporally shaped coherent pulse with a single atom [24] or a cavity [21]. Our photons can be used to perform similar experiment with single atoms in free space or in a weakly coupled cavity. Such an experiment would serve to verify the reversibility of the spontaneous emission process.

Another interesting experiment that one could perform with our photons is to study how remote manipulation of its temporal envelope affects the absorption by an atom. Consider an experiment where our photons are sent to a single atom trapped in free

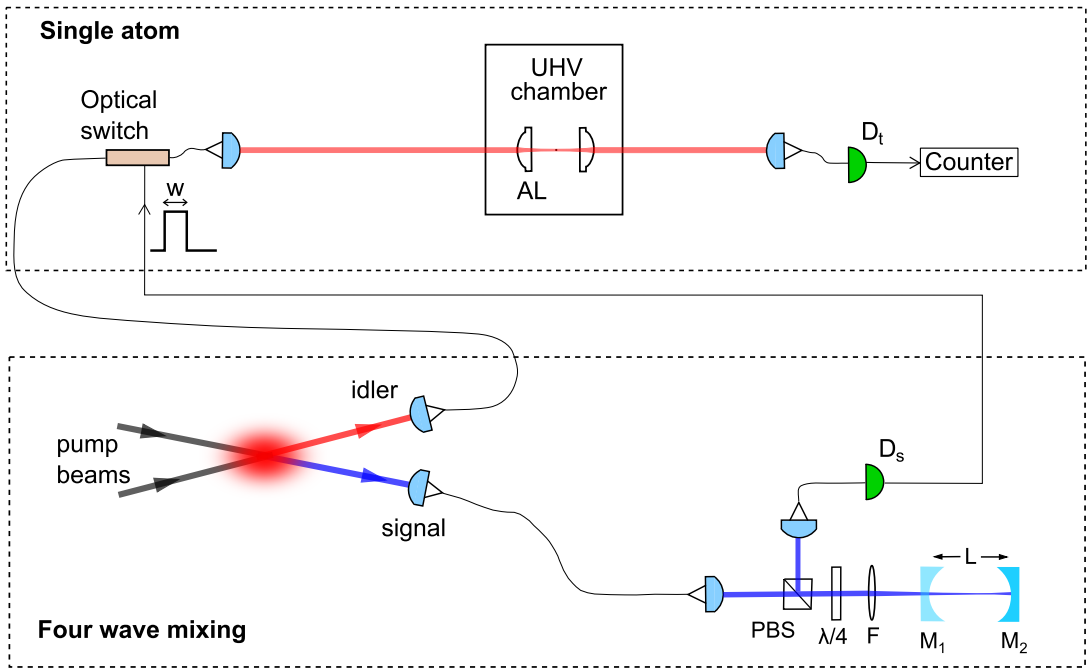

Figure 5.1: Schematic of a proposed experiment to measure the mean absorption of a single photon from FWM by a single atom trapped between two aspheric lenses (AL). The detection signal from D_s is used to open a time window of width w using an optical switch to let the single photon reach the single atom experiment. The transmission of the photon is measured using an APD D_T.

space by a tightly focused optical dipole trap [58, 59] (see Figure 5.1). The interacting photon (idler) is turned on/off by using an optical switch controlled by the detection of a heralding (signal) photon. The switch is opened for a specific time (w) from the detection of time of the signal photon, thereby directing the idler photon to the atom for absorption. How would the mean absorption/scattering change as the resonance frequency of the cavity in the signal mode is varied? And how does the width of the switching time window (w) affect the mean absorption? Answering these questions in an experiment would be helpful to better understand the temporal shaping of single photons by heralding technique, and also the interaction of atoms and photons at a fundamental level.

From quantum information perspective, transfer of entanglement between photons

and atoms is an important step towards building quantum networks. Polarization entanglement of our photon pairs combined with the absorption by an atom can be used to perform entanglement swapping experiments similar to [123, 124].

5.2 Progress towards absorption by a single atom

We are currently working towards interfacing our photons with a single atom in an optical dipole trap in free space. As a first step, we performed an experiment to show that the single photon from our source is indistinguishable from a fluorescence photon from a single atom. A detailed description of this experiment can be found in [76, 125]. A simplified schematic of the Hong-Ou-Mandel (HOM) interferometer used carry out the experiment is shown in Figure 5.2. Single photons from our experiment and the single atom are sent to the input ports of a 50/50 Beam Splitter (BS). The interference of the photons result in bunching at the output ports of the BS. We measure a HOM dip in the coincidences between the detectors D_1 and D_2 with a visibility of $75\pm4\,\%$, indicating that the two photons are indeed largely indistinguishable. Therefore, the time reversed version of the heralded photons from our source obtained by the technique discussed in Chapter 4 should in principle also be indistinguishable from the time reversal of the single atom spontaneous decay.

However the cavity described in Chapter 4 requires polarization projection in order to reverse the envelope. This destroys the polarization entanglement of the photon pairs. In addition to this, the linewidth of the cavity is about 4 times larger than the linewidth of the ^{87}Rb D2 line. A traveling wave bow tie cavity would solves both these issues. The incoupling and the outcoupling modes of such a cavity are spatially separable. Therefore, if the reflectivity of the mirrors are polarization independent, we can reverse the envelope without any polarization projection. We are presently making a bow tie cavity with a linewidth of $\approx$10 MHz, matching the minimum achievable bandwidth of the photons with a reasonable rate ($\approx 50\,\mathrm{s}^{-1}$).

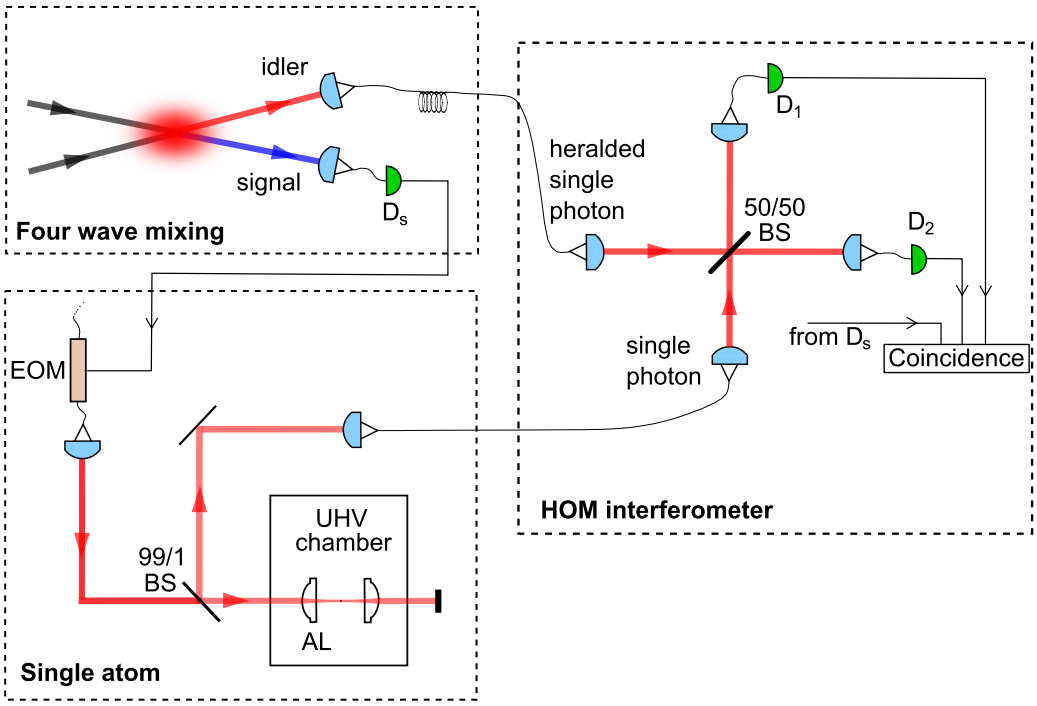

Figure 5.2: A simplified schematic of the Hong-Ou-Mandel (HOM) interference between heralded single photons from four wave mixing and fluorescence photon from a single atom. The detection of a signal photon by an APD D_s is sent to the single atom experiment where it is used as a time reference to prepare a π pulse for exciting the atom. The fluorescence photon from the excited atom reflected from the 99/1 BS is coupled into single mode fiber and sent to one of the input ports of the 50/50 BS used in HOM interferometer. The idler photon from FWM is sent to the other input port of the 50/50 BS. The fiber delay is adjusted such that the two photons reaches the 50/50 BS at the same time. The bunching in photon statistics due to HOM interference is observed by measuring the coincidences between APDs D_1, D_2 and D_s.

Appendix A

Absorption imaging

In this chapter we describe the measurement of the number of atoms trapped by the Magneto-Optical Trap (MOT) using absorption imaging. Absorption imaging is a standard method to determine the number and the density of the atoms obtained by laser cooling techniques [126].

A.1 Experiment

The basic idea of absorption imaging is illustrated in Figure A.1(a). A probe laser of diameter much larger than the size of the cloud and near resonant to the $5S_{1/2}, F = 2 \rightarrow 5P_{3/2}, F = 3$ transition is aligned to overlap with the entire cloud. The probe beam was collimated from the fiber using a 25 mm focal length lens, resulting in a beam diameter of ≈ 6 mm. The power of the probe beam was chosen to be $10\,\mu$W such that the peak intensity is more than 40 times lower than the saturation intensity of the above mentioned transition. The transverse profile of the beam is elliptical instead of Gaussian due to the aberrations caused by the collimating lens. However this is not a problem since the measurements rely only on the intensity fraction with and without the cloud. A two lens telescope with a magnification factor of ≈ 0.23 is used to image the cloud onto a CCD chip. We use a linear CCD camera (Sony XC-56) with a resolution of 659×494 pixels. Each pixel has a physical dimension of $7.5\,\mu\text{m} \times 7.5\,\mu\text{m}$.

A. ABSORPTION IMAGING

The timing sequence of the experiment shown in Figure A.1(b) is different from the cycle used for the photon pair generation. This is mainly because of the slow switching time of the camera shutter. Even though the applied TTL switching pulse to the camera is only 70 μs wide, the camera shutter takes a few ms to "close" completely. During this time the cooling light cannot be turned on as it would affect the measurement.

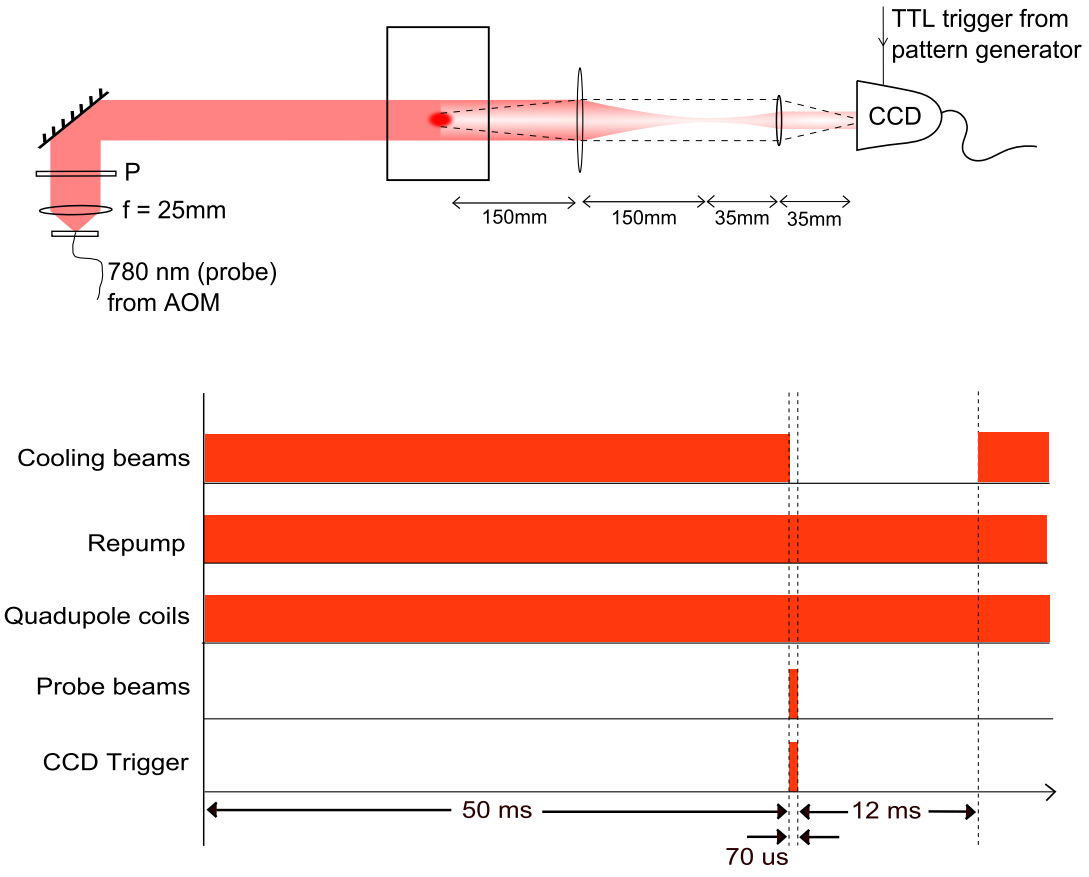

Figure A.1: **(a)** Experimental setup used for absorption imaging. The shadow cast by the cloud of ^{87}Rb atoms on the transverse profile of a near resonant probe laser is imaged using a CCD chip. **(b)** The timing sequence used for absorption imaging.

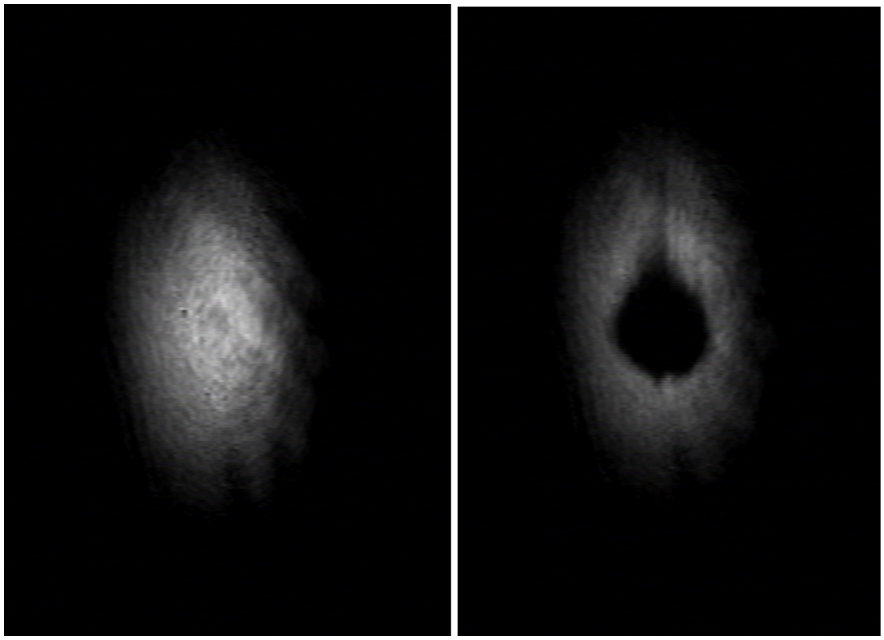

Figure A.2: Shadow cast by the atom cloud on the probe beam. CCD image of the resonant probe beam without (left) and with (right) the atom cloud

A.2 Results

Due to the absorption of the probe light by the cloud during the acquisition time of the camera its image appears as a shadow in the probe beam (see Figure A.2). Each pixel of the camera records the transmission of the probe along different columns along the cloud. We record these transmission images by tuning the frequency of the probe beam across the atomic resonance using an AOM. Three images are captured for every detuning value of the probe beam: (1) with both the probe beam and the cloud to see the absorption (I); (2) with the probe beam but *without* the cloud to obtain I_0; (3) with the probe beam switched off to measure the background (bg). The background image is subtratracted from the other two images for determining the optical density (OD). We determine the OD corresponding to each pixel using a fit function,

$$I(\Delta) - bg = (I_0 - bg)e^{-\frac{OD\,\Gamma^2}{4\Delta^2+\Gamma^2}}\,, \tag{A.1}$$

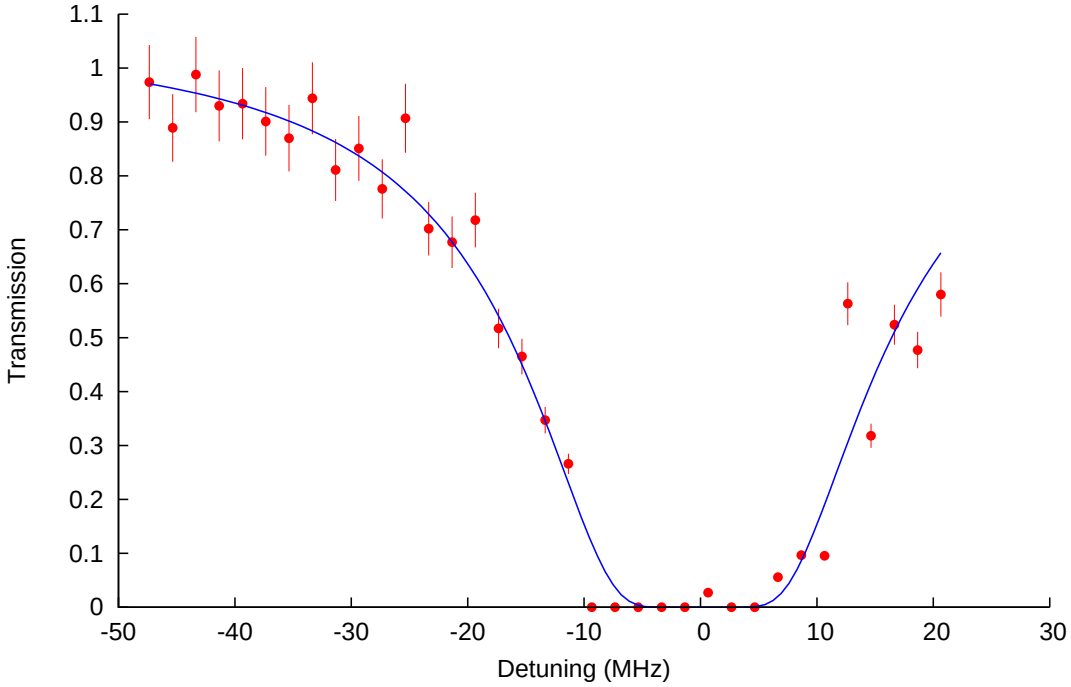

Figure A.3: Transmission corresponding to one of the pixels near the center of the cloud as a function of the detuning from the resonance. The OD obtained from the fit is 25.0±2.2.

where Δ is the detuning of the probe beam from resonance, and Γ=6.06 MHz is the linewidth of the $5S_{1/2}, F = 2 \rightarrow 5P_{3/2}, F = 3$ transition. This fit function is also used when measuring the OD with a photodetector described in Section 2.2.3.

A plot of the probe transmission as a function of detuning for one of the pixels corresponding to a column near the center of the cloud is shown in Figure A.3. The optical densitity ranges from 27.5 at the center of the MOT to 0 outside of the MOT. The distribution of the OD measured for each pixel of the camera is shown as a 3D plot in Figure A.4. It can be seen that the distribution is not Gaussian but rather uniform near the center where the density is high. This is possibly due to the same effects described in [127]

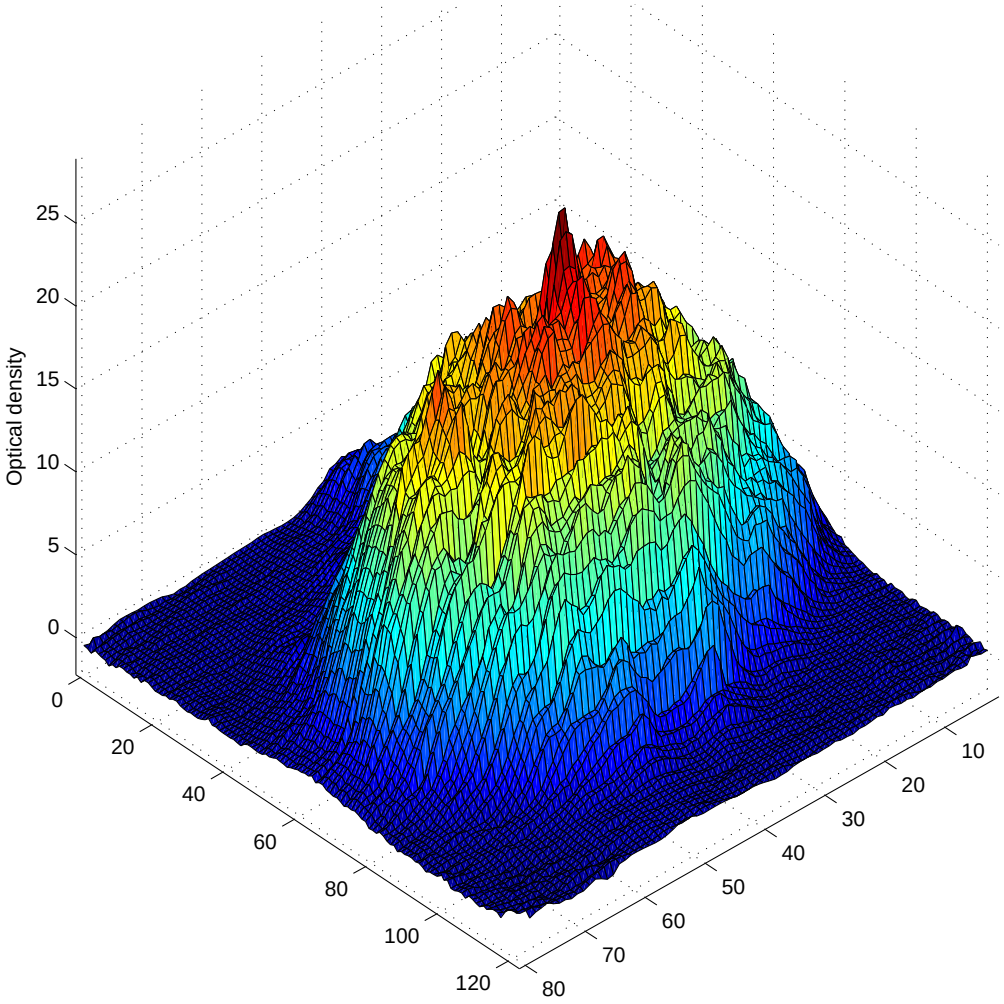

Figure A.4: The optical density as a function of the camera pixel number. Each point is obtained from the transmitted intensity (see Figure A.3) of the probe through a thin column of atoms along the probe propagation direction.

A.2.1 The number of atoms

The average atom density of each column can be obtained from the measured optical density using Beer's law: The transmittance of light traveling through a dispersive medium is given by,

$$\frac{I}{I_0} = e^{-\sigma l n_v}\,, \tag{A.2}$$

where σ is the scattering cross-section, l is the length of the interaction region, and n_v is the average number of the atoms per unit volume in the interaction region. The term ln_v is known as the column density (n_c) and is related to the OD as,

$$ln\Big(\frac{I(0)}{I_0}\Big) \;=\; -OD \;=\; -\sigma n_c\,. \tag{A.3}$$

The average number of atoms in a column corresponding to each pixel of the camera is given by $N_p = n_c A$ where A is the area of the pixel. The total number of atoms in the cloud is obtained by summing N_p over all the pixels of the camera.

$$N = \sum_{\text{all pixels}} N_p \;=\; \sum_{\text{all pixels}} n_c A \;=\; \frac{A}{\sigma_0} \sum_{\text{all pixels}} OD\,. \tag{A.4}$$

We estimate the total number of atoms for the OD distribution shown in Figure A.4 to be $(1.39 \pm 0.21) \times 10^8$.

Appendix B

Four-wave mixing with seed

The atomic ensembles in the presence of the two pump lasers (780 nm and 776 nm) and the seed laser (795 nm) acts as a parametric amplifier. In this process a coherent fourth field (762 nm) is generated in the phase matching direction. We use the seed and the generated field to define the signal and the idler mode for the photon pair generation. In this appendix we study the efficiency of the four-wave mixing process by measuring the power of the generated signal while varying the polarizations of the participating fields.

The experimental setup (see figure B.1) and the timing sequence is the same as that described in alignment procedure (Section 2.3.3). We use a Thorlabs photodetector (PDA36A) to measure the power of the generated signal field. The Figure B.1 shows the oscilloscope trace of the photodiode voltage. During the parametric conversion interval of 1 ms, the generation of the coherent signal field appears as a spike in the photodiode voltage. The background is due to the residual pump light leaking through the interference filters and falling on the photodiode. The Quarter Wave Plates (QWP) and the Half Wave Plates (HWP) in each of the modes is used to set or measure the polarization.

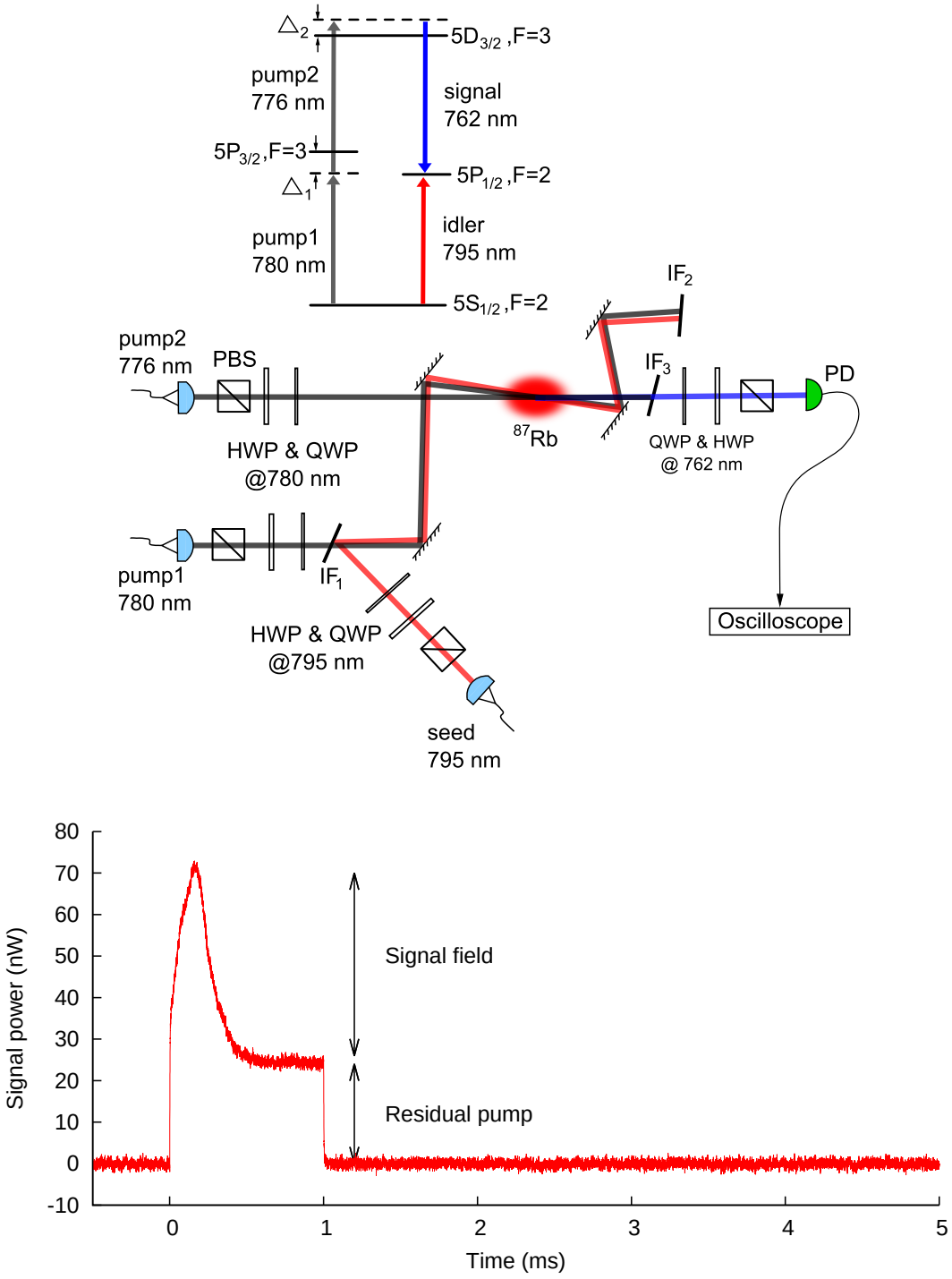

Figure B.1: (Top) Level scheme and setup for FWM with seed. The signal power is measured with a photodiode PD. **(Bottom)** Signal field power measured with an oscilloscope. The background is from the residual 776 nm pump light.

Polarizations				signal
780 nm pump	**776 nm pump**	**795 nm seed**	**762 nm signal**	**power (nW)**
H	H	H	H	30.2
H	H	V	V	7.8
V	H	H	V	80
V	H	V	H	7.8
H	V	V	H	83
V	V	V	V	30
L	L	L	L	39
L	L	R	R	0
R	L	L	R	39.4
L	R	L	R	15.6

Table B.1: The generated signal power and polarization for different polarizations of the pumps and the seed.

To measure the polarization dependence of the signal power, we set different polarization for the pumps and the seed beam. For each setting we determine the polarization and the power of the generated signal. The result of the measurement is shown in Table B.1. The maximum signal power is generated for orthogonal linear polarization of the pump beams. Therefore, we use these polarization settings to obtain high parametric conversion efficiency during photon pair generation.

Appendix C

APD timing jitter

Many measurements presented in this thesis rely on the APDs being able to resolve the temporal envelope of the photons. This requires the jitter time of the APDs to be much smaller than the coherence time of the photons. In this chapter we present a mesurement of the jitter time of an APD used in our experiment.

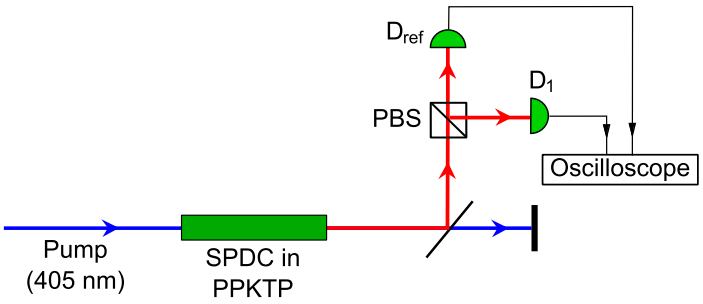

Figure C.1: Experimental setup used to measure APD jitter. The 405 nm photons from the pump laser is converted into photon pairs of wavelength 808 nm by SPDC in a PPKTP crystal. One photon of the pair is detected by a reference APD from MPD, and the other is detected by an APD used in our experiments. The time difference distribution between the detection events is measured using an oscilloscope.

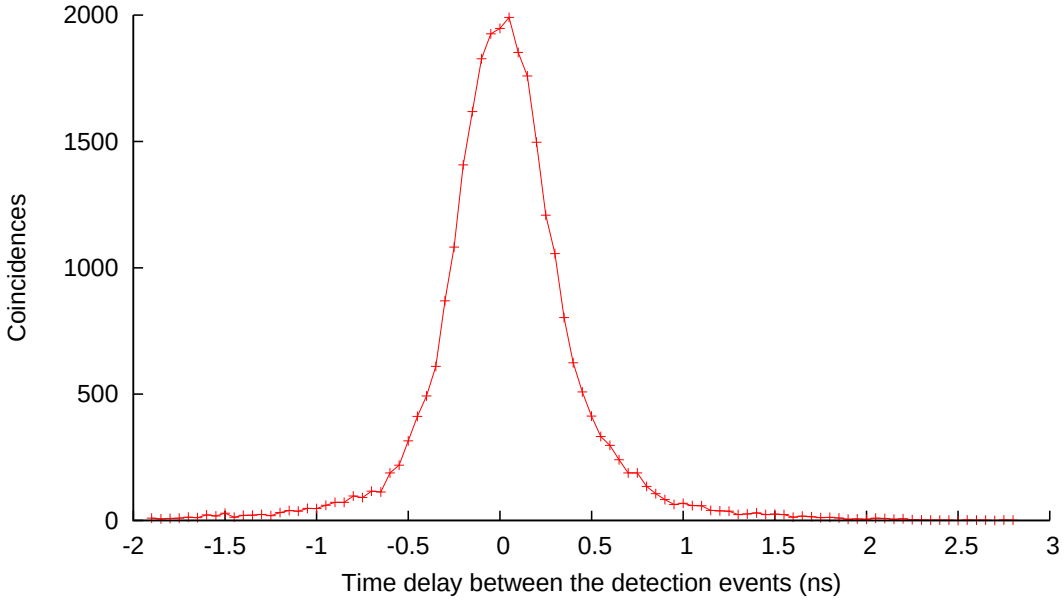

Figure C.2: Result of APD timing jitter measurement. Coincidence between the detection events on D_{ref} and D_1 as a function of the detection time difference. The FWHM of the distribution is 0.58 ± 0.05 ns.

We use an SPDC photon pair source [71] and a commercial APD module from Micro Photon Devices (MPD) with specified jitter time of < 50 ps to perform this measurement. The setup is shown in Figure C.1. The photon pairs from the SPDC source have a FWHM bandwidth of > 100 GHz which corresponds to an arrival time distribution width of < 10 ps, smaller than the jitter of the APDs. The details of the SPDC source can be found in [71]. One photons of the pair is detected by this APD and the other is sent to the APD used in our experiment.

The result of the coincidence measurement is shown in Figure C.2. The width of the time delay distribution obtained from the $G^{(2)}$ between these two detection events gives the combined jitter time of the two APDs. Since the jitter time of the MPD detector is much smaller than our APDs, the measured width is essentially the jitter of our APD.

Appendix D

Superradiance in four-wave mixing

Superradiance is a collective emission phenomenon of an ensemble of excited atoms coupled to a common radiation mode. This phenomenon was first described by Dicke in [73]. There is a wide variety of physical systems where superradiance has been observed [128, 129, 130]. For superradiant emission to happen, the excitation dipoles belonging to different atoms in the ensemble should exhibit correlation in phase along a collective radiation mode. Such a phase correlation between different atoms can be achieved by the proximity of the atoms with separation lengths much smaller than the wavelength of the emitted light [131], coupling of the atoms to a vacuum mode of a resonant cavity [132], or phase-matching in a parametric scattering process [102, 128].

Here we give a brief overview of the superradiance in a four-wave mixing process. Superradiance in four-wave mixing (FWM) via a Λ level scheme has been studied extensively in the context of quantum memories [101, 133]. Since the concept can be easily extended to the cascade level scheme used in our experiment, we first discuss a comparision between the two schemes. We then present the experimental results that shows superradiant emission.

In a FWM experiment via a Λ scheme (see Figure D.1(a)), the first scattering

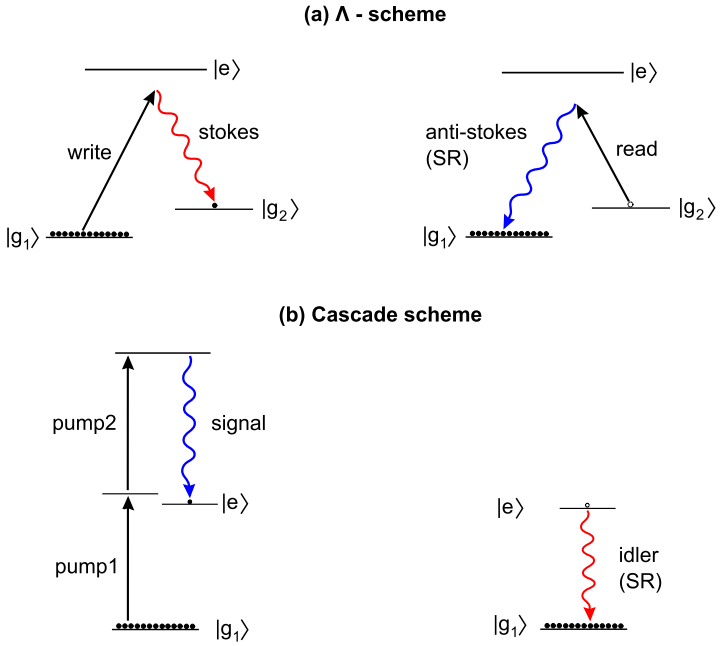

Figure D.1: Superradiance in four-wave mixing. **(a)** Λ scheme: The detection of a stokes photon scattered a write pulse generates a Dicke state of the form described by Eq. (D.1). The superradiance is observed in the emission of the anti-stokes photon during the retrival process. **(b)**Cascade scheme: The detection od a signal photon generated by a two-photon scattering of the pumps prepares a Dicke state of the form Eq. (D.2). Superradiance is observed in the spontaneous emission along the idler mode. In both cases phase matching plays a critical role in achieving the phase coherence between the atoms in the ensemble.

process by an application of a write pulse generates a Dicke state of all N atoms interacting with the pulse.

$$\frac{1}{\sqrt{N}}\sum_{n=1}^{N} e^{i\,\vec{\Delta k}.\vec{r_n}}|g_1\rangle_1|g_1\rangle_2\ldots|g_2\rangle_n\ldots|g_1\rangle_N \tag{D.1}$$

where $\vec{\Delta k}$ is the phase mismatch between the pump and the scattered photon, and $\vec{r_n}$ are the positions of the atoms in the ensemble. Since $|g_1\rangle$ and $|g_2\rangle$ are both ground states there is no spontaneous emission between them. This Dicke state is leads to superradiant emission of a single photon during the retrieval process using a read pulse.

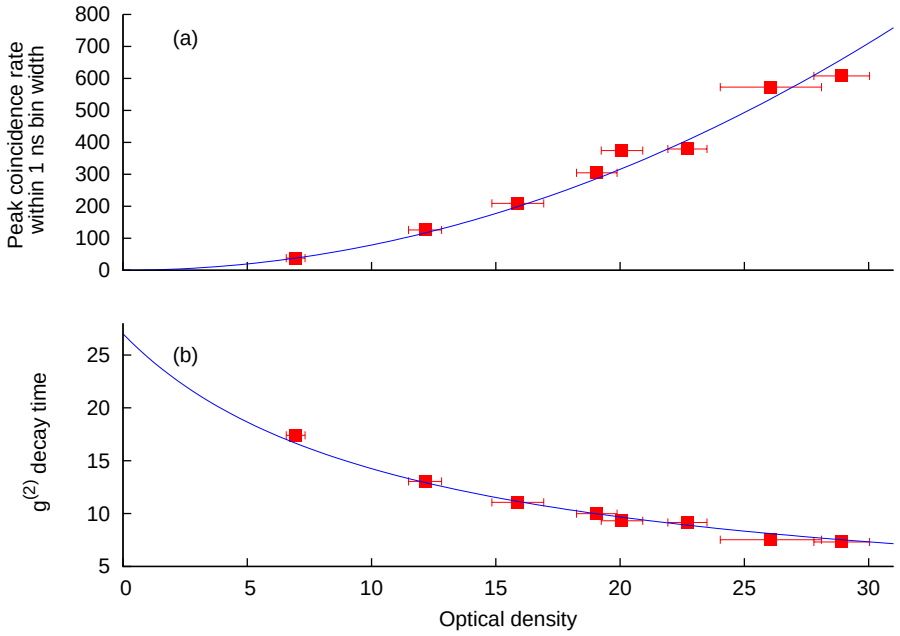

Figure D.2: **(a)** Peak pair rate vs optical density. The line is a fit of the form $r_p = \alpha\,(OD)^2$, where α=0.79. **(b)** Idler decay time vs OD. The line is a fit of the form $\tau/(1+\beta\,OD)$ where $\beta = 0.089$ relates OD to μN in Eq. (D.3).

The superradiance in our experiment is very similar except that the detection of a signal photon prepares a Dicke state of the atomic ensemble with a single excitation to the state $|e\rangle$ (see Figure D.1(b)),

$$\frac{1}{\sqrt{N}}\sum_{n=1}^{N} e^{i\,\vec{k_I}.\vec{r_n}}|g_1\rangle_1|g_1\rangle_2\ldots|e\rangle_n\ldots|g_1\rangle_N \tag{D.2}$$

where $\vec{k_I} = \vec{k_{p2}} + \vec{k_{p1}} - \vec{k_s}$ is given by phase-matching condition. In this case there is spontaneous emission from $|e\rangle$ to $|g_1\rangle$ which is enhanced by superradiance along the idler mode ($\vec{k_I}$).

Since there is a well defined initial condition for the preparation of the Dicke state and the spontaneous emission from $|e\rangle \rightarrow |g1\rangle$ is allowed, we can observe the two characteristic features of superradiance in our experiment:

- The peak intensity (pair rate) increases quadratically with N.

- The decay time τ' is shorter compared to the single atom spontaneous emission time τ,

$$\tau' = \frac{\tau}{1+\mu N}\,, \tag{D.3}$$

  where μ is a geometry factor for the atomic ensemble.

We experimentally verify these two characteristic features of superradiance. We use the optical density of the cloud (OD) as a measure of the number of atoms as $N \propto OD$. In order to vary N without affecting the geometry factor μ, we change the repump laser power.

Figure D.2(a) shows the peak coincidence rate within 1 ns of the detection of the signal photon as a function of optical density (OD) of the cloud. As expected, the rate increases quadratically with the OD.

The $g^{(2)}_{si}(t)$ between detection of signal and idler photons gives the probability of getting a idler photon as a function of time delay from the detection of signal photon. Therefore the exponential time constant of $g^{(2)}(t)$ gives the superradiant decay time of the idler photons. We measure this decay time with different optical densities of the cloud as shown in Figure D.2(b). It can be seen that the variation of the measured decay time agrees with Eq. (D.3).

Appendix E

Laser spectroscopy signals with ^{87}Rb

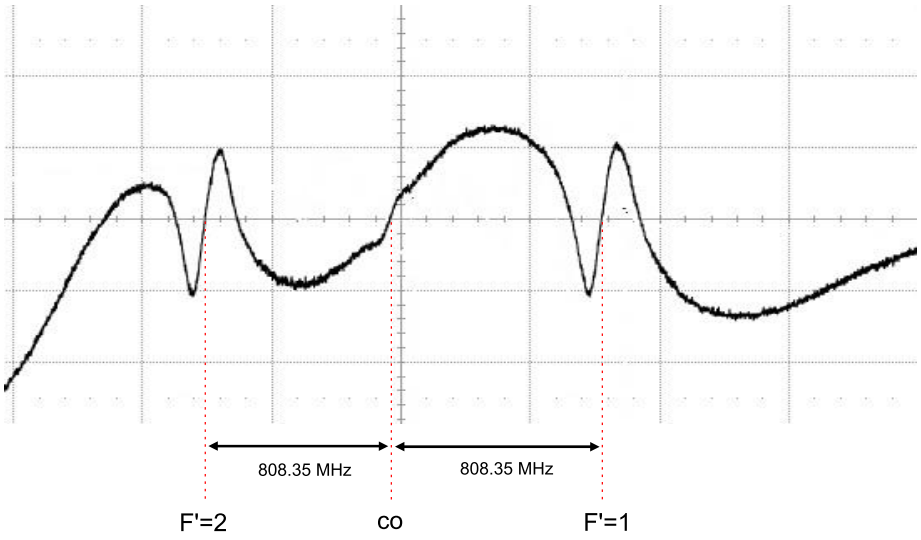

Figure E.1: Spectroscopy error signal of the 795 nm laser corresponding to ^{87}Rb D1 line. The hyperfine lines (F') and the cross-over lines (CO) from $5S_{1/2}, F = 2$ level. The separation frequency (in MHz) between the adjacent lines is indicated.

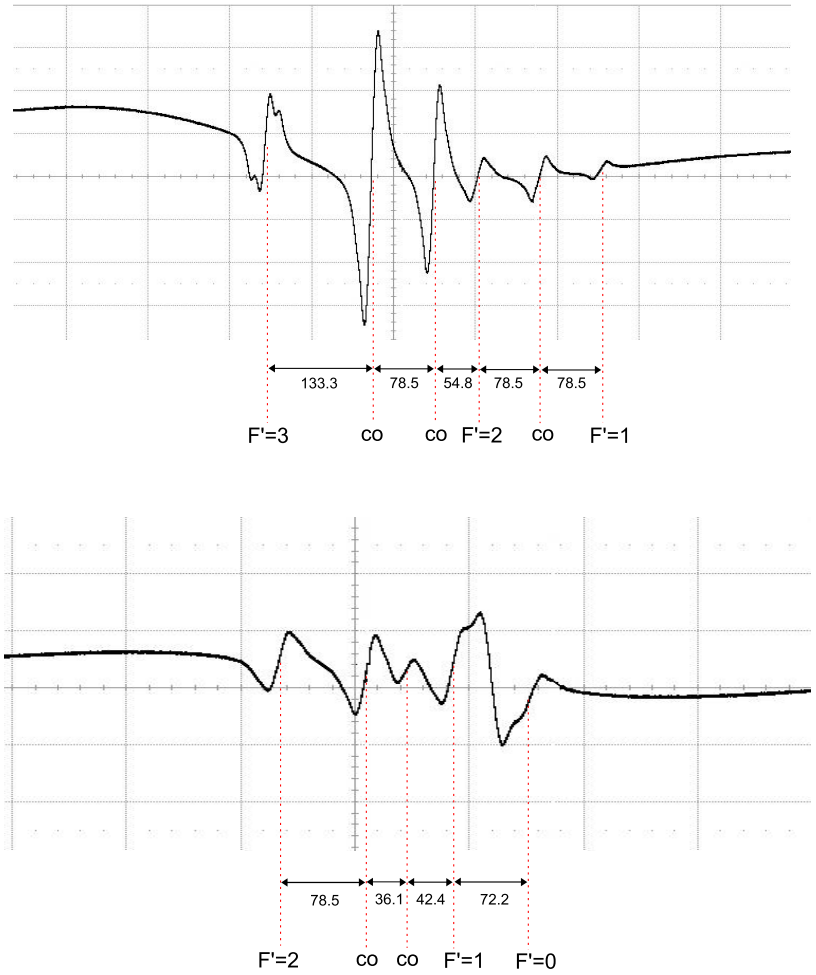

Figure E.2: Spectroscopy error signal of the 780 nm laser corresponding to ^{87}Rb D2 line. The hyperfine lines (F') and the cross-over lines (CO) from $5S_{1/2}, F = 2$ level (Top) and $5S_{1/2}, F = 1$ level (bottom). The separation frequency (in MHz) between the adjacent lines is indicated.

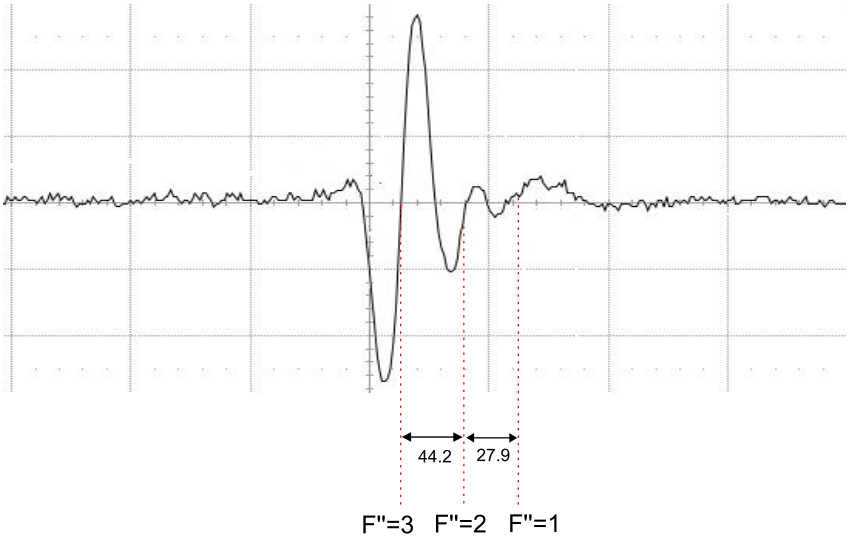

Figure E.3: Spectroscopy error signal of the 762 nm laser. A 795 nm laser resonant to $5S_{1/2}$,F=2 $\rightarrow 5P_{1/2}$,F'=2 is used as a pump. The lines seen in the figure corresponds to the allowed transitions from $5P_{1/2}$,F'=2 level to different hyperfine levels of $5D_{3/2}$.

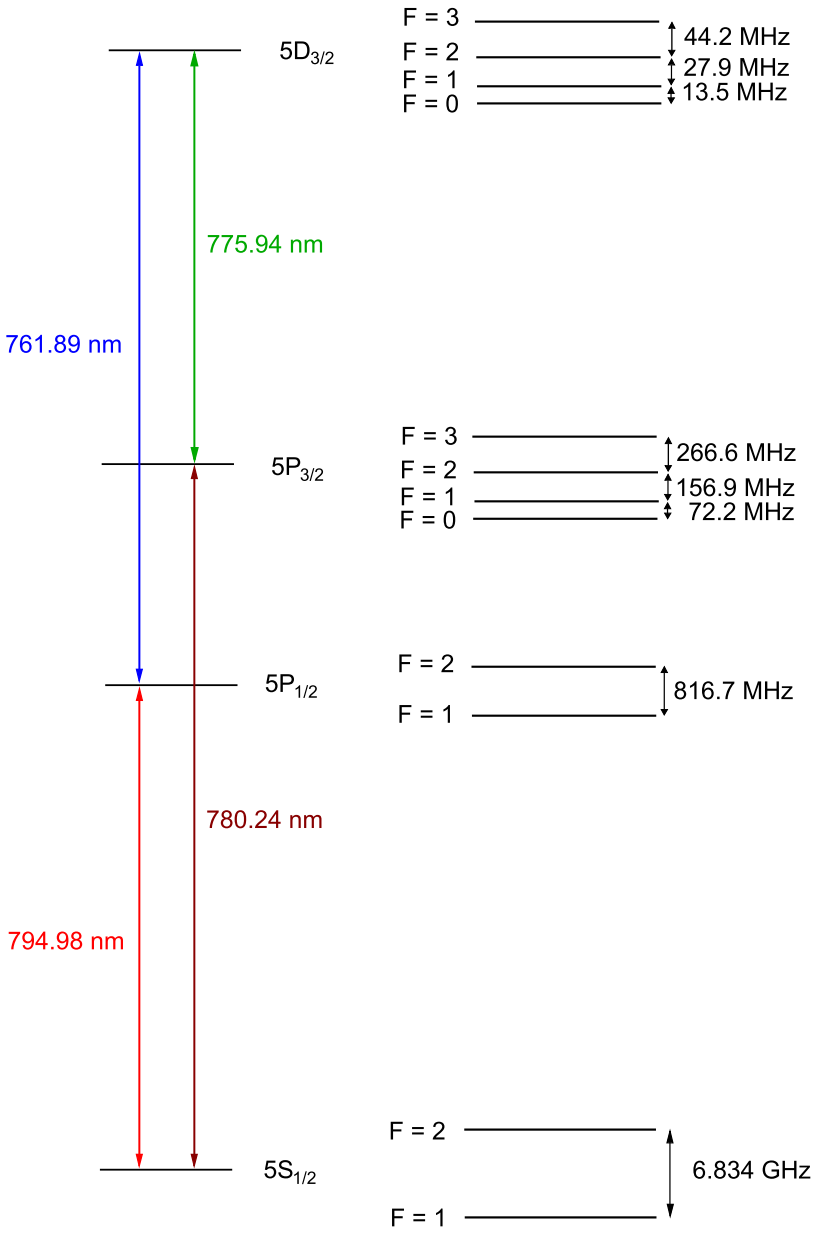

Figure E.4: Hyperfine structure of the relevant levels in ^{8}7Rb.

References

[1] P.W. Shor. **Algorithms for quantum computation: discrete logarithms and factoring**. In *Foundations of Computer Science, 1994 Proceedings., 35th Annual Symposium on*, pages 124 –134, nov 1994.

[2] Lov K. Grover. **A fast quantum mechanical algorithm for database search**. In *Proceedings of the twenty-eighth annual ACM symposium on Theory of computing*, STOC '96, pages 212–219, New York, NY, USA, 1996. ACM.

[3] Andrew Steane. **Quantum computing**. *Reports on Progress in Physics*, **61**(2):117, 1998.

[4] Artur K. Ekert. **Quantum cryptography based on Bell's theorem**. *Phys. Rev. Lett.*, **67**:661–663, Aug 1991.

[5] Charles H Bennett and Gilles Brassard. *Quantum cryptography: Public key distribution and coin tossing*, **175**, pages 175–179. Bangalore, India, 1984.

[6] H. J. Kimble. **The quantum internet**. *Nature*, **453**:1023–1030, 2008.

[7] L.-M. Duan, M. D. Lukin, J. I. Cirac, and P. Zoller. **Long-distance quantum communication with atomic ensembles and linear optics**. *Nature*, **414**:413–418, 2001.

[8] J. I. Cirac, P. Zoller, H. J. Kimble, and H. Mabuchi. **Quantum State Transfer and Entanglement Distribution among Distant Node in a Quantum Network**. *Phys. Rev. Lett.*, **78**:3221–3224, 1997.

[9] P. Zoller, Th. Beth, D. Binosi, R. Blatt, H. Briegel, D. Bruss, T. Calarco, J. I. Cirac, D. Deutsch, J. Eisert, A. Ekert, C. Fabre, N. Gisin, P. Grang-

iere, M. Grassl, S. Haroche, A. Imamoglu, A. Karlson, J. Kempe, L. Kouwenhoven, S. Kröll, G. Leuchs, M. Lewenstein, D. Loss, N. Lütkenhaus, S. Massar, J. E. Mooij, M. B. Plenio, E. Polzik, S. Popescu, G. Rempe, A. Sergienko, D. Suter, J. Twamley, G. Wendin, R. Werner, A. Winter, J. Wrachtrup, and A. Zeilinger. **Quantum information processing and communication**. *The European Physical Journal D - Atomic, Molecular, Optical and Plasma Physics*, **36**:203–228, 2005. 10.1140/epjd/e2005-00251-1.

[10] Emanuel Knill, Raymond Laflamme, and Gerald J Milburn. **A scheme for efficient quantum computation with linear optics**. *nature*, **409**(6816):46–52, 2001.

[11] Gavin K. Brennen, Carlton M. Caves, Poul S. Jessen, and Ivan H. Deutsch. **Quantum Logic Gates in Optical Lattices**. *Phys. Rev. Lett.*, **82**(5):1060–1063, Feb 1999.

[12] J. I. Cirac and P. Zoller. **Quantum Computations with Cold Trapped Ions**. *Phys. Rev. Lett.*, **74**(20):4091–4094, May 1995.

[13] Q. A. Turchette, C. J. Hood, W. Lange, H. Mabuchi, and H. J. Kimble. **Measurement of Conditional Phase Shifts for Quantum Logic**. *Phys. Rev. Lett.*, **75**:4710–4713, Dec 1995.

[14] J.A. Jones. **NMR quantum computation**. *Progress in Nuclear Magnetic Resonance Spectroscopy*, **38**(4):325–360, 2001. cited By (since 1996) 106.

[15] John Clarke and Frank K. Wilhelm. **Superconducting quantum bits**. *Nature*, **453**(7198):1031–1042, Jun 2008.

[16] Daniel Loss and David P. DiVincenzo. **Quantum computation with quantum dots**. *Phys. Rev. A*, **57**(1):120–126, Jan 1998.

[17] Kalle-Antti Suominen. **Physical Implementation of Large-Scale Quantum Computation**. In Grzegorz Rozenberg, Thomas Bck, and JoostN. Kok, editors, *Handbook of Natural Computing*, pages 1493–1520. Springer Berlin Heidelberg, 2012.

[18] G Leuchs and M Sondermann. **Time-reversal symmetry in optics***. *Physica Scripta*, **85**(5):058101, 2012.

[19] M. Stobińska, G. Alber, and G. Leuchs. **Perfect excitation of a matter qubit by a single photon in free space**. *Europhys. Lett.*, **86**:14007, 2009.

[20] Yimin Wang, J Minár, Lana Sheridan, and Valerio Scarani. **Efficient excitation of a two-level atom by a single photon in a propagating mode**. *Phys. Rev. A*, **83**:063842, Jun 2011.

[21] M Bader, S Heugel, A L Chekhov, M Sondermann, and G Leuchs. **Efficient coupling to an optical resonator by exploiting time-reversal symmetry**. *New Journal of Physics*, **15**(12):123008, 2013.

[22] J. Wenner, Yi Yin, Yu Chen, R. Barends, B. Chiaro, E. Jeffrey, J. Kelly, A. Megrant, J. Y. Mutus, C. Neill, P. J. J. O'Malley, P. Roushan, D. Sank, A. Vainsencher, T. C. White, Alexander N. Korotkov, A. N. Cleland, and John M. Martinis. **Catching Time-Reversed Microwave Coherent State Photons with 99.4% Absorption Efficiency**. *Phys. Rev. Lett.*, **112**:210501, May 2014.

[23] Chang Liu, Yuan Sun, Luwei Zhao, Shanchao Zhang, M. M. T. Loy, and Shengwang Du. **Efficiently Loading a Single Photon into a Single-Sided Fabry-Perot Cavity**. *Phys. Rev. Lett.*, **113**:133601, Sep 2014.

[24] Syed Abdullah Aljunid, Gleb Maslennikov, Yimin Wang, Dao Hoang Lan, Valerio Scarani, and Christian Kurtsiefer. **Excitation of a single atom with exponentially rising light pulses**. *Phys. Rev. Lett*, **111**:103001, 2013.

[25] Stephan Ritter, Christian Noelleke, Carolin Hahn, Andreas Reiserer, Andreas Neuzner, Manuel Uphoff, Martin Muecke, Eden Figueroa, Joerg Bochmann, and Gerhard Rempe. **An elementary quantum network of single atoms in optical cavities**. *Nature*, **484**:195–200, 2012.

[26] Martin Fischer, Marianne Bader, Robert Maiwald, Andrea Golla, Markus Sondermann, and Gerd Leuchs. **Efficient saturation of an ion in free space**. *Applied Physics B*, **117**(3):797–801, 2014.

[27] Bharath Srivathsan, Gurpreet Gulati, Brenda Chng, Gleb Maslennikov, Dzmitry Matsukevich, and Christian Kurtsiefer. **Narrow Band Source of Transform-Limited Photon Pairs via Four-Wave Mixing in a Cold Atomic Ensemble**. *Phys. Rev. Lett.*, **111**:123602, Sep 2013.

[28] Gurpreet Kaur Gulati, Bharath Srivathsan, Brenda Chng, Alessandro Cerè, Dzmitry Matsukevich, and Christian Kurtsiefer. **Generation of an exponentially rising single-photon field from parametric conversion in atoms**. *Phys. Rev. A*, **90**:033819, Sep 2014.

[29] Bharath Srivathsan, Gurpreet Kaur Gulati, Alessandro Cerè, Brenda Chng, and Christian Kurtsiefer. **Reversing the Temporal Envelope of a Heralded Single Photon using a Cavity**. *Phys. Rev. Lett.*, **113**:163601, Oct 2014.

[30] Alain Aspect, Philippe Grangier, and Gérard Roger. **Experimental Tests of Realistic Local Theories via Bell's Theorem**. *Phys. Rev. Lett.*, **47**:460–463, Aug 1981.

[31] John F. Clauser, Michael A. Horne, Abner Shimony, and Richard A. Holt. **Proposed Experiment to Test Local Hidden-Variable Theories**. *Phys. Rev. Lett.*, **23**:880–884, Oct 1969.

[32] Edward S. Fry and Randall C. Thompson. **Experimental Test of Local Hidden-Variable Theories**. *Phys. Rev. Lett.*, **37**:465–468, Aug 1976.

[33] Gregor Weihs, Thomas Jennewein, Christoph Simon, Harald Weinfurter, and Anton Zeilinger. **Violation of Bell's Inequality under Strict Einstein Locality Conditions**. *Phys. Rev. Lett.*, **81**:5039–5043, Dec 1998.

[34] Michael A. Nielsen and Isaac L. Chuang. *Quantum Computation and Quantum Information*. Cambridge University Press, 1 edition, January 2004.

[35] D. Bouwmeester, A.K. Ekert, and A. Zeilinger. *The Physics of Quantum Information: Quantum Cryptography, Quantum Teleportation, Quantum Computation*. Springer, 2010.

[36] Thomas Jennewein, Christoph Simon, Gregor Weihs, Harald Weinfurter, and Anton Zeilinger. **Quantum Cryptography with Entangled Photons**. *Phys. Rev. Lett.*, **84**:4729–4732, May 2000.

[37] Alain Aspect, Philippe Grangier, and Gérard Roger. **Experimental Realization of Einstein-Podolsky-Rosen-Bohm *Gedankenexperiment*: A New Violation of Bell's Inequalities**. *Phys. Rev. Lett.*, **49**:91–94, Jul 1982.

[38] David C. Burnham and Donald L. Weinberg. **Observation of Simultaneity in Parametric Production of Optical Photon Pairs**. *Phys. Rev. Lett.*, **25**:84–87, Jul 1970.

[39] Paul G. Kwiat, Klaus Mattle, Harald Weinfurter, Anton Zeilinger, Alexander V. Sergienko, and Yanhua Shih. **New High-Intensity Source of Polarization-Entangled Photon Pairs**. *Phys. Rev. Lett.*, **75**:4337–4341, Dec 1995.

[40] Christian Kurtsiefer, Markus Oberparleiter, and Harald Weinfurter. **High-efficiency entangled photon pair collection in type-II parametric fluorescence**. *Phys. Rev. A*, **64**:023802, Jul 2001.

[41] Taehyun Kim, Marco Fiorentino, and Franco N. C. Wong. **Phase-stable source of polarization-entangled photons using a polarization Sagnac interferometer**. *Phys. Rev. A*, **73**:012316, Jan 2006.

[42] F. Wolfgramm, X. Xing, A. Cerè, A. Predojević, A. M. Steinberg, and M. W. Mitchell. **Bright filter-free source of indistinguishable photon pairs**. *Opt. Express*, **16**(22):18145–18151, Oct 2008.

[43] A. Haase, N. Piro, J. Eschner, and M. W. Mitchell. **Tunable narrowband entangled photon pair source for resonant single-photon single-atom interaction**. *Opt. Lett.*, **34**:55–57, 2009.

[44] Alessandro Cerè, Valentina Parigi, Marta Abad, Florian Wolfgramm, Ana Predojević, and Morgan W. Mitchell. **Narrowband tunable filter based on velocity-selective optical pumping in an atomic vapor**. *Opt. Lett.*, **34**(7):1012–1014, Apr 2009.

[45] Michael Förtsch, Josef Fürst, Christoffer Wittmann, Dmitry Strekalov, Andrea Aiello, Maria V. Chekhova, Christine Silberhorn, Gerd Leuchs, and Christoph Marquardt. **A Versatile Source of Single Photons for Quantum Information Processing**. *arXiv:1204.3056v2*, 2012.

[46] A. R. McMillan, J. Fulconis, M. Halder, C. Xiong, J. G. Rarity, and W. J. Wadsworth. **Narrowband high-fidelity all-fibre source of heralded single photons at 1570 nm**. *Opt. Express*, **17**(8):6156–6165, Apr 2009.

[47] M. Halder, J. Fulconis, B. Cemlyn, A. Clark, C. Xiong, W. J. Wadsworth, and J. G. Rarity. **Nonclassical 2-photon interference with separate intrinsically narrowband fibre sources**. *Opt. Express*, **17**(6):4670–4676, Mar 2009.

[48] R. T. Willis, F. E. Becerra, L. A. Orozco, and S. L. Rolston. **Correlated photon pairs generated from a warm atomic ensemble**. *Phys. Rev. A*, **82**:053842, Nov 2010.

[49] Qun feng Chen, Bao-Sen Shi, Min Feng, Yong-Sheng Zhang, and Guang-Can Guo. **Non-degenerated nonclassical photon pairs in a hot atomic ensemble**. *Opt. Express*, **16**(26):21708–21713, Dec 2008.

[50] James K. Thompson, Jonathan Simon, Huanqian Loh, and Vladan Vuleti. **A High-Brightness Source of Narrowband, Identical-Photon Pairs**. *Science*, **313**(5783):74–77, 2006.

[51] Pavel Kolchin, Shengwang Du, Chinmay Belthangady, G. Y. Yin, and S. E. Harris. **Generation of Narrow-Bandwidth Paired Photons: Use of a Single Driving Laser**. *Phys. Rev. Lett.*, **97**:113602, Sep 2006.

[52] A. Kuzmich, W. P. Bowen, A. D. Boozer, A. Boca, C. W. Chou, L.-M. Duan, and H. J. Kimble. **Generation of nonclassical photon pairs for scalable quantum communication with atomic ensembles**. *Nature*, **423**:731–734, 2003.

[53] T. Chanelière, D. N. Matsukevich, S. D. Jenkins, T. A. B. Kennedy, M. S. Chapman, and A. Kuzmich. **Quantum Telecommunication Based on Atomic Cascade Transitions**. *Phys. Rev. Lett.*, **96**:093604, Mar 2006.

[54] Robert W. Boyd. *Nonlinear Optics, Third Edition*. Academic Press, 3rd edition, 2008.

[55] D F. Walls and Gerard J. Milburn. *Quantum optics*. Springer, Jan 2008.

[56] Hsiang-Hua Jen. *Theory of light-matter interactions in cascade and diamond type atomic ensembles*. PhD thesis, Georgia Institute of Technology, 2011.

[57] Christopher J. Foot. *Atomic Physics*. Oxford University Press, 1st edition, 2005.

[58] Meng Khoon Tey, Zilong Chen, Syed Abdullah Aljunid, Brenda Chng, Florian Huber, Gleb Maslennikov, and Christian Kurtsiefer. **Strong interaction**

between light and a single trapped atom without the need for a cavity. *Nature Physics*, **4**:924–927, 2008.

[59] Meng Khoon Tey. *Interfacing light and a single quantum system with a lens*. PhD thesis, National University of Singapore, 2009.

[60] D.A. Steck. **Rubidium 87 D line data**, 2001.

[61] *DL7140-201S Infrared laser diode*.

[62] A. S. Arnold, J. S. Wilson, and M. G. Boshier. **A simple extended-cavity diode laser**. *Review of Scientific Instruments*, **69**(3), 1998.

[63] R. Paschotta. **Beat Note**. *Encyclopedia of Laser Physics and Technology*.

[64] **NIST Atomic Spectra Database**.

[65] James M. Supplee, Edward A. Whittaker, and Wilfried Lenth. **Theoretical description of frequency modulation and wavelengthmodulation spectroscopy**. *Appl. Opt.*, **33**(27):6294–6302, Sep 1994.

[66] E. L. Raab, M. Prentiss, Alex Cable, Steven Chu, and D. E. Pritchard. **Trapping of Neutral Sodium Atoms with Radiation Pressure**. *Phys. Rev. Lett.*, **59**:2631–2634, Dec 1987.

[67] A. M. Steane and C. J. Foot. **Laser Cooling below the Doppler Limit in a Magneto-Optical Trap**. *EPL (Europhysics Letters)*, **14**(3):231, 1991.

[68] Umakant D. Rapol, Ajay Wasan, and Vasant Natarajan. **Loading of a** Rb **magneto-optic trap from a getter source**. *Phys. Rev. A*, **64**:023402, Jun 2001.

[69] *MicroVac Controller*.

[70] Stephen E. Harris. **Electromagnetically Induced Transparency**. *Physics Today*, **50**(7):36–42, 1997.

[71] Siddarth Joshi. *Entangled Photon Pairs: Efficient Generation And Detection, And Bit Commitment*. PhD thesis, National University of Singapore, 2014.

[72] R. T. Willis, F. E. Becerra, L. A. Orozco, and S. L. Rolston. **Four-wave mixing in the diamond configuration in an atomic vapor**. *Phys. Rev. A*, **79**:033814, Mar 2009.

[73] R. H. Dicke. **Coherence in Spontaneous Radiation Processes**. *Phys. Rev.*, **93**:99–110, Jan 1954.

[74] Nicholas E. Rehler and Joseph H. Eberly. **Superradiance**. *Phys. Rev. A*, **3**:1735–1751, May 1971.

[75] Claude Cohen-Tannoudji, Jacques Dupont-Roc, and Gilbert Grynberg. *Atom-Photon Interactions: Basic Processes and Applications*. Wiley-VCH, 1997.

[76] Gurpreet Kaur Gulati. *Narrowband source of entangled photon pairs via fourwave mixing in cold atomic ensemble (in preparation)*. PhD thesis, National University of Singapore, 2014.

[77] Stewart David Jenkins. *Theory of Light - Atomic Ensemble Interactions: Entanglement, Storage, and Retrieval*. PhD thesis, Georgia Institute of Technology, 2006.

[78] Daniel F. V. James, Paul G. Kwiat, William J. Munro, and Andrew G. White. **Measurement of qubits**. *Phys. Rev. A*, **64**:052312, Oct 2001.

[79] Scott Hill and William K. Wootters. **Entanglement of a Pair of Quantum Bits**. *Phys. Rev. Lett.*, **78**:5022–5025, Jun 1997.

[80] H. J. Kimble, M. Dagenais, and L. Mandel. **Photon Antibunching in Resonance Fluorescence**. *Phys. Rev. Lett.*, **39**:691–695, Sep 1977.

[81] B. Darquié, M. P. A. Jones, J. Dingjan, J. Beugnon, S. Bergamini, Y. Sortais, G. Messin, A. Browaeys, and P. Grangier. **Controlled Single-Photon Emission from a Single Trapped Two-Level Atom**. *Science*, **309**(5733):454–456, 2005.

[82] Frank Diedrich and Herbert Walther. **Nonclassical radiation of a single stored ion**. *Phys. Rev. Lett.*, **58**:203–206, Jan 1987.

[83] B. Lounis and W. E. Moerner. **Single photons on demand from a single molecule at room temperature**. *Nature*, **407**:491–493, 2000.

[84] Th. Basché, W. E. Moerner, M. Orrit, and H. Talon. **Photon antibunching in the fluorescence of a single dye molecule trapped in a solid**. *Phys. Rev. Lett.*, **69**:1516–1519, Sep 1992.

[85] P. Michler, A. Kiraz, C. Becher, W. V. Schoenfeld, P. M. Petroff, Lidong Zhang, E. Hu, and A. Imamoglu. **A Quantum Dot Single-Photon Turnstile Device**. *Science*, **290**(5500):2282–2285, 2000.

[86] Charles Santori, Matthew Pelton, Glenn Solomon, Yseulte Dale, and Yoshihisa Yamamoto. **Triggered Single Photons from a Quantum Dot**. *Phys. Rev. Lett.*, **86**:1502–1505, Feb 2001.

[87] Zhiliang Yuan, Beata E. Kardynal, R. Mark Stevenson, Andrew J. Shields, Charlene J. Lobo, Ken Cooper, Neil S. Beattie, David A. Ritchie, and Michael Pepper. **Electrically Driven Single-Photon Source**. *Science*, **295**(5552):102–105, 2002.

[88] Christian Kurtsiefer, Sonja Mayer, Patrick Zarda, and Harald Weinfurter. **Stable Solid-State Source of Single Photons**. *Phys. Rev. Lett.*, **85**:290–293, Jul 2000.

[89] Rosa Brouri, Alexios Beveratos, Jean-Philippe Poizat, and Philippe Grangier. **Photon antibunching in the fluorescence of individual color centers in diamond**. *Opt. Lett.*, **25**(17):1294–1296, Sep 2000.

[90] Axel Kuhn, Markus Hennrich, and Gerhard Rempe. **Deterministic Single-Photon Source for Distributed Quantum Networking**. *Phys. Rev. Lett.*, **89**:067901, Jul 2002.

[91] J. McKeever, A. Boca, A. D. Boozer, R. Miller, J. R. Buck, A. Kuzmich, and H. J. Kimble. **Deterministic Generation of Single Photons from One Atom Trapped in a Cavity**. *Science*, **303**(5666):1992–1994, 2004.

[92] E. Moreau, I. Robert, J. M. Grard, I. Abram, L. Manin, and V. Thierry-Mieg. **Single-mode solid-state single photon source based on isolated quantum dots in pillar microcavities**. *Applied Physics Letters*, **79**(18):2865–2867, 2001.

[93] Peter J. Mosley, Jeff S. Lundeen, Brian J. Smith, Piotr Wasylczyk, Alfred B. U'Ren, Christine Silberhorn, and Ian A. Walmsley. **Heralded Generation of Ultrafast Single Photons in Pure Quantum States**. *Phys. Rev. Lett.*, **100**:133601, Apr 2008.

[94] D. N. Matsukevich, T. Chanelière, S. D. Jenkins, S.-Y. Lan, T. A. B. Kennedy, and A. Kuzmich. **Deterministic Single Photons via Conditional Quantum Evolution**. *Phys. Rev. Lett.*, **97**:013601, Jul 2006.

[95] Jérémie Fulconis, Olivier Alibart, Jeremy L. O'Brien, William J. Wadsworth, and John G. Rarity. **Nonclassical Interference and Entanglement Generation Using a Photonic Crystal Fiber Pair Photon Source**. *Phys. Rev. Lett.*, **99**:120501, Sep 2007.

[96] Marcelo Davanco, Jun Rong Ong, Andrea Bahgat Shehata, Alberto Tosi, Imad Agha, Solomon Assefa, Fengnian Xia, William M. J. Green, Shayan Mookherjea, and Kartik Srinivasan. **Telecommunications-band heralded single photons from a silicon nanophotonic chip**. *Applied Physics Letters*, **100**(26):–, 2012.

[97] Roy J. Glauber. **The Quantum Theory of Optical Coherence**. *Phys. Rev.*, **130**:2529–2539, Jun 1963.

[98] Rodney Loudon. *The quantum theory of light*. Oxford university press, 2000.

[99] P. Grangier, G. Roger, and A. Aspect. **Experimental Evidence for a Photon Anticorrelation Effect on a Beam Splitter: A New Light on Single-Photon Interferences**. *EPL (Europhysics Letters)*, **1**(4):173, 1986.

[100] G. Rempe, R. J. Thompson, H. J. Kimble, and R. Lalezari. **Measurement of ultralow losses in an optical interferometer**. *Opt. Lett.*, **17**:363–365, 1992.

[101] A. Walther, A. Amari, S. Kröll, and A. Kalachev. **Experimental superradiance and slow-light effects for quantum memories**. *Phys. Rev. A*, **80**:012317, Jul 2009.

[102] H. H. Jen. **Positive-P phase-space-method simulation of superradiant emission from a cascade atomic ensemble**. *Phys. Rev. A*, **85**:013835, Jan 2012.

[103] Horace P Yuen and Vincent W S Chan. **Noise in homodyne and heterodyne detection**. *Optics Letters*, **8**:177–179, 1983.

[104] A. I. Lvovsky, H. Hansen, T. Aichele, O. Benson, J. Mlynek, and S. Schiller. **Quantum State Reconstruction of the Single-Photon Fock State**. *Phys. Rev. Lett.*, **87**:050402, Jul 2001.

[105] D. T. Smithey, M. Beck, M. G. Raymer, and A. Faridani. **Measurement of the Wigner distribution and the density matrix of a light mode using optical homodyne tomography: Application to squeezed states and the vacuum**. *Phys. Rev. Lett.*, **70**:1244–1247, Mar 1993.

[106] Alexei Ourjoumtsev, Rosa Tualle-Brouri, and Philippe Grangier. **Quantum Homodyne Tomography of a Two-Photon Fock State**. *Phys. Rev. Lett.*, **96**:213601, Jun 2006.

[107] V Weisskopf and E Wigner. **Berechnung der natürlichen Linienbreite auf Grund der Diracschen Lichttheorie**. *Z. Physik*, **63**:54, 1930.

[108] Andreas Reiserer, Norbert Kalb, Gerhard Rempe, and Stephan Ritter. **A quantum gate between a flying optical photon and a single trapped atom**. *Nature*, **508**:237, 2014.

[109] Alexander I Lvovsky, Barry Sanders, and Wolfgang Tittel. **Optical quantum memory**. *Nat. Photonics*, **3**:706–714, 2009.

[110] Shanchao Zhang, Chang Liu, Shuyu Zhou, Chih-Sung Chuu, M. M. T. Loy, and Shengwang Du. **Coherent Control of Single-Photon Absorption and Reemission in a Two-Level Atomic Ensemble**. *Phys. Rev. Lett.*, **109**:263601, Dec 2012.

[111] Thomas Volz, Andreas Reinhard, Martin Winger, Antonio Badolato, Kevin J. Hennessy, Evelyn L. Hu, and Atac Imamoglu. **Ultrafast all-optical switching by single photons**. *Nat Photon*, **6**:605, 2012.

[112] R. Johne and A. Fiore. **Single-photon absorption and dynamic control of the exciton energy in a coupled quantum-dot-cavity system**. *Phys. Rev. A*, **84**:053850, Nov 2011.

[113] Y. L. A. Rezus, S. G. Walt, R. Lettow, A. Renn, G. Zumofen, S. Götzinger, and V. Sandoghdar. **Single-Photon Spectroscopy of a Single Molecule**. *Phys. Rev. Lett.*, **108**:093601, Feb 2012.

[114] Pavel Kolchin, Chinmay Belthangady, Shengwang Du, G. Y. Yin, and S. E. Harris. **Electro-Optic Modulation of Single Photons**. *Phys. Rev. Lett.*, **101**:103601, Sep 2008.

[115] J. D. Franson. **Nonlocal cancellation of dispersion**. *Phys. Rev. A*, **45**:3126–3132, Mar 1992.

[116] Charles Santori, David Fattal, Matthew Pelton, Glenn S. Solomon, and Yoshihisa Yamamoto. **Polarization-correlated photon pairs from a single quantum dot**. *Phys. Rev. B*, **66**:045308, Jul 2002.

[117] Adrien Dousse, Jan Suffczynski, Alexios Beveratos, Olivier Krebs, Aristide Lemaitre, Isabelle Sagnes, Jacqueline Bloch, Paul Voisin, and Pascale Senellart. **Ultrabright source of entangled photon pairs**. *Nature*, **466**:217, 2010.

[118] N. Akopian, N. H. Lindner, E. Poem, Y. Berlatzky, J. Avron, D. Gershoni, B. D. Gerardot, and P. M. Petroff. **Entangled Photon Pairs from Semiconductor Quantum Dots**. *Phys. Rev. Lett.*, **96**:130501, Apr 2006.

[119] N. Hodgson and H. Weber. *Optical Resonators: Fundamentals, Advanced Concepts, and Applications*. Springer Verlag, 1997.

[120] Girish S. Agarwal and S. Dutta Gupta. **Filtering of two-photon quantum correlations by optical cavities: Cancellation of dispersive effects**. *Phys. Rev. A*, **49**:3954–3957, May 1994.

[121] S. Heugel, A.S. Villar, M. Sondermann, U. Peschel, and G. Leuchs. **On the analogy between a single atom and an optical resonator**. *Laser Physics*, **20**(1):100–106, 2010.

[122] M. Sondermann, R. Maiwald, H. Konermann, N. Lindlein, U. Peschel, and G. Leuchs. **Design of a mode converter for efficient light-atom coupling in free space**. *Applied Physics B*, **89**(4):489–492, 2007.

[123] Christoph Kurz, Michael Schug, Pascal Eich, Jan Huwer, Philipp Müller, and Jürgen Eschner. **Experimental protocol for high-fidelity heralded photon-to-atom quantum state transfer**. *arxiv:1312.5995*, 2014.

[124] M. Schug, J. Huwer, C. Kurz, P. Müller, and J. Eschner. **Heralded Photonic Interaction between Distant Single Ions**. *Phys. Rev. Lett.*, **110**:213603, May 2013.

[125] Sandoko Kosen. *Quantum Interference between Single Photons from a Single Atom and a Cold Atomic Ensemble*. Master's thesis, National University of Singapore, 2014.

[126] C. G. Townsend, N. H. Edwards, C. J. Cooper, K. P. Zetie, C. J. Foot, A. M. Steane, P. Szriftgiser, H. Perrin, and J. Dalibard. **Phase-space density in the magneto-optical trap**. *Phys. Rev. A*, **52**:1423–1440, Aug 1995.

[127] Thad Walker, David Sesko, and Carl Wieman. **Collective behavior of optically trapped neutral atoms**. *Phys. Rev. Lett.*, **64**:408–411, Jan 1990.

[128] Adam T. Black, James K. Thompson, and Vladan Vuletić. **On-Demand Superradiant Conversion of Atomic Spin Gratings into Single Photons with High Efficiency**. *Phys. Rev. Lett.*, **95**:133601, Sep 2005.

[129] M. Gross and S. Haroche. **Superradiance: An essay on the theory of collective spontaneous emission**. *Physics Reports*, **93**(5):301 – 396, 1982.

[130] Justin G. Bohnet, Zilong Chen, Joshua M. Weiner, Dominic Meiser, Murray J. Holland, and James K. Thompson. **A steady-state superradiant laser with less than one intracavity photon**. *Nature*, **484**(0028-0836):78–81, 2012.

[131] T. Wang, S. F. Yelin, R. Côté, E. E. Eyler, S. M. Farooqi, P. L. Gould, M. Koštrun, D. Tong, and D. Vrinceanu. **Superradiance in ultracold Rydberg gases**. *Phys. Rev. A*, **75**:033802, Mar 2007.

[132] Markus P. Baden, Kyle J. Arnold, Arne L. Grimsmo, Scott Parkins, and Murray D. Barrett. **Realization of the Dicke Model Using Cavity-Assisted Raman Transitions**. *Phys. Rev. Lett.*, **113**:020408, Jul 2014.

[133] T. Chaneliere, D. N. Matsukevich, S. D. Jenkins, S.-Y. Lan, T. A. B. Kennedy, and A. Kuzmich. **Storage and retrieval of single photons transmitted between remote quantum memories**. *Nature*, **438**(7069):833–836, 2005.